

# Ultra-Low Electron Temperatures in Nanostructured Samples

## Inauguraldissertation

zur

Erlangung der Würde eines Doktors der Philosophie

vorgelegt der

Philosophisch-Naturwissenschaftlichen Fakultät

der Universität Basel

von

**Lucas Casparis**

aus Bergün, Scharans, Fürstenau und Thusis GR



Basel, 2015

Genehmigt von der Philosophisch-Naturwissenschaftlichen Fakultät auf Antrag von

Prof. Dr. D. M. Zumbühl

Prof. Dr. J. P. Pekola

Prof. Dr. J. A. Folk

Basel, 14. Oktober 2014

Prof. Dr. Jürg Schibler

Dekan

*"Der Fortschritt ist absolut humorlos, weil er den Optimisten ausgeliefert ist."*

Heinrich Böll

# Abstract

Nanostructured samples, be it semiconducting or metallic ones, have received considerable experimental and theoretical attention due to the manifold of possibilities to investigate fundamental physics. Not only are they viable candidates for realizations of qubits, the key ingredient of quantum computation, but the surrounding solid makes it a testing ground for many-body physics. Novel quantum mechanical effects, such as topological phases and electron-mediated ferromagnetic nuclear spin ordering, are predicted to emerge in such systems. Low temperatures are crucial for these many-body effects as the energies scales involved are typically very small. State of the art electron transport experiments reach an electron temperature of roughly 10 mK. In order to reach sub-millikelvin electron temperatures, we develop a novel type of refrigerator aimed at cooling nanostructured samples, where nuclear demagnetization refrigerators are integrated into every measurement lead, directly cooling the electrons therein. Hence circumventing the limitation of electron-phonon coupling which is drastically suppressed at the lowest temperatures due to its  $T^5$  dependence.

We implement various kinds of electron thermometers to measure the electron temperature in typical samples. In metallic Coulomb blockade thermometers (CBTs), we observe a deviation from the electron-phonon cooling mechanism, indicating that we succeed in cooling samples through the conduction electrons. Further, we investigate a quantum dot in a typical GaAs device. The quantum dot thermometer is operated in deep Coulomb blockade and probes the Fermi edge of the surrounding electron reservoir both through direct transport and a proximal charge sensing device. After considerable tuning effort an electron temperature of 10 mK is extracted. Our experiments show that the temperature reading is very susceptible to the electrostatic environment, emphasizing the importance of the surrounding solid and demonstrating the difficulty to implement a temperature sensor at the lowest temperatures. More importantly the low electron temperatures open the possibility for very sensitive measurements of

back-action effects of the charge sensor or the charge stability of the material.

After optimizing the chip socket and improving the filtering in the system, an electron temperature of  $5.2 \text{ mK} \pm 0.3 \text{ mK}$  in a CBT is measured after demagnetization. By measuring the temperature dependent I-V curves of a normal metal/insulator/superconductor (NIS) tunnel junction, we implement yet another thermometer, which we employ as both primary and secondary thermometer. On top of that, we demonstrate with the help of reentrant features in the fractional quantum Hall regime, cooling of electrons in a high mobility GaAs two-dimensional electron gas (2DEG) below the base temperature of our dilution refrigerator.

Using our low electron temperatures, we investigate high mobility GaAs 2DEG devices in large magnetic fields. In our samples the typical signature of the quantum Hall effect is dramatically altered, resulting in a quantized longitudinal resistance. We can show that this quantization, which occurs only at the lowest temperatures, is due to a large electron density gradient in the 2DEG. As we show subsequently for the  $\nu = 5/2$  fractional quantum Hall state, the electron density gradient heavily influences the extraction of the energy gap between the ground and excited state. Being a candidate for one of the above mentioned topologically non-trivial ground states, our findings could have important consequences for the fabrication of  $\nu = 5/2$  fractional quantum Hall state samples.

Additionally, we measure the electrical resistance anisotropy in both natural graphite and highly ordered pyrolytic graphite (HOPG), comparing macroscopic samples, with exfoliated, nanofabricated specimens of nanometer thickness. In nanoscale samples, independent on the graphite type, we find a very large c-axis resistivity  $\rho_c$  – much larger than expected from simple band theory – and non-monotonic temperature dependence. This is similar to macroscopic HOPG, but in stark contrast to macroscopic natural graphite. A recent model of disorder-induced delocalization is consistent with our transport data. Furthermore, Micro-Raman spectroscopy reveals clearly reduced disorder in exfoliated samples and HOPG, as expected within the model.

## Acknowledgments

Many people have contributed to this work and without them this work would not have been possible. Above all, I wish to express my gratitude to Dominik Zumbühl for being my PhD supervisor. His thorough scientific guidance throughout my PhD allowed us to tackle many challenges. But it was his exceptional educational skills, which made this last four years a truly instructive experience, touching on fundamental concepts and ideas and teaching me how to approach them. Together with his will to understand every experimental detail, this made him a great resource for discussion about everything from lab specifics to physics fundamentals.

A large fraction of the work presented in this thesis is based on a fruitful collaboration with the *Pico* group of Jukka Pekola. I want to especially thank Matthias Meschke and Anna Feshchenko for the fabrication of the CBT and NIS devices as well as for the valuable inputs they gave during discussing low  $T$  electron thermometry. Jukka himself always had an open ear for our experimental problems and provided us at any time with the theoretical background. I want to thank all of them for their patience during our time consuming experiments and publication processes.

The graphite project was initiated by Dimitrii Maslov, for which I want to thank him. It is a fascinating and humbling experience to participate and discuss with such a distinguished and quickly-minded physicist. In the further course of the graphite work, we also did some numerical simulations with the help of Andreas Fuhrer at IBM Rüsçhlikon, who provided us with the Matlab code, many thanks for that and the stimulating inputs from his side considering the experiment.

In terms of the more daily working environment, I would like to thank Tony Clark. He was the one introducing me to ultra-low temperatures and the experimental setup. Although not famous for his patience, he somehow could exercise a lot of patience with me, the new, inexperienced PhD student. In the 6 months we worked together, he taught me many things, most importantly how to deal with experimental setbacks –

black humor.

Of course this thesis could not have been written without Dario Maradan. On one hand he built the MNK-P fridge, the protagonist of this thesis, during his master thesis. On the other hand we shared many, many hours together not only in the lab but in meeting rooms and over lunch. After all these years I still feel that we are a good team and this is to a larger part because of him. His patience with my clumsiness, his calm, mindful working attitude, contrasting mine so heavily and his expertise in all experimental matters, made it easy for me enjoy working, and even more importantly becoming good friends with him.

Further within the  $\mu\text{K}$  project I had the pleasure to work with Tai-Min Liu, which kindly shared his valuable scientific, as well as his cultural experience with us. Spending time with him and his family both in the lab and outside the department was always great fun. Mario Palma joined the project in recent years and became a team member really fast, I wish him the best of luck for his PhD.

I'm very thankful that I could spend the last years in a very stimulating but still relaxed working environment, where conversations always were interesting and entertaining, although not always evolved around physics. For this good spirit in the group I want to thank my former office mates Dominikus Koelbl, Florian Dettwiler, Dorothee Hug, who also introduced me to general lab conduct and had helped me already excessively during my master thesis. It is nice that with the younger inhabitants of office 1.12, Pirmin Weigele, Yemliha Bilal Kalyoncu and Larissa Conrad the spirit persists.

I apologize for blowing up so many of Daniel Biesinger's quantum dots, it was always fun working in the lab with him and Christian Scheller (at least for me). Their quantum dot expertise was of great help in the course of our own experiments. Additionally Christian contributed valuably to cool our electrons with his insight on filtering and thermalization in general. I am further thankful to Myrsini Lafkioti for introducing me to the  $\nu=5/2$  project, which hopefully continues prospering in the near and far future. I would like to thank all former members of the Zumbühl group, Kai Schwarzälde,

Sarah Heizmann, Charulata Barge for setting up the lab, fridges and measurement setups and in particular Samuel Hess for building the Ag chip socket. Further, I hope the new group members Leon Camenzind and Taras Patlatiuk will enjoy working here as much as I did.

Additionally, I want to thank all members of Christian Schönenbergers group for the good collaboration both in the labs and the cleanroom.

All our experiments, especially the  $\mu K$  project, would not be operating without some outside expertise I would like to acknowledge. Big thanks go to the mechanical workshop, in particular Patrick Stöcklin and Sasha Martin for their fast help with all kinds of mechanical problems and their steady hand. Michael Steinacher and his electronic workshop helped in so many ways to optimize our setup and also understand where our limits are – thank you. Dominik Sifrig made sure we always had enough liquid-He, sometimes even by redistributing to our favour from other groups. For this and all his pump servicing I'm thankful. Further Barbara Kammermann and Astrid Kalt handled the administrative part impeccably and efficiently, their patient assistance was of great value at all time.

I am grateful that many of the people I got to know during my nine years in Basel, I now consider as true friends, especially This, Tinu and Luuki. To my great fortune I also found more than just friendship in Basel, thank you Melanie for being the firm, patient and encouraging anchor you are.

Of course finishing this PhD would not have been possible without the support of my old friends and family, especially my parents. Apart from your financial and moral backing, I thank you for leaving me the long time to realize that interest in physics is indeed a hereditary terminal illness.



# Contents

<b>Contents</b>	<b>VII</b>
<b>1 Introduction</b>	<b>1</b>
<b>2 Nuclear Refrigeration for Nanoelectronics</b>	<b>5</b>
2.1 Thermal Conductance of Solid Matter . . . . .	6
2.1.1 General Concepts . . . . .	6
2.1.2 Heat Conductivity . . . . .	6
2.2 Cooling of Solid Matter . . . . .	9
2.2.1 Thermal Boundary Resistance . . . . .	9
2.2.2 Electron-Phonon Coupling . . . . .	10
2.3 Adiabatic Nuclear Demagnetization . . . . .	11
2.3.1 Coupling of the Nuclear Spins to the Environment . . . . .	13
2.3.2 Influence of an External Heat Load . . . . .	15
2.3.3 Practical Considerations . . . . .	16
2.4 Design of the Refrigerator . . . . .	19
2.5 Refrigerator Performance . . . . .	21
2.5.1 Heat Leak . . . . .	22
2.5.2 Demagnetization Efficiency . . . . .	26
<b>3 Metallic Coulomb Blockade Thermometry down to 10 mK and below</b>	<b>31</b>
3.1 Motivation . . . . .	32
3.2 Strategy to Approach Submilikelvin Sample Temperatures . . . . .	32

3.2.1	Nuclear Refrigerator and Microwave Filtering Scheme . . . . .	33
3.2.2	Performance of the Nuclear Refrigerators . . . . .	34
3.3	Electron Temperature Measurements . . . . .	35
3.3.1	CBT Sample Overview . . . . .	35
3.3.2	CBT Performance for Different Sensors . . . . .	36
3.4	CBT Cooling Mechanism . . . . .	36
3.4.1	Theoretical Model including EP and WF Cooling . . . . .	36
3.4.2	Measured Cooling Power-Laws versus Theory . . . . .	37
3.5	Summary . . . . .	39
<b>4</b>	<b>GaAs Quantum Dot Thermometry Using Direct Transport and Charge Sensing</b>	<b>40</b>
4.1	Introduction . . . . .	41
4.2	Quantum Dot Thermometry . . . . .	43
4.3	Thermometry with Direct Transport . . . . .	47
4.4	Thermometry with Charge Sensing . . . . .	51
4.5	Discussion . . . . .	57
<b>5</b>	<b>Electron Thermometry using Metallic Nanostructures and the Quantum Hall Regime in an Improved Experimental Setup</b>	<b>60</b>
5.1	Introduction . . . . .	61
5.2	Coulomb Blockade Thermometry . . . . .	62
5.2.1	Two-Dimensional CBT Arrays . . . . .	62
5.2.2	Linear CBT Array . . . . .	64
5.3	Normal Metal/Insulator/Superconductor Thermometer . . . . .	66

5.3.1	Introduction . . . . .	66
5.3.2	Sample . . . . .	68
5.3.3	I-V Characteristics . . . . .	69
5.3.4	B-Field Dependence . . . . .	72
5.3.5	NIS Thermometry . . . . .	73
5.4	Reentrant State Quantum Hall Thermometer . . . . .	80
5.5	Electrical Noise as a Limiting Factor for Reaching $\mu\text{K}$ Temperatures . .	83
5.5.1	Metallic CBT . . . . .	85
5.5.2	Quantum Dot Coulomb Blockade Thermometry . . . . .	87
<b>6</b>	<b>Longitudinal Resistance Quantization and Density Gradient in the Integer Quantum Hall Regime</b>	<b>89</b>
6.1	Introduction . . . . .	90
6.2	Experiment . . . . .	91
6.2.1	Samples . . . . .	92
6.2.2	Magnetic Field Dependence . . . . .	93
6.2.3	Asymmetry in Magnetic Field . . . . .	96
6.2.4	Temperature Dependence . . . . .	98
6.2.5	$\nu = 5/2$ State Gap Characterization . . . . .	99
6.3	Discussion . . . . .	102
<b>7</b>	<b>Evidence for Disorder Induced Delocalization in Graphite</b>	<b>104</b>
7.1	Introduction . . . . .	105
7.1.1	Overview . . . . .	106
7.2	Experimental Techniques . . . . .	107

7.2.1	Sample Fabrication . . . . .	107
7.2.2	Measurements . . . . .	108
7.3	Results . . . . .	109
7.3.1	Thickness Dependence . . . . .	109
7.3.2	Temperature Dependence . . . . .	110
7.4	Discussion . . . . .	112
7.4.1	Disorder induced Delocalization . . . . .	112
7.4.2	Non-monotonic Temperature Dependence . . . . .	114
7.5	Conclusion . . . . .	115
7.6	Supplementary Information . . . . .	116
7.6.1	Geometry of Nano Graphite Flakes . . . . .	116
7.6.2	Numerical Simulation of Current Distribution . . . . .	117
7.7	Acknowledgements . . . . .	122
<b>8</b>	<b>Conclusion &amp; Outlook</b>	<b>123</b>
	<b>References</b>	<b>125</b>
	<b>List of Figures</b>	<b>141</b>
<b>A</b>	<b>Curriculum Vitae</b>	<b>143</b>

# 1 Introduction

Ever since Max Planck put forward quantized units of energy [1], quantum physics has truly revolutionized physics, helping to understand the microscopic workings of our universe. To this day in particle physics novel elementary particles are predicted and detected [2]. But quantum physics has also shaken up condensed matter physics, as many properties of condensed matter can only be accurately described with quantum mechanical principles [3]. Besides band theory, the introduction of quasiparticles in order to describe collective behavior in a solid has been amongst the most successful approaches. The reason might be that the quasiparticle description captures the essentials of collective behavior, but still employs a simple particle picture. Bosonic phonons as fundamental excitation of lattice vibration are needed to explain the lattice heat capacity and its temperature dependence [4]. Mass-renormalized quasiparticle in Landau-Fermi liquids[5] are able to capture the interaction between electrons and thus predict many properties of an interacting electron gas, e.g. the  $T^2$  dependence of electrical conductivity in a metal at the lowest temperatures [3].

In the meantime, condensed matter physics can be considered the modern playground for particle physics, as efforts of many research groups concentrate on investigating novel types of quasiparticles within the solid state, inspired by concepts and ideas which have been around for a long time. Additionally, the solid state offers many more possibilities to realize novel types of states of matter - tailored quasiparticles, designed on paper or fortuitously discovered in exotic materials. Composite fermions [6], heavy fermions [7, 8], Dirac fermions [9, 10], Majorana fermions [11, 12], Bose condensates [13, 14] of pure bosons and paired fermions, topologically trivial or non-trivial[15–17] and even particles with non-integral statistics [18, 19] have been predicted and some of them observed in condensed matter systems. Instead of building a huge accelerator, one “only” has to ensure that within a solid the energy separation between the many-body ground state and the first excited state is large compared to all other energy

scales. This can either be done by choosing materials wisely or even synthesize them purpose specific, such that the energy protection of the collective ground states is large enough. Another approach is to reduce the magnitude of all other involved energies, namely by reducing temperature. Low temperature physics has always been promoting discoveries of collective behavior from superconductivity [20], Kondo physics [21, 22] to superfluidity in  $^4\text{He}$  [23] and more surprisingly in  $^3\text{He}$  [24].

By now, experimental studies of quantum effects are not restricted to macroscopic manifestations anymore. Modern measurement techniques have enabled observation and manipulation of single atoms. Further, progress in fabrication techniques has promoted creation of a plethora of nanostructured devices with energy scales within reachable experimental temperatures [25, 26], allowing for the creation of artificial, tunable atoms [27], offering a versatile instrument to investigate the meso- and nanoscopic behavior of electrons and their coupling to the environment.

Simultaneously to the advancement of device fabrication allowing wide tunability, quantum mechanics has changed another discipline in the last decades: Information technology. On the one hand side transistor sizes approach the quantum realm, but more importantly it has been postulated that algorithms harvesting the properties of entangled superpositions of quantum states will outperform classical algorithms in certain tasks [28]. The fundamental constituent of such a quantum computer is a so called quantum bit (qubit), which has to be manipulated coherently. The proposed physical implementation of qubits are manifold, among them are photons [29], trapped ions [30] or currents in superconducting LC circuits [31]. Another promising candidate are electrons with their charge [32] or their spin [33], confined to nanostructures. The electron based realizations often require low temperatures, as coupling to the environment is strong due to the electronic charge. This makes the qubit more vulnerable to its surrounding, but also easier to manipulate and read-out. The electron spin on the other hand offers a more protected qubit basis. Among the fundamental questions for the development of a quantum computer is how and how fast the qubit decoheres [34].

---

For the case of electrons, it has been found that the inverse of the decoherence time scales with a power law in temperature [35], again suggesting benefits from low electron temperatures. For electron spin qubits, nuclear spin fluctuations in the host material have been identified as the main decoherence mechanism. Lower temperatures would allow for larger nuclear spin polarizations. For a two dimensional GaAs/GaAlAs heterostructure, it has even been predicted that below  $\sim 1$  mK the nuclear spins should align ferromagnetically due to an electron mediated interaction between the nuclei [36, 37], suppressing fluctuations completely. Such a phase transition is of course interesting in its own right, as the transition temperature is supposed to be electron density dependent, and constitutes another new state of matter.

Motivated by the ample reasons to explore unprecedented low temperatures, this thesis describes the effort to reduce electron temperatures in metallic and semiconducting nanostructured samples using an adiabatic nuclear refrigeration technique. In chapter 2 first an introduction to fundamental cryogenic principles and relations will be given and then the implementation and performance of the experimental apparatus aimed at cooling electrons in typical devices to sub-millikelvin temperatures will be described. In Chapter 3 electron thermometry experiments with Coulomb blockaded metallic structures will be presented and limitations of the cooling technique are discussed. Experiments investigating deep Coulomb blockade thermometry in quantum dots are presented in chapter 4, including a discussion about the thermometer limitations. Chapter 5 describes an improved setup and subsequent experiments, demonstrating that electrons in metallic structures cool to  $\sim 5$  mK. Measured devices include both Coulomb blockade thermometers (CBT) and normal/insulator/superconductor (NIS) junctions. Finally also the cooling of electrons in a two-dimensional electron gas (2DEG) below the base temperature of the dilution refrigerator is shown by means of reentrant features in quantum Hall measurements. A recent experiment on high mobility 2DEGs is described in chapter 6, where the detrimental effects of density gradients in the detection of the exotic  $\nu=5/2$  state are investigated. Chapter 7 discusses our

possible evidence of bulk disorder induced lifting of Anderson localization along the c-axis in the layered material graphite, yet another interesting state of matter – already known for a long time, but surprisingly still not understood today.



---

## 2 Nuclear Refrigeration for Nanoelectronics

Due to the decoupling of different degrees of freedom at the lowest  $T$ , a key ingredient for reaching unprecedented electron temperatures in semiconductor devices is the actual refrigeration technique. Commercially available dilution refrigerators can reach base temperatures of below 10 mK. With home-built, optimized setups, even temperatures of 2 mK can be reached in continuous operation mode. Our approach is a different one, as we adopt the well established technique of adiabatic nuclear demagnetization (AND) for cooling [38–40]. AND is used to achieve the lowest temperatures in condensed matter, it is a single shot technique, but allows in principle to cool the coldest part in the refrigerator to  $\leq 100 \mu\text{K}$ , potentially reducing temperature by factor 100 or even more compared to a commercial DR. Double demagnetization stages can be used to achieve even lower temperatures. Using this technique the lowest electron temperature reported to date is 1  $\mu\text{K}$  in Pt [41], for the nuclear system the record stands at 300 pK reached in Rh nuclear spins [42]. Another beneficial effect is that coupling the electronic system to a nuclear refrigerator (NR) at the lowest temperatures is much easier than coupling it to the  $^4\text{He}/^3\text{He}$  mixture in a DR, as NRs can be chosen to be metallic. Although the scope of this thesis is rather coupling electrons in semiconductors to the coldest part of a given refrigerator, we first have to establish successful AND. After outlining the physical principles governing heat transport at low  $T$ , an introduction to the working principle of AND will be given and the design of the home-built nuclear demagnetization unit will be presented. In the second part of this chapter the demagnetization stage performance is discussed by means of heat leaks, lowest temperatures reached and demagnetization efficiency.

## 2.1 Thermal Conductance of Solid Matter

### 2.1.1 General Concepts

In a cryogenic apparatus the coldest parts are inevitably connected to room temperature and heat will flow accordingly. In order to build a refrigerator, it is very important to understand how all parts of the refrigerator are coupled to each other. Heat flow is described by a linear response theory, where a potential gradient (temperature) causes a flow of a current (heat). The linear relation between the two is characterized by a constant (heat/thermal conductivity). Elementary excitations can carry energy and therefore will participate in thermal conductance in order to equalize the energy difference. Among these excitations are electron and phonons, but also more exotic particles like magnons and neutral modes in quantum Hall edge states [43]. Because the elementary excitation can differ for different materials, the heat conductivity is depending on the specific material. Thus an appropriate choice of materials is paramount for proper operation of the experimental apparatus at  $T \ll 1$  K. We will first discuss some mechanisms of heat transport for different material types and then discuss what happens at material interfaces.

### 2.1.2 Heat Conductivity

The rate of heat flow per unit area resulting from a temperature gradient can be written as

$$\dot{q} = -\kappa \nabla T. \tag{2.1}$$

As the transport of heat carriers, i.e. elementary excitations, is usually not ballistic, heat conduction is a diffusive process. By applying transport theory in its simplest form (i.e. kinetic gas theory) one finds for the thermal conductivity

$$\kappa = \frac{1}{3}c_m v \lambda = c_m v^2 \tau, \quad (2.2)$$

where  $c_m$  is the the molar heat capacity,  $\lambda$  is the mean free path,  $\tau$  the scattering rate and  $v$  is the velocity of the particles. We are now interested in the temperature dependence of Eq. 2.2 especially in the low temperature regime.

Considering phonons, it is important that at low temperatures the sound velocity is independent of temperature [44]. According to the Debye Model, the molar vibrational heat capacity due to phonons  $c_{ph} \propto \frac{T^3}{\Theta_D}$ , where  $\Theta_D$  is the Debye temperature. For  $T \ll \Theta_D$ , the number of thermally excited phonons is small, thus the mean free path is not dominated by phonon-phonon scattering, but rather by scattering at crystal defects and boundaries. It turns out that for the case of dominant scattering at crystal irregularities the mean free path is temperature independent, such that  $\kappa_{ph} \propto T^3$ .

In the case of electrons, the Fermi velocity is temperature independent as well. Below the Fermi temperature, the molar heat capacity of free electrons decreases linearly with temperature,  $c_e = \gamma T$ , where  $\gamma$  is the Sommerfeld constant. Below the Debye temperature, electron scattering with lattice defects and impurity dominates, as the number of phonons is small and thus  $\lambda$  is temperature independent as well - hence  $\kappa_e \propto T$ . The two channels of heat conductance are additive. Because of the lack of free electrons, in insulators  $\kappa_{ph}$  dominates and becomes rather weak at the lowest temperatures due to its cubic  $T$  dependence. In superconducting metals there are also no free electrons available at the Fermi energy because of the superconducting gap  $\Delta$ . Only the phonons and the remaining quasiparticles, which are exponentially suppressed at temperatures below the critical temperature  $T_C$ , can contribute to the thermal conductance. Hence below the critical temperature  $T_c$  of the superconductor the thermal conductance approaches the conductance of an insulator with the cubic  $T$  dependence. In normal metals on the other hand, heat conduction is typically dominated by electrons, providing a rather good thermal conductance at the lowest  $T$ . The dominance of electronic heat conduction manifests itself in a particular nice way

through the Wiedemann-Franz law, which relates thermal conductivity and electrical conductivity. It allows for an easy determination of the thermal conductivity of a metal by measuring the electrical conductivity. This is helpful as thermal conductivity measurements are typically rather involved. In the defect scattering limit (i.e. at lowest  $T$ ) the mean free path is not temperature dependent. This means that the electrical conductance is constant. The  $T$  dependence of the thermal conductivity is solely carried by the heat capacity  $c_e$ , which is linear in temperature. Thus the ratio between thermal and electrical conductivity should be proportional to  $T$ . For a more qualitative consideration take a density  $n$  of electrons with effective mass  $m^*$  in a metal. Due to the Fermi-Dirac distribution around the Fermi energy ( $\epsilon_F$ ), we can use the relations  $v_F^2 = \frac{2\epsilon_F}{m^*}$  and  $c_e = \frac{\pi^2}{2} \frac{k_B T}{\epsilon_F} n k_B$ . Further by plugging into Eq. 2.2, we find

$$\kappa = \frac{\pi^2}{3} \frac{\tau}{m^*} k_B^2 n T. \quad (2.3)$$

By employing the Drude electrical conductivity  $\sigma = \frac{ne^2\tau}{m^*}$  the relation of thermal and electrical conductivity can be written as

$$\frac{\kappa}{\sigma} = \frac{\pi^2}{3} \frac{k_B^2}{e^2} T = L_0 T, \quad (2.4)$$

where  $L_0$  is the Lorenz number. Due to more exotic scattering mechanisms (e.g. the Kondo effect) this temperature dependence can be altered at the lowest temperatures and it has been observed that the Lorenz number can vary for different types of metals for various reasons [39]. In summary, plugging Eq. 2.4 into Eq. 2.1, the electronic contribution to the heat flow between two points at electron temperatures  $T_{e,1}$  and  $T_{e,2}$  is

$$\dot{Q}_e = \frac{\pi^2 k_B^2}{6e^2 R} (T_{e,1}^2 - T_{e,2}^2), \quad (2.5)$$

where  $R$  is the electrical resistance between the two points. Generally, it is clear that

in order to achieve the highest thermal conductance, often desired in low temperature experiments, one should use the highest purity metals, as in those defect scattering is suppressed. An easy method to characterize the purity of metals is through their electrical resistance. By measuring the electrical resistivity  $\rho$  both at room temperature, where it is dominated by phonon scattering and at 4.2 K, where impurity scattering dominates, one can extract the residual resistivity ratio ( $RRR$ )

$$RRR = \frac{\rho_{300\text{ K}}}{\rho_{4.2\text{ K}}}. \quad (2.6)$$

## 2.2 Cooling of Solid Matter

Cooling an object involves putting it into thermal contact with a colder reservoir. The temperature gradient will cause energy to flow from the object with the larger temperature towards the reservoir with a lower temperature. The thermal equilibrium temperature of the object to be cooled is determined by the rate of heat flow, the thermal conductivity  $\kappa$  and the heat leaking into the object -  $Q_0$ . This assumes of course that the reservoir is large enough, or that the heat is efficiently and continuously removed so that it keeps the initial temperature.

### 2.2.1 Thermal Boundary Resistance

So far we have considered the heat conductivity within a material. Often one has to combine different materials in an experimental apparatus for practical reasons. At the interface between materials different effects come into play. The thermal boundary resistance, or Kapitza resistance,  $R_K$  is also temperature dependent. For non noble metals like Cu or Al usually a oxide layer covers the surface, which is detrimental for the thermal conductance across this boundary. For Al, the oxide layer is almost unavoidable, thus it is very inefficient to bring materials just in contact with Al, they should be fused together instead. The Cu surface slowly degrades over time. A way

to prevent oxidation is to cover Cu with a more noble metal like Au. With this Au plating technique, a pressed contact can stay efficient for very long time. Generally the preferred contact types for permanent connections between materials are fused or welded joints as they provide much better thermal contact.

An especially high thermal resistance is observed between liquid helium and metals, because of the large sound velocity difference. Hence an acoustic mismatch exists at liquid helium-metal interfaces. As the work horse of low temperature physics is the dilution refrigerator (DR), where a liquid helium mixture is the coldest point, this is a very important technical concern. Snell's law of refraction for phonons is

$$\frac{\sin \alpha_h}{\sin \alpha_s} = \frac{v_h}{v_s}, \quad (2.7)$$

for the angles  $\alpha$  at which the phonons cross the boundary. Because the sound velocity in helium  $v_h$  is roughly a factor 10 smaller than the phonon velocity in the solid ( $v_s$ ), the critical angle for total reflection is  $\theta_c \sim 3^\circ$ ; above this angle phonons from the helium cannot enter the solid. Taking the angle distribution and in addition the transmission coefficient into account, it turns out that only a very small fraction of phonons from the helium can enter the solid (one per  $\sim 10^5$  [5]). Therefore the cold helium and the surrounding pieces are rather inefficiently coupled. Additionally it can be shown that for liquid helium-metal interfaces  $R_K \propto A^{-1}T^{-3}$ , where  $A$  is the contact area. As a consequence, to allow for efficient thermal coupling at the DR base T, the contact area between liquid helium can be increased i.e. by surface roughening of the metal or by using metal sinters [45].

### 2.2.2 Electron-Phonon Coupling

Interestingly, as thermal conductance generally is reduced with temperature, the different degrees of freedom within a material tend to become decoupled at the lowest temperatures. The different systems of elementary excitation can then individually be

described because they reach equilibrium among themselves on a much faster time scale than coupling to other degrees of freedom. For example in the case of electron-phonon coupling the heat flow is given by

$$\dot{Q}_{e-ph} = \Sigma\Omega(T_{ph}^5 - T_e^5), \quad (2.8)$$

where  $\Omega$  is the volume and  $\Sigma$  is the material dependent electron-phonon coupling constant [44]. Due to the strong temperature dependence at the lowest temperatures the heat flow is suppressed between electrons and phonons. It thus becomes increasingly difficult to cool the electron system through lattice phonons at lower temperatures, as for example in a DR. It may be that phonons are at much lower temperatures, while the electron temperature lies well above that, due to a small heat leak. For the implementation of a refrigerator for low electron temperatures it is more desirable to cool the electrons through a different system. Fortunately, the coupling between nuclei and conduction electrons is much more efficient down to low temperatures. The coupling mechanism is due to electromagnetic interaction between the magnetic moments of electrons and nuclei, the so called hyperfine interaction. This can be used in a so called nuclear demagnetization stage, as described below.

## 2.3 Adiabatic Nuclear Demagnetization

The thermodynamics of the nuclear demagnetization for our purposes is completely described by a non-interacting ensemble of nuclei with spin  $I$  and magnetic moment  $\mu_n$  subjected to a magnetic field  $B$ . The Zeeman energies of the different spin states are given by

$$E_{Z,m} = -m\mu_n g_n B \quad (2.9)$$

where  $g_n$  is the nuclear g-factor and the magnetic quantum number  $m$  runs from  $-I$  to  $+I$ . One can then write in the high temperature limit ( $k_B T \gg E_{Z,m}$ ) the molar nuclear spin entropy as

$$S_n = R \ln(2I + 1) - \frac{\lambda_n B^2}{2\mu_0 T_n^2} \quad (2.10)$$

where  $R$  is the molar gas constant,  $\mu_0$  is the vacuum permeability,  $T_n$  the nuclear temperature and  $\lambda_n$  the molar Curie constant. From the relation  $C_B = T \left( \frac{\partial S}{\partial T} \right)_B$ , one finds the Schottky law for the nuclear specific heat

$$C_{n,B} = \frac{\lambda_n B^2}{\mu_0 T_n^2}. \quad (2.11)$$

Notably both the entropy and the specific heat are functions of  $(B/T)$  only.

AND is a single shot technique, which can be divided into three sub steps. First the NR is exposed to a high magnetic field of several Tesla ( $B_i$ ). The heat of magnetization generated by the polarization of the nuclear spins is removed by a continuously operating refrigeration technique, typically a DR, which has to be thermally coupled to the NR very well. Precooling the NR to an initial temperature ( $T_i$ ) builds up a significant spin polarization, resulting in a reduction of the nuclear spin entropy, according to Eq. 2.10. Then the DR and the NR are thermally decoupled with a so called heat switch, otherwise heat will leak into the NR from the DR. In the last step, the demagnetization field is ramped down very slowly to a final field  $B_f$  at nuclear temperature  $T_f$ , in order to preserve the nuclear spin population. During an ideal adiabatic process, the nuclear spin entropy then stays constant  $S(B_i/T_i) = S(B_f/T_f)$ , which results in

$$\frac{B_i}{T_i} = \frac{B_f}{T_f}. \quad (2.12)$$

Therefore for a given precooling temperature  $T_i$  the ratio between initial field and final field determines the final temperature. One cannot demagnetize to arbitrarily low  $B_f$  because of the internal field of the NR. Secondly, at the lowest temperatures the condition  $k_B T \gg E_{Z,m}$  does not hold and internal interactions will align the magnetic moments. Generally the two restrictions are avoided in our experiments as we keep



$B_f$  above several tens of mT. For these fields  $E_{Z,m} \sim 40 \mu\text{K}$ , which is well above the lowest temperatures achieved in our setup ( $T_f \sim 180 \mu\text{K}$ ). As will be shown below the residual heat leak of the system stops us from demagnetizing to fields comparable to the internal field of Cu (0.4 mT) – the NR warm up before reaching this  $B$ -field scale.

### 2.3.1 Coupling of the Nuclear Spins to the Environment

The spin-spin relaxation time needed to establish thermal equilibrium among the nuclei,  $\tau_2$ , is very short ( $\tau_2 \sim 1$  ms for typical metals) [39]. Thus one can assume thermal equilibrium among the nuclei with the temperature  $T_n$ . In order to cool the electronic system, a thermal equilibrium has to be reached between the different heat reservoirs in the NR. As described above, at the lowest temperatures different reservoirs typically tend to be rather well decoupled. Fortunately, the coupling between nuclei and conduction electrons is efficient down to low temperatures. The hyperfine interaction is the electromagnetic interaction between the magnetic moments of nuclei and electrons. The dominant hyperfine term is the Fermi-contact interaction for electrons with a finite charge density at the site of the nucleus. Thus in metals with valence electrons in the s-shell, hyperfine coupling is especially strong. Generally, only conduction electrons near the Fermi energy can interact with the nuclei, because the electron has to have an accessible empty energy state at the energy difference corresponding to the small energy exchanged with the nucleus. Because of this participation of electrons close to the Fermi edge only, the time  $\tau_1$  the nuclei need to come into equilibrium with the conduction electrons can be linked to the electron temperature  $T_e$  through the Korringa law

$$\tau_1 T_e = \kappa, \quad (2.13)$$

where  $\kappa$  is the Korringa constant, a material parameter describing the strength of the hyperfine coupling. For insulators there are no conduction electrons, therefore the Korringa constant gets very small, rendering time scales very long ( $\tau_1 \gg 1$  day at

temperatures below 1 mK). Superconductors suffer from the same problem as at the Fermi energy there are no energy states available. For normal metals, the Korringa constant is higher, especially for metals with s-orbital conduction electrons, making the relaxation times experimentally accessible ( $\tau_1 \sim 1\text{h}$ ). Thus only metals are suitable for nuclear refrigeration.

So far we only considered the situation where the electrons sit at a constant temperature  $T_e$  and the nuclei equilibrate to this electron temperature. If one considers the actual case of nuclear refrigeration, where the cold nuclei have to pull the hotter electrons to lower temperatures, both temperatures  $T_n$  and  $T_e$  will change. The heat flow between the two baths is given by

$$\dot{Q} = nC_e\dot{T}_e = -nC_{n,B}\dot{T}_n, \quad (2.14)$$

where  $C_e$ ,  $C_{n,B}$  is the specific heat of the conduction electrons and the nuclei respectively and  $n$  is the number of moles of the NR.

With the definition of the spin relaxation time ( $\frac{dT_n^{-1}}{dt} = -\frac{T_n^{-1}-T_e^{-1}}{\tau_1}$ ) and the Korringa law (2.13) one finds for the rate of change of the nuclear temperature

$$\dot{T}_n = \frac{(T_e - T_n)T_n}{\kappa}. \quad (2.15)$$

By plugging this into Eq. 2.14, the rate of change of temperature for the conduction electrons becomes

$$\dot{T}_e = -(T_e - T_n) \left( \frac{T_n C_{n,B}}{\kappa C_e} \right). \quad (2.16)$$

This results in an altered relaxation time, such that the effective time constant becomes

$$\tau_1^{eff} = \frac{\tau_1 C_e}{C_{n,B} + C_e} \approx \frac{\tau_1 C_e}{C_{n,B}}, \quad (2.17)$$

the approximation is justified because the  $C_e$  is much smaller than  $C_{n,B}$  in an external magnetic field  $B$ . For the same reason  $\tau_1^{eff}$  is much shorter than  $\tau_1$ , thus the conduction

electrons follow the nuclear spin temperature rather quickly, while  $T_n$  stays almost constant.

### 2.3.2 Influence of an External Heat Load

In a more realistic scenario the demagnetization is not a reversible and non-adiabatic process, because of an external heat load. Heat will flow from the outside to the electrons and from there to the nuclei. This results in a temperature gradient between the electrons and the nuclei, finally causing both systems to warm up. The cooling capacity of the nuclei is given by

$$\int \dot{Q} dt = \int n C_{n,B} dT. \quad (2.18)$$

From the rate of change of the nuclear temperature (2.15) and the definition of the nuclear specific heat one finds

$$\dot{Q} = n C_{n,B_f} \dot{T}_n = (T_e - T_n) \frac{n \lambda_n B_f^2}{\mu_0 \kappa T_n}. \quad (2.19)$$

This can be rewritten as

$$\frac{T_e}{T_n} = 1 + \frac{\mu_0 \kappa \dot{Q}}{n \lambda_n B_f^2}, \quad (2.20)$$

thus  $T_e$  is lifted above the nuclear temperature when a heat load is present, and the effect is most pronounced at low final demagnetization fields. Due to the reduction in heat capacity at lower fields and the heat leak there exists an optimum in  $B_f$  for which the electron temperature is minimal, which is given by:

$$B_{f,opt} = \sqrt{\frac{\mu_0 \kappa \dot{Q}}{n \lambda_n}}. \quad (2.21)$$

Another important property of a nuclear demagnetization stage is the time it can stay

below a certain temperature, as due to the finite heat leak, both the electrons and the nuclei will heat up with time. Because the rate of change of the nuclear temperature is given by

$$\dot{T}_n = \frac{\dot{Q}}{nC_{n,B_f}}, \quad (2.22)$$

the time to warm-up the nuclei from temperature  $T_{n,1}$  to a higher temperature  $T_{n,2}$  can be expressed as

$$t = \left( \frac{n\lambda_n B_f^2}{\mu_0 \dot{Q}} \right) (T_{n,1}^{-1} - T_{n,2}^{-1}). \quad (2.23)$$

This relation can be very useful. For a given  $B_f$  the heat leak into the NR can be estimated from the time  $t$  it takes to warm up the nuclei. Further, if for some reason reliable thermometry is not possible at the lowest temperature, the temperature can be estimated with Eq. 2.23, if a known amount of heat is applied to the NR [40].

### 2.3.3 Practical Considerations

A suitable nuclear refrigerant has to meet several criteria. Of course, a considerable part of the NRs' isotopes should possess a nuclear spin  $I > 0$  and a large as possible nuclear Curie constant  $\lambda_n$  for a large specific heat and thus a large cooling power. As discussed above, an efficient coupling between the nuclei and the conduction electrons is needed, thus the NR should be a metal with a small Korringa constant  $\kappa$ . On the other hand the NR should not become superconducting, because of low thermal conductance and poor coupling between nuclei and electrons of the superconductor. Further the NR should not exhibit an electronic magnetic ordering transition, because the nuclei would align along this internal field. These requirements can be contradictory as high electronic density at the Fermi-edge for good coupling to the nuclei also enhances electronic magnetism and superconductivity. Further, the material should be available in high purity and easily machinable. It turns out that only few materials meet the above mentioned criteria, among them In, Nb, Cu and PrNi<sub>5</sub>. In (Nb) has a large nuclear spin ( $I = 9/2$ ), but exhibit superconductivity at fields below  $\sim 30$  mT (200 mT). Like

in many other AND experiments, in our setup Cu is used as NR, due to its reasonably large nuclear spin ( $I = 3/2$ ) and Curie constant ( $\lambda_n/\mu_0 = 3.22 \cdot 10^{-6} \mu\text{J K T}^{-2} \text{ mol}^{-1}$ ) [39]. Further, the Korringa constant is also sufficiently low ( $\kappa = 1.27 \text{ K s}$ ). Using Cu as NR allows to demagnetize to very low final fields ( $B_f \sim 10 \text{ mT}$ ) and therefore enables very low temperatures  $T_f < 50 \mu\text{K}$ . But successful demagnetization requires a very small heat load on the NR. Further, demagnetization experiments with Cu can be demanding as the precooling temperature should be on the order of  $\sim 10 \text{ mK}$  in a magnetic fields of  $\sim 8 \text{ T}$ . If experiments have less stringent requirements for the lowest temperatures,  $\text{PrNi}_5$  can be a better choice. Due to its large hyperfine enhancement  $\text{PrNi}_5$  demagnetization stages can reach  $T_f \sim 0.4 \text{ mK}$  with less demanding constraints on superconducting solenoids and precooling temperature ( $T_i \sim 25 \text{ mK}$ ,  $B_i \sim 5 \text{ T}$ ). Recently, AND has been demonstrated on a so called pulse-tube setup with  $\text{PrNi}_5$  as NR [46].

In order to ensure an efficient performance of the demagnetization refrigerator, one should limit external heat loads to a minimum. Obvious external heat leaks include residual heat flow from the warmer parts of the refrigerator to the coldest part through residual gas particles, via the heat switch or along the mechanical support. By proper choice of materials and operation in a low pressure environment ( $p_{\text{residual}} \leq 10^{-5} \text{ mbar}$ ) these heat leaks can be reduced to below  $1 \text{ nW}$ . Because thermal radiation from higher temperatures can be much larger, all microkelvin temperature parts have to be guarded by radiation shields. Another concern is heat coupled into the low  $T$  environment by radio frequency (RF) radiation via the electrical measurement lines from room temperature. In order to avoid these effects, our measurement lines are feed through thermocoax or twisted pairs in order to attenuate radiation. Further, the sample measurement leads are equipped with low  $T$  filters (discussed in more detail below). We additionally operate the experiment in a shielded room, where no power supply is operated inside the room. All power lines and magnet leads are filtered upon entering the room. Preamplifiers operated inside the room run on an external battery.

Mechanical vibrations stemming from mechanical pumps, sound or building activities can cause heating as well. The experiment is therefore placed on a pneumatically damped table. Additional mass is placed on the table in order to reduce the resonance frequency of the system, decoupling it from higher vibrational frequencies. All gas lines, potentially mediating pump vibrations, pass through a sandbox and a concrete block to reduce these vibrations. All of these measures help to suppress eddy current heating, occurring when a time dependent magnetic field  $\dot{B}$  is inducing currents in conducting materials, i.e if parts of the refrigerator move in a magnetic field gradient. Along similar lines, we build a rigid support structure around the NR. Of course ramping during demagnetization always implies a finite  $\dot{B}$  and eddy currents consequently generate heat. In principle, there is an optimal geometry for the Cu plates, but it turns out that for sufficiently low demagnetization rates ( $\dot{B} \leq 1 \text{ T h}^{-1}$ ), dimensions of the NR of 2-3 mm are sufficient to suppress heating to an acceptable level ( $\dot{Q}_{eddy} \leq 10 \text{ nW}$ ). We therefore do not use any slitting techniques to further reduce eddy current heating. In any case, conducting loops in which changing magnetic flux gives rise to eddy currents should be minimized, thus all rings in the support structure have a nonconducting slit.

Moreover there are time-dependent, internal heat leaks, sometimes referred to as heat release. Materials containing hydrogen can release a significant amount of energy over a very long time scale, due to the so called ortho-para conversion of hydrogen [47]. Essentially hydrogen gets trapped in a metastable excited energy state at higher temperatures and only very slowly relaxes to the ground state, which emits heat to the surrounding. Therefore we try to reduce the use of hydrogen containing materials to a minimum. That means that for thermal and electric insulators, where plastic is the material of choice, we use hydrogen-free Teflon or very little epoxy or nylon. Further the NR is made from high purity, low hydrogen concentration Cu (NOSV). Another internal source of heat are relaxations of structural tunneling systems within a solid. Especially for amorphous materials like ceramics, this can be a significant contribution to the heat leak with a very broad distribution of relaxation times [5]. As will

be discussed below, it could have been the case that exactly such an effect was a major obstacle in our efforts to cool electrons to temperatures below 10 mK, underlining the paramount importance of all material and design considerations for a successful operation of a nuclear demagnetization refrigerator.

## 2.4 Design of the Refrigerator

The nuclear demagnetization unit is displayed schematically in Fig. 2.1. We follow a recent proposal and realization of a nuclear refrigerator prototype developed in our group [48]. The most important feat of the setup is that every sample wire passes through its own, separate NR (colored red, Fig. 2.1 (a)), providing excellent thermal contact between the NR and the sample, even at the lowest temperatures. It is important to keep all wires electrically isolated from each other to perform transport measurements. The presented setup consists of 21 parallel NRs, allowing for quite sophisticated transport experiments.

Each NR plate consists of 1 mol of Cu (4N,  $RRR \sim 480$ , red in Fig. 2.1 (a)), situated at the center of a demagnetizing field ( $B_{demag}$ ). On the upper side, the Cu NRs are connected with high conductivity Ag wires (5N,  $RRR \sim 1,000$ , light blue) through an Aluminum heat switch (green) to the mixing chamber (MC) of a dilution refrigerator (DR). For efficient thermalization of the Cu during precooling, the thermal resistance between the NR and the MC must be minimized. To this end we use Ag wire with 1.27 mm diameter, which are spot welded to the Cu plates, and in the MC sintered to Ag nanoparticles (light blue) [45]. The surface areas are measured with the BET method [49] and determined to be  $\sim 2.5 \text{ m}^2$  per sinter. The heat switches are “C”-shaped pieces of annealed high purity Al (5N) fused to the Ag wires on both ends [50]. The heat switch magnet is used to switch between a thermally conducting state (Al in the normal state) and a thermally insulating state (Al in the superconducting state), where the requirement on the solenoid is given by the critical field  $B_{C,Al} \sim 10.5 \text{ mT}$  [51]. The switching ratio of thermal conductances in the “closed” (normal) and the

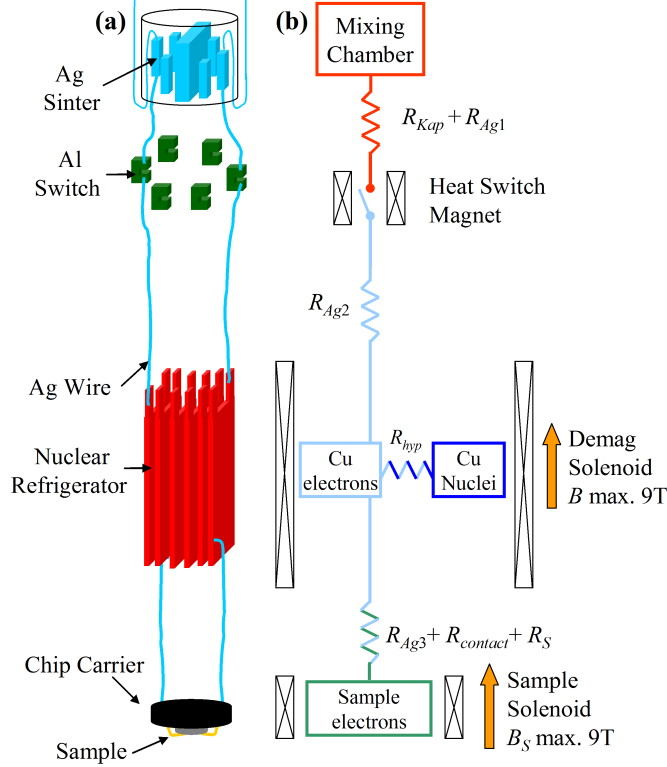


**Figure 2.1:** (a) Schematic of the Nuclear Refrigerator Setup. Only 6 NR are shown for simplicity. Each NR plate is  $0.25 \times 3.2 \times 9.0 \text{ cm}^3$ , amounting to 1 mol of Cu per plate. The distance from the bottom of the MC to the center of the Cu pieces 35 cm. (b) Cooling scheme with thermal resistances of the nuclear refrigerator setup. Different colors indicate potentially different temperatures in the steady state. Further the location of the three independent solenoid fields is indicated.

“open” (superconducting) state can reach  $10^7$  at temperatures well below the critical temperature of the superconductor [39], where excited quasiparticles are highly suppressed in the superconductor. ( $\sim 100$  mK for Al with  $T_C \sim 1.1\text{K}$ ). The Al pieces are roughly placed on a fixed radius in order to minimize differences in the stray field of the heat switch magnet. The field we apply to “close” the switches is 25 mT. Between the heat switch magnet and the demagnetization solenoid a canceled field region exists, where field sensitive devices like thermometers are placed.

On the lower side of the NRs the plates are connected by Ag wire to a ceramic chip socket (Macor, black), where a chip carrier (Macor) can be plugged into. Gold-plated metal pins ensure a press contact, resulting in an electrical resistance of  $\sim 100 \text{ m}\Omega$  at room temperature ( $RRR \sim 10$ ). The contacts of the sample are wire bonded (Au



wire, yellow) to contact pads on the chip carrier (Ti/Au, evaporated onto the Macor). A sample magnetic field ( $B_S$ , up to 9T) can be controlled independently from the demagnetization field.

For stability reasons the whole NR array is held together with dental floss and rigidly attached to a metallic support structure (not shown in Fig. 2.1), which is thermalized to the MC of the DR. Electrical and thermal insulation between the NRs and, more importantly, to the support structure is ensured through Teflon spacers. In the original design of the demagnetization stage, below the NR network, the sample socket is held in place by three Macor rods attached to the support structure for excellent thermal insulation and stabilization. In the course of transport experiments we became aware that Macor might not be a suitable low temperature material, either being responsible for a significant heat leak, or developing a high heat capacity at the lowest  $T$ , making it difficult to cool. As discussed below, in later experiments, we replace both the Macor chip socket/carrier by a silver epoxy version and the supporting rods by Vespel (SP-22) rods, because we suspect the ceramic to cause quite significant heat release, inhibiting further cooling.

Probably the weakest thermal link between the device and the NR occurs at the Schottky barriers of the metal-semiconductor contacts ( $R_{Ag3}, R_{Hyp} < R_{contact}$ , see Fig. 2.1 (b)). In steady state, the parasitic heat leaking into the device will equal the heat leaving it through the thermal links to the NRs, setting the lowest achievable temperatures. Metallic nanostructures will benefit from comparatively higher conductivity metal-metal contacts.

## 2.5 Refrigerator Performance

The MC temperature ( $T_{MC}$ ) is measured with a Cerium Manganese Nitrate (CMN) thermometer bolted to the support structure, which itself is thermally connected to the DR through its own Ag sinter in the MC. Characterization of the NRs is carried out by monitoring the electron temperature  $T_{Cu}$  of the Cu plates. Nine  $RuO_2$  chip resistors

labeled A-I are mounted on the chip carrier and electrically connected to 16 of the 21 NRs, with each resistor using a pair of NR as its leads. The chip resistors are calibrated against the MC temperature between 20 mK and 100 mK, and then temperature can be extrapolated for lower temperatures. Further two Lanthanum Cerium Manganese Nitrate (LCMN) thermometers are placed in the compensated field region and connected to an individual NR through a Ag wire. Unfortunately at the lowest temperatures all thermometers suffer from saturation ( $T_{sat,RuO_2} \sim 2$  mK,  $T_{sat,LCMN} \sim 1$  mK). This is expected in the case of the chip resistors, but rather unexpected for LCMN thermometers, as the Curie temperature for LCMN usually is below a millikelvin [52]. But a deviation from Curie-Weiss behavior below 3 mK has been reported before [53]. We suspect that a possible hydration of the paramagnetic salt causes the mediation of the dipole-dipole interaction, resulting in a higher Curie temperature [54].

In order to test the demagnetization stage properties further, we place temperature independent resistors ( $R_{heater} \sim 120 \Omega$ ) on some NRs to apply heat to specific NRs. We first characterize the demagnetization stage by means of heat leaks and precooling times. The performance of the demagnetization stage is then tested by measuring the lowest nuclear and electron temperatures. We finally chart the demagnetization efficiencies such that the final temperature can be determined from the precooling temperature.

### 2.5.1 Heat Leak

A key figure of merit of every demagnetization stage is the heat leak into the NR. One can divide these heat leaks into a static heat leaks i.e. radiation, residual heat conduction through vacuum and heat release from materials and dynamic heat leaks, i.e. eddy currents during ramping of the magnetic field. The lower the heat leak, the longer the NR can stay at the lowest temperatures and thus the longer the time window for experiments before warming up again. Further, the heat leak potentially keeps the lowest electron temperature significantly above the nuclear temperature.

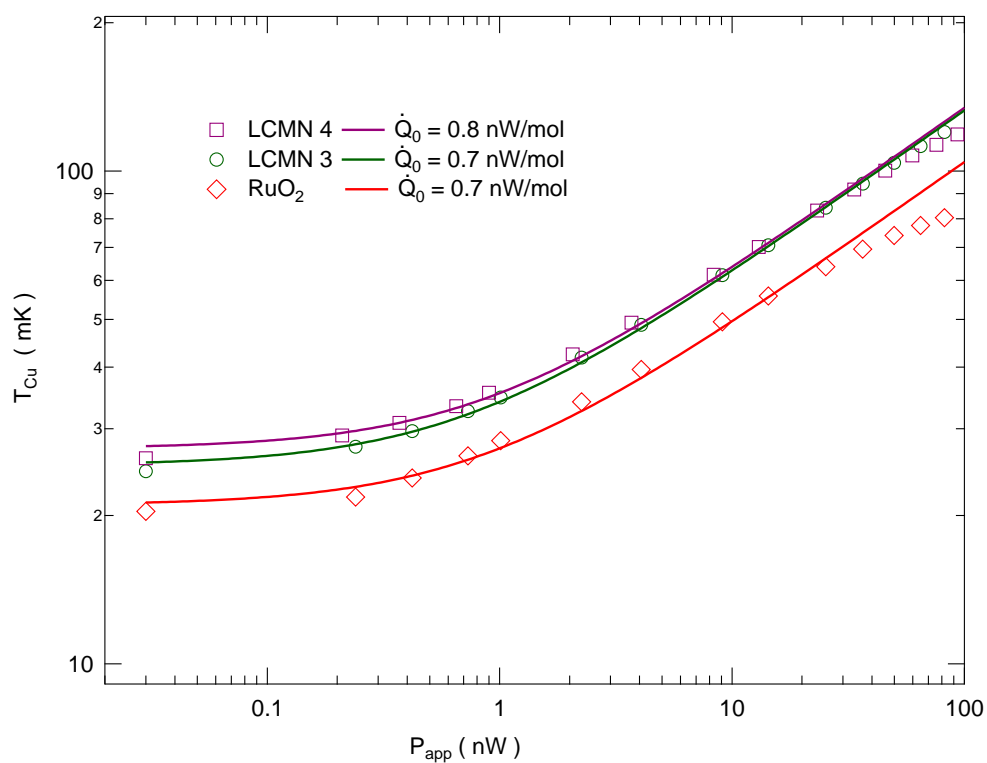


**Figure 2.2:** The temperature of the NR versus the applied power for three different NR. The markers are measurements for different LCMN thermometers (purple, green) as well as a RuO<sub>2</sub> chip resistor thermometer (red). The solid lines represent fits assuming a dominant phonon dislocation scattering mechanism ( $\kappa_{ph} \propto T^2$ ). The extracted heat leaks from the fits are on the same order of magnitude, below 1 nW mol<sup>-1</sup>

One way of measuring the residual heat leak is by applying a given amount of heat to a NR at base temperature of the dilution fridge [48]. By knowing the heat conduction mechanism one can extrapolate back to zero power applied, in order to estimate the residual heat leak  $\dot{Q}_0$ . At base  $T$ , with the heat switches in the “closed” position, the NR and the MC are at roughly the same temperature. No significantly higher temperature of the NR can be detected, which is, due to very good thermal conductance to the MC expected and a first (not very stringent) requirement for successful operation of the nuclear stage. In order to be more sensitive, the heat switches are switched to the superconducting state, decoupling the NR and the MC. Now, the residual heat leak can lift the NR temperature already significantly above the DR base  $T$  due to the highly reduced thermal conductance. In order to characterize the thermal conductance, we apply a known power  $P_{app}$  to a NR with a resistive heater placed on the NR. Further we assume a phonon dislocation scattering mechanism through the heat switch as the lowest thermal resistance between NR and MC [55]. The equilibrium situation is described by

$$P_{app} = nA (T_{Cu}^3 - T_{MC}^3) - \dot{Q}_0, \quad (2.24)$$

where  $n$  is the number of moles of Cu and  $A$  is a geometry and material dependent prefactor. By plotting  $T_{Cu}$  versus  $P_{app}$  for several applied powers, we can fit Eq. 2.24 in order to extract  $A$  and more importantly  $\dot{Q}_0$  ( $n = 1$  mol is held constant). Figure 2.2 shows so called power curves for three different NRs. Two power curves are recorded with LCMN thermometers (purple, green) and the third with a calibrated  $RuO_2$  chip resistor (red). As LCMN thermometers are not precise anymore at higher temperatures, we only fit  $T_{Cu}(P_{app})$  for  $T_{Cu} \leq 70$  mK. The phonon dislocation mechanism fits agree nicely with the data (solid lines in Fig. 2.2), although at the highest temperatures there is a deviation. This might be due to the lack in precision in the LCMN measurement, but the discrepancy also shows up in the  $RuO_2$  curve. Most likely the deviation stems from an additional heat transport channel through the heat switch, possibly due to

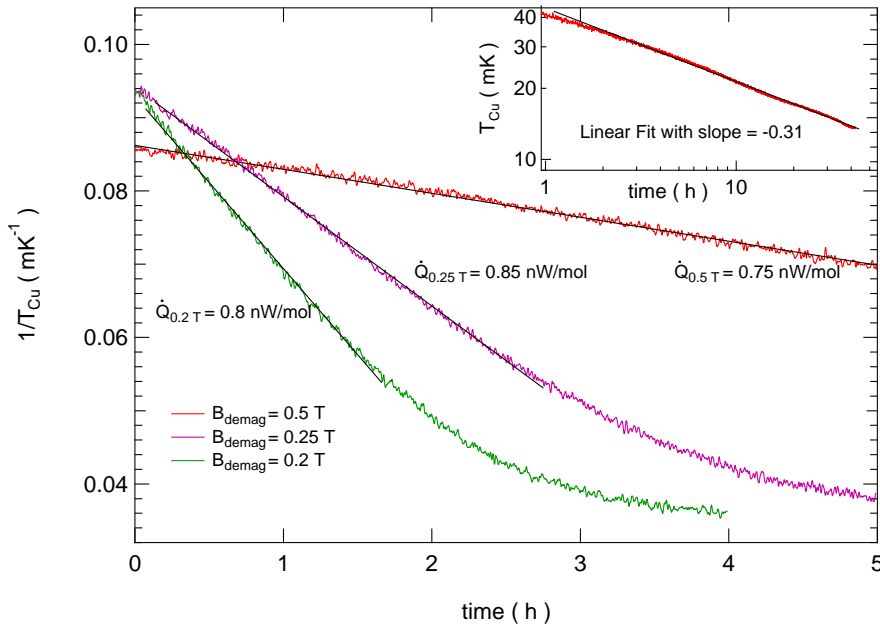


**Figure 2.3:** The inverse temperature of the NR is plotted against time for three different  $B_{demag}$ , 0.2 T (green), 0.25 T (purple) and 0.5 T (red). The solid black lines are fits using Eq. 2.23, with only the static heat leak  $\dot{Q}_0$  as a free parameter. The extracted  $\dot{Q}_0$  agree for the three different  $B_{demag}$ , are below 1 nW mol<sup>-1</sup> independent of  $B_{demag}$ . The heat switches are in the “open” state for this measurement. The inset shows the precooling of the nuclear refrigerator.  $T_{Cu}$  is plotted as a function of time, at  $B_{demag} = 9$  T and the heat switches are in the “closed” state. A linear fit to the data in the log-log plot shows a slope of -0.31, corresponding to  $T_{Cu} \propto t^{-0.31}$ , in agreement with expected behavior.

an increased number of quasiparticles at elevated temperatures. For all three fits  $A$  is  $8 \pm 1 \cdot 10^{-5}$  W mol<sup>-1</sup> K<sup>-3</sup>. The parasitic heat leak  $\dot{Q}_0$  per mol, deduced from the fit, lies between 0.7 and 0.9 nW mol<sup>-1</sup>. This is sufficiently low, but far away from the state of the art heat leak of  $\dot{Q}_0 \sim 5$  pW mol<sup>-1</sup> [56]. We suspect that most of the heat leaks through the Teflon spacers and nylon screws holding together the NR array and attaching it to the support structure [57]. Additionally, we determine the heat leak at  $B_{demag} = 0.2$  T, which is measured to be below 1 nW as well (data not shown). From field sweeps around zero  $B$ -field we estimate the dynamic heat leak, due to eddy current heating, to be  $\sim 20$  nW for a sweep rate of 1 T h<sup>-1</sup> and  $\sim 8$  nW for 0.5 T h<sup>-1</sup>.

Another way of determining the residual heat leak is to ramp the demagnetization coil to a finite field  $B_{demag} \neq 0$ , have the heat switches in the “closed” position and let the

NR precool for some time. After the heat switches are “opened”, effectively reducing the heat conduction between MC and NR by orders of magnitude, the temperature of the NR will increase due to the parasitic heat leak. The dynamics of this warm up are governed by Eq. 2.23. By plotting the inverse of the NR temperature  $T_{Cu}$  versus time, one can extract the residual heat leak by fitting a line, as the slope is given by  $-\frac{\mu_0 \dot{Q}}{n\lambda_n B_{demag}^2}$ . Figure 2.3 plots  $1/T_{Cu}$  as a function of time for three different  $B_{demag}$ . We again extract heat leaks below  $1 \text{ nW mol}^{-1}$  for all  $B_{demag}$ . At longer times the residual heat leak and the heat removed through the heat switches start to balance and the temperature saturates. For  $B_{demag} = 0.5 \text{ T}$ , due to the quadratic dependence of the heat capacity on  $B$ -field, this starts to happen after more than 9 hours.

### 2.5.2 Demagnetization Efficiency

Given a heat leak sufficiently low for nuclear cooling, we now evaluate the demagnetization process itself. After ramping  $B_{demag}$  to  $B_i = 9 \text{ T}$ , the NR heat up to  $60 \text{ mK}$  or more (depending on the exact ramp rate), but then rapidly cool below  $20 \text{ mK}$  again. After 2 days of precooling the NR reach  $T_i \sim 13 \text{ mK}$ , as displayed in the inset of Fig. 2.3. The time dependence of the precooling temperature is in good agreement with the behavior expected ( $T_{Cu} \propto t^{-1/3}$ ). This is true as long as the DR has a cooling power  $\propto T^2$ , the specific heat of the nuclei is proportional to  $T^{-2}$ , and they are connected through a metallic link with  $\kappa \propto T$  [39] (assuming that  $R_K$  does not play a role).

With  $T_i \sim 13 \text{ mK}$  accessible within 2 days, we next try to characterize the demagnetization process itself. Figure 2.4 shows the resistance of several chip resistors  $R_{RuO_2}$  during a series of ramps from  $9 \text{ T}$  to  $0.2 \text{ T}$ . The inset in Fig. 2.4 shows the parallel NR network with the corresponding chip resistors attached to them.  $B_{demag}$  is decreased linearly in time using two sequential ramps at  $1 \text{ T h}^{-1}$  from  $9 \text{ T}$  to  $1 \text{ T}$  (for most scans we stop and let equilibrate at  $5 \text{ T}$  and at  $2 \text{ T}$ ), and at  $0.125 \text{ T h}^{-1}$  from  $1 \text{ T}$  to  $0.2 \text{ T}$ .  $R_{RuO_2}$  values increase upon demagnetization, clearly indicating cooling. Further,  $R_{RuO_2}$  continues to increase between the individual  $B$ -field ramps, reflecting a thermal lag between the

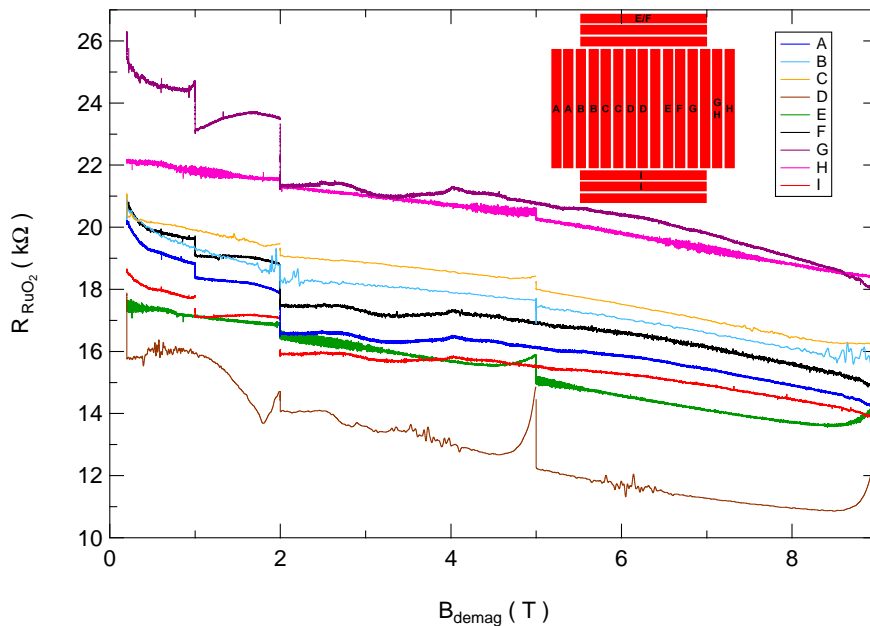


**Figure 2.4:** Resistance  $R_{RuO_2}$  of the  $RuO_2$  chip resistors versus the  $B_{demag}$  during demagnetization indicating cooling of all NRs. Inset: Arrangement of Cu plates in the parallel NR network with chip resistor and LCMN arrangement.

thermometers and the Cu plates. Looking at the rate of cooling, the  $RuO_2$  thermometers are sensitive to the ramping of the field, as cooling is faster once the magnetic field has stopped ramping (not visible in Fig. 2.4). Upon resuming ramping after a stop at constant  $B_{demag}$  some chips show a decrease in  $R_{RuO_2}$ , indicating sensitivity to eddy current heating in the NR. Applying the temperature calibration obtained at higher temperatures to  $R_{RuO_2}$  (not shown), one can extract a minimal  $T_e \sim 2$  mK for the chip resistors, but applying heat to the Cu plates demonstrates that this temperature is saturated.

We follow the approach of previous experiments and try to extrapolate the NR temperatures based on warm up curves [48]. Because of the thermal lag between NRs and chip resistors and the not so clear amount of Cu a single resistor is connected to, we focus on warm up curves measured with the LCMN. The inset of Fig. 2.5 shows the electron temperature measured by the LCMN versus  $B_{demag}$  during a demagnetization run ( $T_i = 13$  mK). As before  $B_{demag}$  is ramped linearly from 9 T to 1 T (equilibration stop at 2 T), and at  $0.125$  T  $h^{-1}$  from 1 T to  $B_f$ , for this particular demagnetization

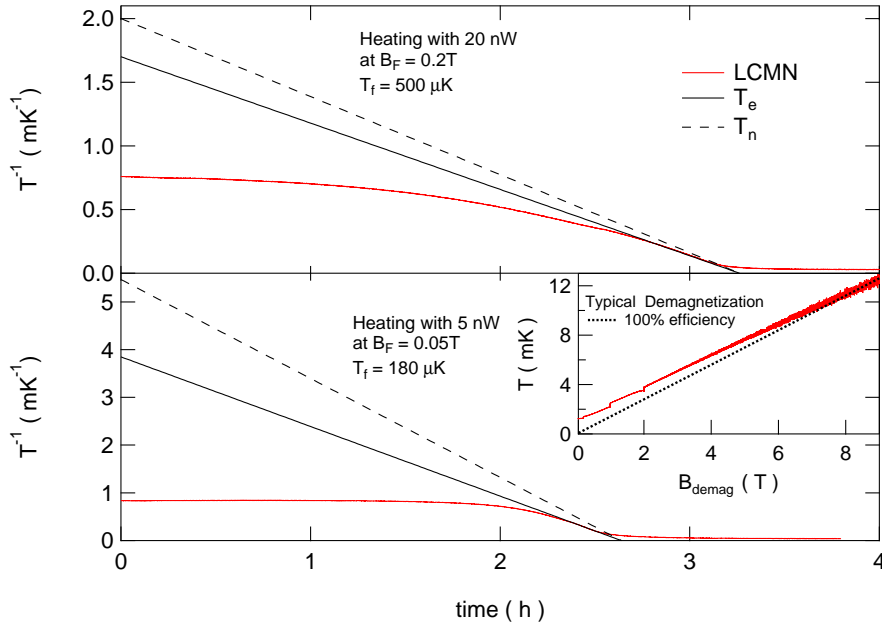


**Figure 2.5:** Measured  $T_{LCMN}^{-1}$  (red) and fitted  $T_e^{-1}$  (black) for  $B_f$  of 0.2 T while applying 20 nW (top panel) and for  $B_f$  of 0.05 T while applying 5 nW (bottom panel).  $T_n^{-1}$  (black, dashed) was calculated through  $B_f$ ,  $\dot{Q}$  and Cu material constants, see text for details. Inset: Cooling of the LCMN during demagnetization to 0.05 T, the dashed black line represents 100% efficiency.

$B_f = 0.05$  T. There is a clear deviation of  $T_{Cu}$  from the expected behaviour for a demagnetization efficiency of 100% (dashed line). As will be discussed below, this is both due to a saturation of the LCMN thermometer at low  $T$  and a manifestation of the non-adiabatic character of the demagnetization process.

We extrapolate  $T_f$  and  $T_e$  of the NRs reached after demagnetizing to  $B_f$  by plotting the inverse LCMN temperature ( $T_e^{-1}$ ) versus time  $t$  under an applied power  $\dot{Q}_{app}$  in Fig. 2.23. At first,  $T_e^{-1}$  is not showing a change at all, demonstrating the saturation of the LCMN, but then eventually decreases. The warm up is described by Eq. 2.23, where the slope of  $T_n^{-1}(t)$  is given by the ratio  $\dot{Q}/B_f^2$ . In the range in which the LCMN is not saturated (between 3 mK and 15 mK) we use a linear fit to determine  $T_e^{-1}(t)$  (solid black line in Fig. 2.5) to account for the warm-up. By calculating back to  $t = 0$ , we determine the initial  $T_e$ . From  $T_e^{-1}(t)$  and Eq. 2.20, we determine  $T_n^{-1}(t)$  (dashed black line in Fig. 2.5) and consequently  $T_f$ . Please note that we add the parasitic heat leak  $\dot{Q}_0 \sim 0.7$  nW to the applied heat, such that  $\dot{Q} = \dot{Q}_0 + \dot{Q}_{app}$ . The slope



of the “fitted”  $T_n^{-1}(t)$  agrees nicely with the slope expected from  $B_f$  and  $\dot{Q}$ . In the upper panel of Fig. 2.5 a warm-up curve after a demagnetization to  $B_f = 0.2$  T with  $\dot{Q}_{app} = 20$  nW is plotted. We extract  $T_e = 0.59 \pm 0.01$  mK and  $T_f = 0.50 \pm 0.01$  mK. It is worth noticing that at this  $B_f$ , with a heat leak of 0.7 nW, the NRs stay below 1 mK for 51 hours. Previously,  $T_e$  and  $T_f$  after demagnetizing to  $B_f$  were determined by recording the time  $t$  necessary to warm up the Cu plate completely ( $T_e^{-1}, T_n^{-1} \rightarrow 0$ ) and then employing Eq. 2.20 and Eq. 2.23 [39, 48]. We emphasize that the previously used method gives very similar  $T_e$  and  $T_f$  as we extracted with our procedure.

Finally, we try to explore the limits of the nuclear demagnetization refrigerator by demagnetizing to lower  $B_f$  ( $B_{f,opt} \sim 20$  mT). The bottom panel of Fig. 2.5 displays a warm-up curve after a demagnetization to  $B_f = 0.05$  T and  $\dot{Q}_{app} = 5$  nW. The extracted temperatures (using the method described above) are  $T_e = 0.26 \pm 0.01$  mK and  $T_f = 0.18 \pm 0.01$  mK, further demonstrating the successful operation of a parallel NR network in the sub-millikelvin range. When demagnetized to  $B_f = 0.05$  T other Cu plates behave similarly (detected with the  $RuO_2$  chip resistors). Although some chip resistors warm up when ramping to fields below  $\sim 0.2$  T, most likely because of a too high heat leak due to eddy current heating. This has already been observed in the prototype experiment [48, 58], where first thermometers would heat up at around 1 T. Thus the field range where this warm up occurs has been significantly reduced with the second generation setup, hence also lower temperatures can be achieved with the present setup.

Due to the saturation of the thermometers below 1 mK and due to the non-adiabatic character of the demagnetization, we can only determine  $T_e$  and  $T_f$  by measuring the warm-up under an applied heat. For future experiments it is not practicable though to warm up the NR right after every demagnetization run. We thus attempt to pre-chart the demagnetization efficiencies  $\xi_{B_f}(B_f) = \frac{T_i/T_e}{B_i/B_f}$  in order to predict the final electron temperatures through the precooling temperatures  $T_i$ . After several demagnetization runs we find the reproducible efficiencies:  $\xi_{5T} = 92 \pm 2\%$ ,  $\xi_{2T} = 81 \pm 2\%$ ,  $\xi_{1T} = 77 \pm 3\%$

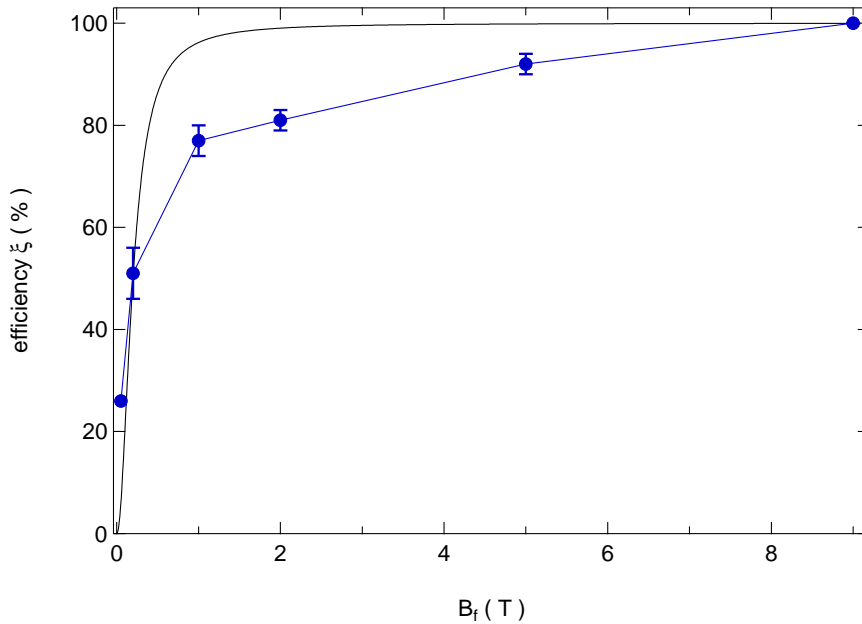


**Figure 2.6:** Demagnetization efficiency  $\xi$  extracted from warm-up curves against the final magnetic field  $B_f$  of the demagnetization run (blue markers). A theoretical curve using Eq. 2.20 and assuming a heat leak of  $\dot{Q} = 100$  nW is added (solid black line).

and  $\xi_{0.2T} = 51 \pm 5\%$ . The dependence of the efficiency  $\xi$  on  $B_f$  is displayed in Fig. 2.6 (blue). The nonadiabaticity ( $\xi < 100\%$ ) stems from the finite heat leak to the Cu plates, most likely because of eddy current heating during the ramping of the field. The nonadiabaticity becomes worse at lower magnetic fields due to the smaller heat capacity of the nuclei. The solid black line in Fig. 2.6 is the calculated  $\xi(B_f)$  using Eq. 2.20 and the definition of  $\xi(B_f)$ . For unknown reasons we have to assume an unrealistically high heat leak of 100 nW, in order to somehow reproduce the measured  $\xi$ . This is much higher than the dynamic heat leak we extracted from sweeps around zero  $B$ -field. We note that in order to find a better matching of the calculated  $\xi$  to our data, one has to incorporate a static heat leak which is  $\propto B^2$  [58]. This might be consistent with vibrations in a magnetic field gradient, causing eddy current heating. On the other hand we do not observe that the static heat leak depends on magnetic field. Thus the discrepancy between measured and calculated  $\xi$  is at present not fully understood.

---

### 3 Metallic Coulomb Blockade Thermometry down to 10 mK and below

L. Casparis, D. Maradan, A. C. Clark, C. P. Scheller,

K. K. Schwarzwälder, D. M. Zumbühl

*Department of Physics, University of Basel, CH-4056 Basel, Switzerland*

M. Meschke, J. P. Pekola

*Low Temperature Laboratory (OVLL), Aalto University, 00076 Aalto, Finland*

#### Abstract

We present an improved nuclear refrigerator reaching 0.3 mK, aimed at microkelvin nanoelectronic experiments, and use it to investigate metallic Coulomb blockade thermometers (CBTs) with various resistances  $R$ . The high- $R$  devices cool to slightly lower  $T$ , consistent with better isolation from the noise environment, and exhibit electron-phonon cooling  $\propto T^5$  and a residual heat-leak of 40 aW. In contrast, the low- $R$  CBTs display cooling with a clearly weaker  $T$ -dependence, deviating from the electron-phonon mechanism. The CBTs agree excellently with the refrigerator temperature above 20 mK and reach a minimum- $T$  of  $7.5 \pm 0.2$  mK.

### 3.1 Motivation

Advancing to even lower temperatures can open the door for the discovery of new physics: for example, submillikelvin temperatures in quantum transport experiments could lead to novel nuclear-spin physics [36, 37] in nanoscale semiconductor devices [59] or could facilitate the study of non-Abelian anyons, Majorana fermions and topological quantum computation in fractional quantum Hall samples [60, 61]. However, cooling of nanoscale devices below  $T \sim 1$  mK is a formidable challenge due to poor thermal contact as well as microwave and other heating, often resulting in device and/or electron temperatures raised well above the refrigerator temperature. Therefore, significant progress beyond the status quo in both cooling techniques and thermometry is necessary.

### 3.2 Strategy to Approach Submillikelvin Sample Temperatures

One approach to overcome these difficulties uses Ag sinters [38–40] to thermalize the sample wires [62], pioneered by the Florida group [63, 64]. Another approach — pursued by our Basel group [48] — is to use nuclear cooling [38–40] on the sample wires, with the potential to advance well into the microkelvin range. Thermometry in this regime [38–40] typically faces similar challenges as cooling nanostructures and is ideally integrated on-sample. Among numerous sensors [65], Coulomb blockade thermometers [66] (CBTs) are simple to use and self-calibrating yet offer high accuracy, demonstrated down to 20 mK [67]. Here, we present an improved nuclear refrigerator (NR) for cooling nanoelectronic samples and use it to investigate CBTs and their mechanisms of cooling.

### 3.2.1 Nuclear Refrigerator and Microwave Filtering Scheme

We employ a novel scheme for cooling electronic nanostructures into the microkelvin regime by thermalizing each sample wire directly to its own, separate nuclear refrigerator [48]. In this scheme, the sample cools efficiently through the highly conducting wires via electronic heat conduction, bypassing the phonon degree of freedom since it becomes inefficient for cooling at low  $T$ . A prototype of this refrigerator presented in Ref. [48] has been significantly improved in a second generation system, briefly outlined below and in Fig. 3.1.

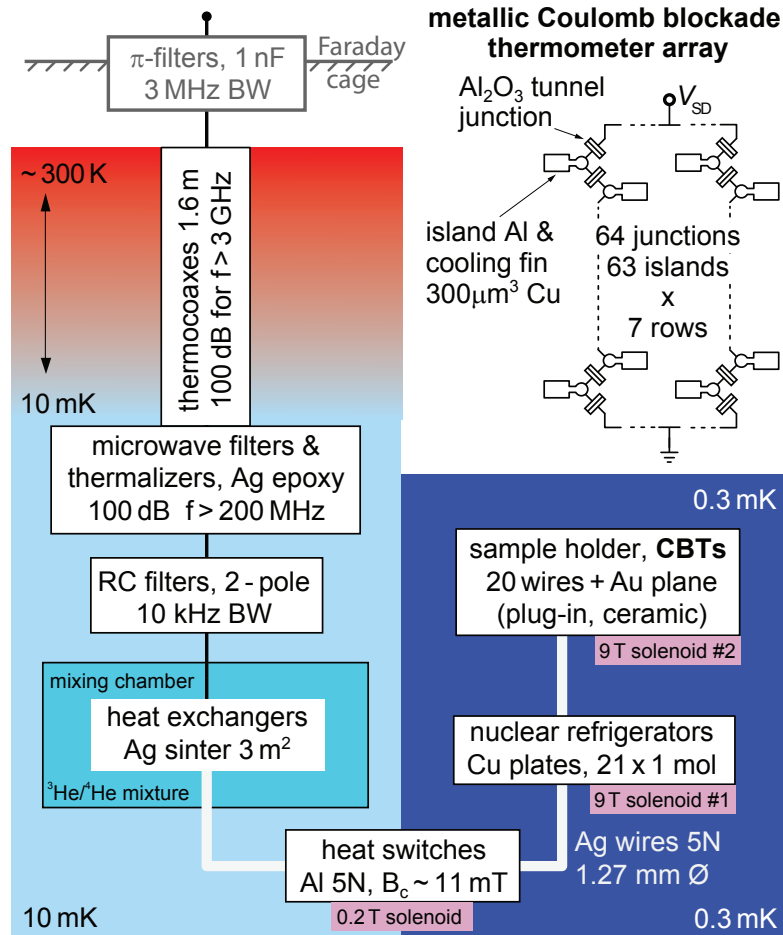


**Figure 3.1:** Layout of novel nanosample microkelvin refrigerator and CBT array. Radiation shields (not drawn) are attached to the still and cold plate ( $\sim 50$  mK). The RC filters are  $820 \Omega / 22$  nF and  $1.2$  k $\Omega / 4.7$  nF. The 21 NR plates are  $0.25 \times 3.2 \times 9.0$  cm<sup>3</sup> each, amounting to 64 g Cu per plate.

A network of 21 parallel NRs is mounted on a rigid tripod intended to minimize vi-

brational heating. Two separate 9 T magnets allow independent control of the NR and sample magnetic field.

Several stages of thermalization and filtering are provided on each sample wire (see Fig. 3.1). After  $\pi$ -filter and thermocoax [68], each lead passes through a Ag-epoxy microwave filter [69], followed by a RC filter. Each wire then feeds into a Ag-sinter in the mixing chamber, emerging as a massive high-conductivity Ag wire. After Al heat-switches with fused joints, each lead traverses a separate Cu-NR via spot welded contacts, terminating in an easily-exchangeable chip carrier plugged into Au-plated pins which are spot welded to the Ag wires. Therefore, excellent thermal contact ( $< 50 \text{ m}\Omega$ ) is provided between the bonding pads and the parallel network of 21 Cu pieces — the micro kelvin bath and heart of the nuclear refrigerator — while maintaining electrical isolation of all wires from each other and from ground, as required for nanoelectronic measurements.

### 3.2.2 Performance of the Nuclear Refrigerators

The performance of the NRs is evaluated in a series of demagnetization runs. The temperature  $T_{Cu}$  of the Cu pieces is obtained using a standard technique [39, 40, 48]: after demagnetization, we apply power on heaters mounted on some of the NRs and evaluate the warm-up time-dependence  $T_{Cu}(t)$  measured with Lanthanum Cerium Magnesium Nitrate (LCMN) thermometers above 2 mK. This allows us to determine both the temperature  $T_{Cu}$  of the Cu-NRs after demagnetization as well as a small field-offset. For each demagnetization run, the NRs are precooled to  $T_i \sim 12 \text{ mK}$  in a  $B_i = 9 \text{ T}$  magnetic field and then demagnetized to temperatures as low as  $T_f \sim 0.3 \text{ mK}$  after the field has been slowly ramped down to  $B_f \sim 0.135 \text{ T}$ , giving efficiencies  $(T_i/T_f)/(B_i/B_f) \gtrsim 60\%$ . Reruns showed excellent repeatability, allowing us to chart  $T_{Cu}$  for various  $B_f$ , depending on the precooling temperature  $T_i$ . Note that the electron temperature  $T_{Cu}$  will be, due to the finite heat leak, lifted above the nuclear temperature, therefore demagnetization efficiencies are slightly different for electron temperatures, see chapter 2. To

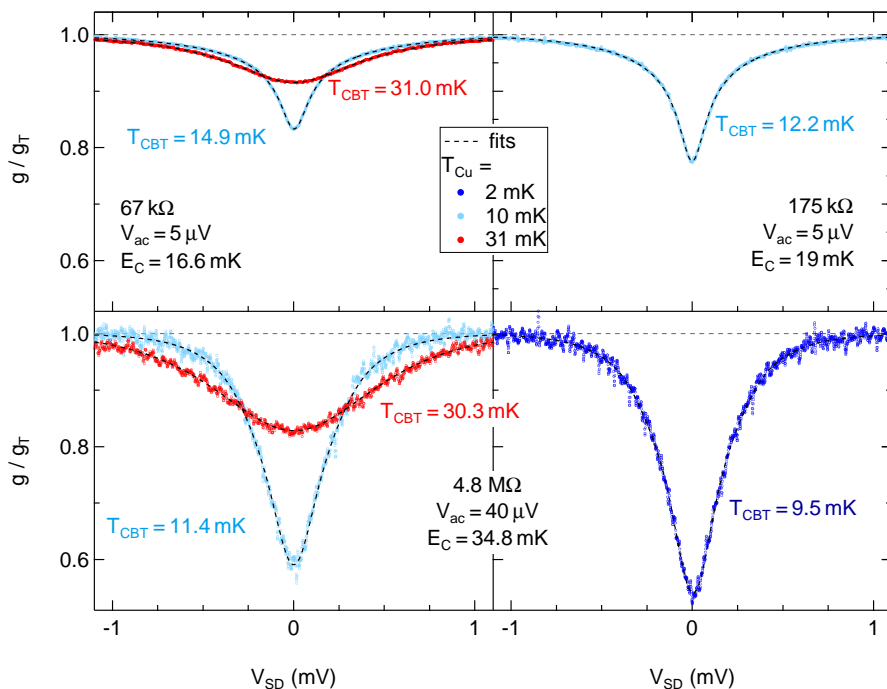


**Figure 3.2:** CBT normalized differential conductance  $g/g_T$  versus source-drain dc bias  $V_{SD}$  for various NR temperatures  $T_{Cu}$  as color-coded, with resulting  $T_{CBT}$  ( $\delta g$  method, see text) given adjacent to each trace. Data from a 67 k $\Omega$ , 175 k $\Omega$  and 4.8 M $\Omega$  CBT is shown. Dashed curves are fits to a model (see text). Note lower noise in low- $R$  sensors due to larger resulting currents.

determine  $T_{Cu}$  during the CBT experiments, we use the LCMN thermometers above 2 mK, warm-up curves at the lowest  $B_f$  and in-between, the pre-charted  $T_{Cu}$  values.

### 3.3 Electron Temperature Measurements

#### 3.3.1 CBT Sample Overview

The network with 21 NRs allows measurements of several CBTs (2-wire each). The CBT devices are Au-wire bonded and glued to the Au backplane of the chip carrier which is also cooled with a NR. Each CBT consists of 7 parallel rows of 64 Al/Al<sub>2</sub>O<sub>3</sub> tunnel-junctions in series with an area of 2  $\mu\text{m}^2$  fabricated using e-beam lithography and shadow evaporation. The process used allows oxidation at elevated temperatures, giving junction resistances up to 1 M $\Omega/\mu\text{m}^2$ . Each island extends into a large cooling fin made from Cu, since Cu gives excellent electron-phonon (EP) coupling. A small  $B \sim$

150 mT is applied perpendicular to the sensor wafer to suppress the superconductivity of the Al. The differential conductance through a CBT sensor was measured with a standard lock-in technique adding a small ac excitation  $V_{ac}$  to a dc bias  $V_{SD}$ . Note that only 1/64 of the applied voltage drops across each junction and the sensor resistance is 64/7 times the junction resistance  $R_j$ , assuming identical junctions.

### 3.3.2 CBT Performance for Different Sensors

We investigated CBTs with various  $R$ , see Fig. 3.2. Due to Coulomb blockade effects, the conductance around  $V_{SD} = 0$  is suppressed below the large-bias conductance  $g_T$ . Both width and depth  $\delta g = 1 - g(V_{SD} = 0)/g_T$  of the conductance dip are related to the CBT electron temperature  $T_{CBT}$ . To extract  $T_{CBT}$ , we perform fits (dashed curves) using a numerical model from Ref. [70]. We find excellent agreement between model and data (see Fig. 3.2). Independently,  $T_{CBT}$  can be obtained [70] from the conductance dip  $\delta g = u/6 - u^2/60 + u^3/630$  with  $u = E_C/(k_B T_{CBT})$  and charging energy  $E_C$ . We first extract  $E_C$  at high- $T$  assuming  $T_{Cu} = T_{CBT}$  and then use this  $E_C$  to extract  $T_{CBT}$  from  $\delta g$  everywhere. While both methods produce very similar  $T_{CBT}$  (deviating slightly only at the lowest  $T$ ), the  $\delta g$  approach makes no *a priori* assumptions about the cooling mechanism, allowing us an unbiased investigation, though now requiring high- $T$  calibration against another thermometer. All  $T_{CBT}$  values given here are from the  $\delta g$  method.

## 3.4 CBT Cooling Mechanism

### 3.4.1 Theoretical Model including EP and WF Cooling

The thermalization properties of  $T_{CBT}$  of the lowest and highest  $R$  CBTs are displayed in Fig. 3.3 for a wide range of  $T_{Cu}$  from 0.5 mK to 100 mK. As seen, excellent agreement is found between  $T_{CBT}$  and  $T_{Cu}$  at high temperatures, as expected. Further,  $T_{CBT}$  is seen to lie well above  $T_{Cu}$  at the lower temperatures (see Fig. 3.2 and 3.3), decoupling



fully from  $T_{Cu}$  well below 10 mK. We note that  $V_{ac}$  was experimentally chosen to avoid self-heating. Also, the 4.8 M $\Omega$  sensor reaches lower temperatures than the other, lower impedance CBTs, consistent with better isolation from the environment, since the power dissipated is proportional to  $V_{env}^2/R_j$ , with environmental noise voltage  $V_{env}$ .

To model the CBT thermalization[70], we write down the heat flow  $\dot{Q}_i$  onto a single island  $i$  with electron temperature  $T_i$ :

$$\dot{Q}_i = \frac{V_j^2}{R_j} + \sum_{\pm} \frac{\pi^2 k_B^2}{6e^2 R_j} (T_{i\pm 1}^2 - T_i^2) - \Sigma \Omega (T_i^5 - T_p^5) + \dot{Q}_0 \quad (3.1)$$

where  $\dot{Q}_0$  is a parasitic heat leak and  $V_j$  is the voltage drop across the junction, appearing here in the Joule heating term.  $\Sigma$  is the Cu EP coupling constant,  $\Omega = 300 \mu\text{m}^3$  the island volume and  $T_p$  the phonon bath temperature assumed to be equal to  $T_{Cu}$ . This is well justified by the high thermal conductance between the NRs and bonding pads. Note that at  $T \ll 1$  K, the sample-to-Au-backplane interface resistance (Kapitza) is small compared to the EP coupling resistance [70]. Within this model, two cooling mechanisms are available: Wiedemann-Franz (WF,  $T^2$  term) and EP cooling. Note the strong  $T^5$  dependence of the EP term, ultimately rendering WF cooling dominant at sufficiently low  $T$ . Assuming one mechanism and simplifying to only one island gives a saturation curve  $T_{CBT} = (T_S^p + T_{Cu}^p)^{1/p}$ , with a CBT saturation temperature  $T_S$  and an exponent  $p$ , corresponding to  $p = 2$  for WF-electron cooling and  $p = 5$  for EP cooling.

### 3.4.2 Measured Cooling Power-Laws versus Theory

We study the mechanism of thermalization by fitting the saturation curve first to the 4.8 M $\Omega$  data. We find very good agreement, giving  $p = 4.9 \pm 0.4$  (see Fig. 3.3), indicating that EP coupling presents the dominant cooling mechanism, limiting  $T_{CBT}$  to 9.2 mK even though  $T_{Cu} = 0.75$  mK. Using  $\dot{Q}_0 = \Sigma \Omega T_{CBT}^5$ , a small parasitic heat leak  $\dot{Q}_0 = 40$  aW results for each island, with  $\Sigma = 2 \times 10^9 \text{ Wm}^{-3} \text{ K}^{-5}$  from Ref. [70].

We speculate that  $\dot{Q}_0$  could be caused by electrical noise heating such as microwave radiation, intrinsic residual heat release from materials used or other heat sources. Considering the high- $R$  junctions and correspondingly weak WF cooling, it is not surprising that EP coupling is dominant here.

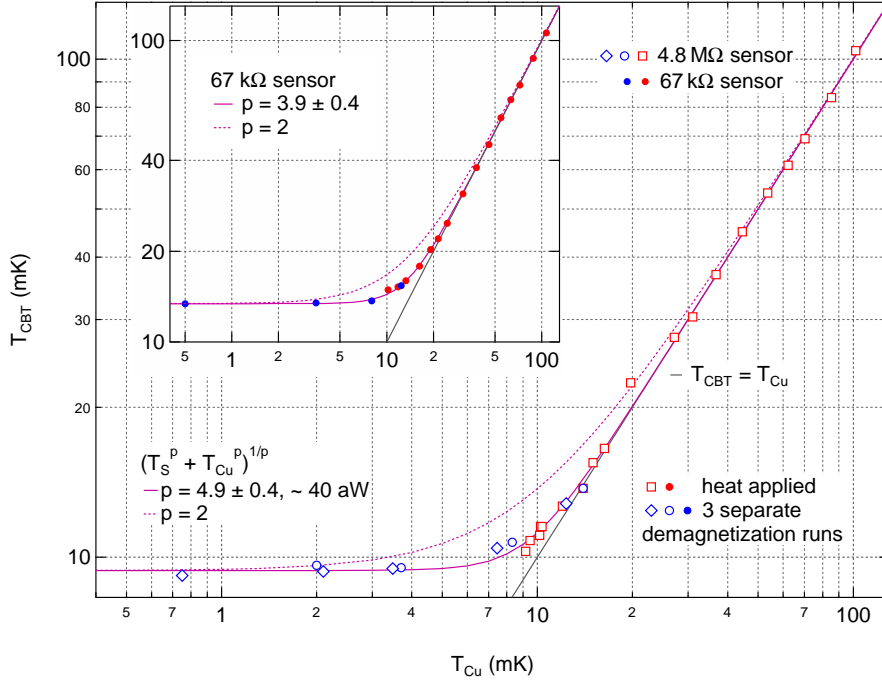


**Figure 3.3:** CBT electron temperature  $T_{CBT}$  versus NR temperature  $T_{Cu}$  for 4.8 M $\Omega$  (open markers) and 67 k $\Omega$  sensors (filled markers, same axes on inset as main figure). Below 10 mK, the data is obtained in 3 demagnetization sweeps (blue markers) with  $B = 9$  T, 5 T, 2 T, 1 T and 0.4 T in a typical run, ramped at 1 T/h above 1 T and 0.5 T/h below. Error bars are about the size of the markers. Purple curves are  $T_{CBT}$  saturation curves (see text).

When analogously examining the low- $R$  sensors, on the other hand, we find  $p = 3.9 \pm 0.4$  and  $T_S = 13.4$  mK for the 67 k $\Omega$  sensor (see inset Fig. 3.3), and even  $p = 2.7 \pm 0.2$  and  $T_S = 6.9 \pm 0.1$  mK for a 134 k $\Omega$  sensor (not shown) mounted on a conventional dilution refrigerator (base- $T \sim 5$  mK) with improved filtering and chip carrier. Note that  $T_S$  is the extrapolated  $T_{Cu} = 0$  saturation- $T$ . The lowest  $T$  measured here was  $7.5 \pm 0.2$  mK. These power-laws far below  $p = 5$  indicate that EP cooling is no longer dominant but, rather, a more efficient mechanism  $p < 5$  takes over at the lowest- $T$  in the low- $R$  sensors.

### 3.5 Summary

In summary, we have demonstrated operation of the NRs down to 0.3 mK while the CBTs cool as low as 7.5 mK. Though the high- $R$  sensor is obviously cooled by EP coupling, the low- $R$  sensors, interestingly, appear to be entering a different cooling regime. However, the low- $R$  sensors have slightly higher  $T_{CBT}$  given the same environment, consistent with stronger coupling to the environment. The lowest CBT temperatures are limited by the parasitic heat leak, which is drained by the cooling channels available.

To further improve the sensor performance, the cooling-fin volume can be increased or the heat leak can be reduced, potentially using improvements in microwave shielding and filtering, e.g. using on-chip capacitors, metal planes or alternative array designs. Such efforts will strongly enhance thermalization if a more efficient cooling mechanism is indeed present, since otherwise, in the EP regime, reducing  $\dot{Q}_0$  by 5 orders of magnitude will only reduce  $T_{CBT}$  by a factor of ten.

An alternative avenue based on quantum dot CBTs, e.g. in GaAs, might also be rewarding, taking advantage of a much larger  $E_C$  and level spacing  $\Delta$ . The resulting reduced sensitivity to the environment might allow a single dot to be used, rather than an array, cooling the reservoirs directly via the WF term, rather than through a long series of junctions.

### Acknowledgments

We would like to thank R. Blauwgeers, G. Frossati, R. Haley, G. Pickett, V. Shvarts, P. Skyba and A. de Waard for very useful discussions. This work was supported by the Swiss Nanoscience Institute (SNI), NCCR QSIT, Swiss NSF, ERC starting grant, and EU-FP7 SOLID and MICROKELVIN.

## 4 GaAs Quantum Dot Thermometry Using Direct Transport and Charge Sensing

L. Casparis, D. Maradan, T.-M. Liu, D. E. F. Biesinger,

C. P. Scheller, D. M. Zumbühl

*Department of Physics, University of Basel, CH-4056 Basel, Switzerland*

J. Zimmerman, A. C. Gossard

*Materials Department, University of California, Santa Barbara, California, USA*

### Abstract

We present measurements of the electron temperature using gate defined quantum dots formed in a GaAs 2D electron gas in both direct transport and charge sensing mode. Decent agreement with the refrigerator temperature was observed over a broad range of temperatures down to 10 mK. Upon cooling nuclear demagnetization stages integrated into the sample wires below 1 mK, the device electron temperature saturates, remaining close to 10 mK. The extreme sensitivity of the thermometer to its environment as well as electronic noise complicates temperature measurements but could potentially provide further insight into the device characteristics. We discuss thermal coupling mechanisms, address possible reasons for the temperature saturation and delineate the prospects of further reducing the device electron temperature.

This chapter was published in *JLTP* Vol. 175, **5**, 784 (2014).

## 4.1 Introduction

Two-dimensional electron gases (2DEGs) are a versatile, widely-used experimental platform in low temperature solid state physics because of their nearly ideal two-dimensional nature and the possibility to confine electrons to almost arbitrary shapes using gate voltages. Groundbreaking experiments have been realized in these systems, including artificial atoms [27, 71, 72], the integer and fractional quantum Hall effect [15, 16] and spin qubits [33, 59]. In many experiments, the temperature of the 2DEG is much higher than the temperature  $T_{MC}$  of the dilution refrigerator mixing chamber due to various reasons, including poor thermal coupling and insufficient filtering. However, a wide range of phenomena contain small energy scales and are only accessible at very low temperatures. These include novel nuclear spin quantum phases in 2D [36, 37] and in interacting 1D conductors [73, 74] and multiple impurity [75] or multiple channel [76, 77] Kondo physics. Further, studies of fragile fractional quantum Hall states, including candidates for non-Abelian physics such as the  $\nu = 5/2$  state [78], would benefit from low temperatures, possibly opening the doors for topological quantum computation [60].

To our knowledge, the lowest reliable temperature reported in a 2DEG is 4 mK [62, 63] in a fractional quantum Hall experiment, with sintered silver heat exchangers attached to the sample wires in a  $^3\text{He}$  cell. In Ref. [63], a  $\text{PrNi}_5$  demagnetization stage at 0.5 mK was used to cool the liquid  $^3\text{He}$ , well below the 4 mK of the 2DEG sample. For quantum Hall samples loaded into a chip holder in vacuum, slightly higher temperatures 9...13 mK were reported [79–81]. Interestingly, in Ref. [80] (supplementary), the refrigerator base temperature was below 6 mK and the temperature measured with a Coulomb blockaded quantum dot was  $16 \pm 3$  mK. The lowest GaAs quantum dot temperature measurement reported is 12 mK [82, 83], as far as we know.

We note that apart from noise measurements [79], electron temperature measurements in the (fractional) quantum Hall regime are of rather qualitative nature, usually lacking

a well-known temperature dependent effect to extract temperature from. Instead, some temperature dependent feature, typically a longitudinal resistance peak [62, 63, 80], is used, assuming a specific temperature dependence (e.g. linear) – resulting in estimates of temperature, rather than absolute temperature values. A quantum dot thermometer, on the other hand, is in principle a primary thermometer capable of reading absolute temperatures [71]. However, compared to quantum Hall samples, a quantum dot device operates at significantly larger resistance (typically  $\gtrsim 1 \text{ M}\Omega$ ). Thus, essentially the entire voltage drops over the dot, presumably making it more susceptible to electronic noise.

For any device electron thermometer, it is very instructive to compare the electron temperature with a suitable calibrated refrigerator thermometer over a broad temperature range. Ideally, both thermometers should agree very well, demonstrating effective operation of the device thermometer – in a much more convincing way than agreement at any single, isolated temperature. In addition, at the lowest refrigerator temperatures, often a saturation of the device temperature becomes apparent, either due to improper thermometer operation or insufficient device thermalization (or both). The functional form of the deviation of the device temperature from the refrigerator temperature in principle contains important information about the device cooling mechanism [84], if the thermometry is accurate enough and functioning properly. Previous reports have shown quantum dot thermometers to agree well with the refrigerator thermometer over a broad range of rather high temperatures  $T \gtrsim 100 \text{ mK}$  [85–87], with the best reaching down to about 50 mK [43, 83, 88–90] – but not to lower temperatures.

These examples indicate that cooling of a 2DEG embedded in a semiconductor such as e.g. GaAs is a difficult task. The main reason is the weakening of the electron-phonon interaction in the 2DEG  $\propto T^5$  [63, 91, 92] at low temperatures. Therefore, at very low temperature, the system benefits from cooling through the conduction electrons (Wiedemann-Franz mechanism,  $\propto T^2$  [39, 93]), where heat transfer is mediated through the electrical contact to the sample. For typical semiconductor devices with compar-

atively large contact resistances, this comparably weak coupling makes the sample vulnerable to heat leaks, e.g. high frequency radiation or dissipative heating. Additionally, the weakening of the electron-phonon interaction significantly complicates the thermal coupling of the insulated sample wires to the coldest part of the refrigerator.

Recently, we have proposed a way to overcome these limitations by integrating a copper nuclear refrigerator into each of the electrical sample wires connected to an electronic transport sample, providing efficient thermal contact to a bath at low mK or microkelvin temperature [48]. For efficient precooling of the nuclear refrigerators as well as for regular dilution refrigerator operation, every sample wire is connected to a sintered silver heat exchanger located in the plastic mixing chamber (facilitating superfluid leak-tight feedthroughs) of the dilution refrigerator with a base temperature of 9 mK. Further, to minimize the effect of high-frequency radiation, all electrical lines are filtered extensively using thermocoax cables, cryogenic Ag-epoxy microwave filters [69] and double-stage RC filters of bandwidth 30 kHz. The measurement setup is described in detail in reference [84]. In semiconductor samples such as GaAs 2DEGs, the ohmic contacts will probably present the largest electrical and thermal impedance in this cooling scheme.

## 4.2 Quantum Dot Thermometry

Gate defined GaAs quantum dots in deep Coulomb blockade are used as a thermometer directly probing the electron temperature  $T$  in the surrounding 2DEG by measuring the thermal smearing of the Fermi edge [71]. As shown in Fig. 4.1(a), the quantum dot is coupled to two electron reservoirs via left and right tunnel barriers with tunnel rates  $\Gamma_L$  and  $\Gamma_R$ . In the symmetric case  $\Gamma_L = \Gamma_R = \Gamma$ , the direct current through the quantum dot is approximated by  $I_{DC} = e\Gamma/2$  assuming sequential tunneling, with  $e$  the electron charge. In the temperature broadened Coulomb blockade regime ( $h\Gamma \ll k_B T$ , with Boltzmann constant  $k_B$  and Planck constant  $h$ ), the narrow dot level with broadening  $\sim \Gamma$  acts as a variable energy spectrometer which can resolve and directly map the

Fermi-Dirac (FD) distribution in the current through the dot. The energy of the spectrometer can be tuned by capacitively shifting the dot energy level with a gate, e.g. the plunger gate at voltage  $V_P$ . With a sufficiently large DC source-drain bias  $V_{SD} \gg k_B T/e$ , the chemical potential of source and drain reservoirs can be individually resolved, separately giving the distribution functions of each reservoir when sweeping the plunger gate voltage  $V_P$  through both source and drain chemical potentials.

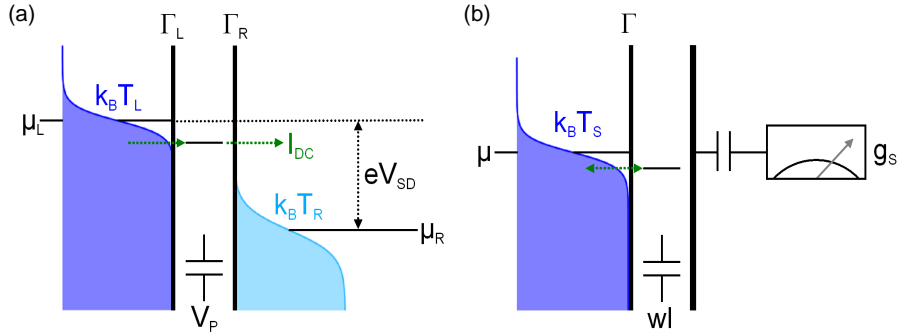


**Figure 4.1:** (a) Schematic for a temperature measurement using a single quantum dot. Low tunnel rates to the left and right reservoir,  $\Gamma_L$  and  $\Gamma_R$  respectively, result in an energetically sharp quantum dot level which can be tuned with the plunger gate  $V_P$ . By sweeping the dot level through the source-drain window  $eV_{SD}$ , given by the difference in chemical potentials  $\mu_L - \mu_R$ , the temperature of each reservoir can be extracted individually; the thermally smeared Fermi-Dirac distributions ( $\propto k_B T$ , here  $T_R > T_L$ ) are mapped with the measured current  $I_{DC}$ . (b) Working principle for the charge sensing measurement: the dot level can be swept through the Fermi level at chemical potential  $\mu$  using the top gate voltage  $wl$ . The average occupation probability, which again reflects the Fermi-Dirac distribution (i.e. temperature  $T_S$ ) in the double dot reservoir, is probed by the conductance  $g_s$  through a charge sensing quantum dot capacitively coupled to the dot. For details see text.

To stay in the single level transport regime, the bias  $V_{SD}$  has to be small compared to the excited state energy  $\Delta$ . To obtain the temperature from each distribution function, the gate lever arm  $\alpha$  is required for the conversion from gate voltage to energy. The separation  $\Delta V_P$  in gate voltage between the inflection points of the two FD distributions can be taken from the plunger gate sweep  $I_{DC}(V_P)$  at a fixed, known bias  $V_{SD}$ . This measurement gives the lever arm  $\alpha = eV_{SD}/\Delta V_P$  without additional measurements and delivers the temperatures  $T_L$  and  $T_R$  of the left and right reservoir, respectively, from a single  $I_{DC}(V_P)$  sweep. This allows a temperature measurement without calibration by



another thermometer, thus constituting a primary thermometer. As an alternative, the differential conductance through the dot can be measured using a small AC voltage, resulting in the derivative of the FD function [71].

We note that here, the device is operated in a highly non-linear regime where the dot current  $I_{DC}$  depends only on the tunneling rate  $\Gamma$  but is – to lowest order – independent of the applied bias  $k_B T \ll V_{SD} \ll \Delta$  once the dot level is well within the transport window spanned by source and drain chemical potentials. However, the electrons traversing the dot are injected at a high energy  $V_{SD} \gg k_B T$  into the reservoir with the lower chemical potential. These hot electrons will relax their energy and thereby cause heating in the 2DEG reservoir. The currents and biases used here are rather small, typically giving heating powers  $\sim I_{DC} V_{SD}$  below 1 fW. Nevertheless, this heat will need to be removed, e.g. through the ohmic contacts or the phonon degree of freedom. We experimentally choose the bias  $V_{SD}$  small enough to avoid measurable heating.

For ultra-low temperatures, one critical aspect of the quantum dot thermometer is the requirement to have a dot level much sharper than the FD distribution to be probed and resolved. The broadening of the dot level is given by lifetime broadening: the finite time an electron spends on the dot, defined by its escape rate  $\sim \Gamma$ , introduces an uncertainty on its energy through the time-energy Heisenberg uncertainty principle. In gate defined dots, the tunneling rate  $\Gamma$  can be tuned widely over many orders of magnitude with gate voltages, affording broad flexibility. While  $\Gamma$  can easily be made sufficiently small to satisfy  $h\Gamma \ll k_B T$  even at the lowest temperatures, reduced  $\Gamma$  also suppresses the dot current  $I_{DC} \sim e\Gamma/2$ . Taking  $2h\Gamma = k_B T$ , an upper bound on the dot current of  $I \sim 1 \text{ pA} \cdot \vartheta$  results, where  $\vartheta$  is the temperature in mK. Thus, to be clearly in the temperature broadened regime, currents far below these upper bounds are required, setting a practical limit of order of 10 mK as the lowest temperature that can be measured with the current setup.

An integrated charge sensor directly adjacent to the quantum dot [94, 95] makes it possible to overcome this limitation: a measurement of the average dot charge occu-

pation while sweeping the dot level through a charge transition [96] reflects the FD distribution under similar conditions as described before. However, the dot-reservoir tunneling rate  $\Gamma$  can now be made essentially arbitrarily small, ensuring  $h\Gamma \ll k_B T$  even for temperatures well below 1 mK. This is possible because the size of the charge sensor signal is nearly independent of  $\Gamma$  and the charge sensor remains operational for arbitrarily small  $\Gamma$ . The distribution function is conveniently measured when the dot tunneling is fast compared to the data acquisition rate, avoiding complications due to real time detection of single electron tunneling. The current through the charge sensor still gives rise to phonon or photon emission [97] and generally causes heating, analogous to a current flowing directly through the dot as discussed above. However, the sensor and its reservoirs can be electrically isolated and spatially separated somewhat from the dot, reducing heat leaks and coupling strength [98] and improving the situation compared to a direct current through the quantum dot. Nevertheless, the sensor biasing will need to be experimentally chosen to minimize such heating effects.

Similar thermometry can also be performed in a double quantum dot configuration, where charge transitions involving a reservoir can be used to measure the FD distribution and the corresponding temperature, see Fig. 4.1(b). The relevant double dot lever arm can be extracted again from finite bias measurements [99] or can be calibrated at elevated temperatures where it is safe to assume  $T_{MC} = T_{L,R}$  with the temperature of the left and right reservoir  $T_{L,R}$ , respectively. It is worth noting that in a double dot, the thermal smearing of the reservoirs can be essentially eliminated when studying internal transitions such as inter-dot tunneling, allowing measurements with a resolution much better than the reservoir temperature [99]. Nevertheless, internal double dot transitions can also be used for reservoir thermometry depending on the dot configuration [96]. Similarly, in optically active semiconductor quantum dots, the reservoir temperature can be irrelevant, and the optical line width is limited by the lifetime and/or other noise sources such as semiconductor charge instabilities or nuclear spin noise [100].

Interestingly, the energy levels of the double dot can easily be configured (e.g. sufficiently far away from the triple points or bias triangles) so that no net current can flow through the double dot even at some finite bias (here always assuming sequential tunneling only), avoiding dissipative heating originating from the double dot altogether. Despite the absence of current flow, the system can still easily be probed with a charge sensor, and the reservoir temperature can be extracted as described above. A similar situation can also be exploited in a single dot with one barrier tuned to be very opaque [101]. The biasing of the charge sensor nevertheless still dissipates energy, as already described.

### 4.3 Thermometry with Direct Transport

The quantum dots were fabricated with standard UV and ebeam lithography and evaporation of Ti/Au depletion gates. The single quantum dot (SQD) layout, see inset of Fig. 4.2(b), was adapted from Ref. [102], giving access to the few electron regime in transport measurements. The 2DEG is formed at a single AlGaAs/GaAs interface, located 110 nm below the surface, with charge carrier density  $n = 2.8 \cdot 10^{11} \text{ cm}^{-2}$  and mobility  $\mu = 280'000 \text{ cm}^2/(\text{Vs})$ . This wafer was chosen because of excellent charge stability. The devices were cooled down without positive voltage bias on the gates. The ohmic contacts are non-magnetic, made from AuGe/Pt, and optimized for minimal contact resistances, typically  $\lesssim 100 \Omega$ . The direct current  $I_{DC}$  through the dot was measured with a 3 Hz low-pass filter.

We now show how the reservoir temperatures  $T_L$  and  $T_R$  can be extracted from a measurement of the current  $I_{DC}$  through the dot at finite applied bias  $V_{SD}$  as a function of the plunger gate voltage  $V_P$ , as shown in Fig. 4.2(a). The plunger gate  $V_P$  allows us to shift the energy of the dot level through both source and drain chemical potentials without significantly changing the reservoir tunneling rates for a small change of  $V_P$ : more negative  $V_P$  capacitively shifts the dot level to higher energy. A finite current flows through the dot when the dot energy level is located within the transport window,

see Fig. 4.1(a). Otherwise, no current can flow, either due to a lack of filled electron states when the dot energy is above the higher chemical potential reservoir, or due to a lack of empty states the dot electron can tunnel into when the dot energy is below the lower chemical potential reservoir. The transitions between zero and finite current  $I_{DC}$  each reflect the distribution function of the respective reservoir, and can be fit by a FD function of the form

$$I_{FD}(V_P) = I_1 \left[ \exp \left( \frac{\alpha(V_P - V_{P0})}{k_B T_{L,R}} \right) + 1 \right]^{-1} + I_0, \quad (4.1)$$

with step height  $I_1$ , offset current  $I_0$  and plunger gate offset  $V_{P0}$ . For a given step height  $I_1$  and lever arm  $\alpha$ , the temperature is essentially given by the slope of the transition, where lower temperature corresponds to a steeper, sharper curve. A rising (falling) step is obtained by the choice of the relative sign of  $I_0$  and  $I_1$ . We note that this fit function will only apply in a rather narrow window of energy (i.e. plunger gate voltage) around the transition, since other effects not captured by the FD function alone can also play a role, such as local density of states variations due to the finite size lead reservoirs. The FD function gives high quality fits to the data within the measurement noise, see Fig. 4.2(a), and delivers separate temperatures  $T_{L,R}$  for the left and right reservoirs, respectively. The right reservoir was connected to the current preamplifier and gives slightly higher temperatures  $T_R > T_L$ , see Fig. 4.2(a). Swapping the current preamplifier to the other reservoir inverts the situation. Upon increasing  $T_{MC}$ , we have observed better agreement with  $T_L$  than with  $T_R$ , thus we will focus on  $T_L$ . The weak dependence of dot current on  $V_P$  in the high current state can arise e.g. due to variations in the local density of states in the leads, but is not part of the transition region fit by the FD function. The DC bias voltage was reduced until no effects on the extracted temperatures were observed, typically  $V_{SD} < 100 \mu\text{V}$  at the lowest temperatures – still allowing to clearly separate the two flanks.

Despite significant noise on the  $I_{DC}$  data, the error-bars on the temperatures extracted from the individual FD fits are rather small  $\lesssim 10\%$ , see Fig. 4.2(a), plus  $\lesssim 10\%$

error from uncertainty of the lever arm  $\alpha$ . A further uncertainty (typically about  $\lesssim 20\%$ ) becomes apparent when the fits are performed over a large number (of order 10) of repeated current traces under nominally identical conditions, see Fig. 4.2(b). This uncertainty is due to charge instabilities and resulting random telegraph noise – occasionally directly identifiable in the data as a discrete switch – as well as slow drifts in the 2DEG material and quantum dots, or external influences. Semiconductor charge noise is known for a long time and has been studied extensively, see e.g. Refs. [100, 103, 104] and references therein. We note that the sensitivity to such disturbances becomes more pronounced at lower temperature, already requiring an energy jitter of much less than  $\sim 1 \mu\text{eV}$  at 10 mK – a quite remarkable charge stability [100]. The severity of such charge noise depends sensitively on the detailed dot gate voltage configuration as well as the wafer material and fabrication procedure, and can become negligible at elevated temperatures due to increased thermal broadening. Current traces with obviously apparent switching events are not included in the ensemble of traces used to extract temperature. Nevertheless, charge switching is not always directly identifiable, and the fluctuating temperatures extracted from the FD fits upon repeating the measurement are predominantly due to charge noise. A switch occurring during the scan at the transition is the only obvious source we are aware of that could lead to both a narrowing or a broadening of the FD distribution, resulting in artificially fluctuating temperatures extracted from the FD fits, as seen in the experiment.

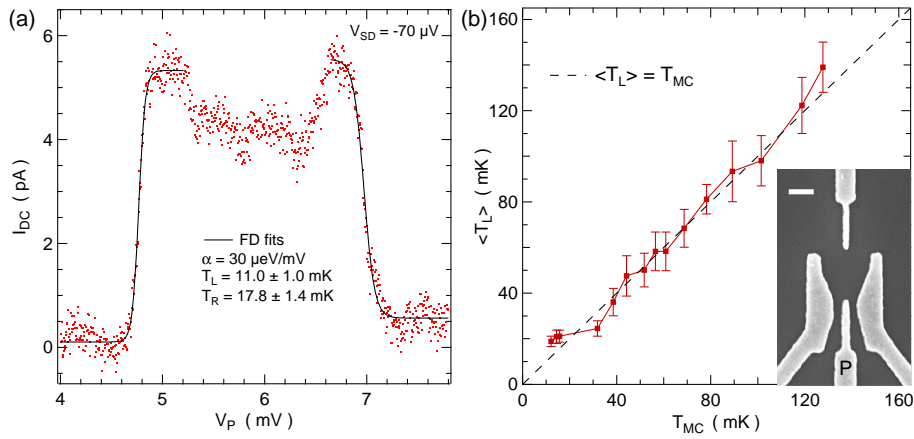


**Figure 4.2:** (a) DC current  $I_{DC}$  through the single quantum dot as a function of plunger gate voltage  $V_P$  at refrigerator temperature  $T_{MC} = 9$  mK, showing a high current region (dot level between source and drain chemical potential) and a low current region (dot level outside source-drain window). These regions are separated by the Fermi-Dirac distributions in each reservoir, separately giving  $T_L$  and  $T_R$  from Fermi-Dirac fits (solid curves). The error bars shown here are the uncertainties from the FD fits only. An additional uncertainty of  $\lesssim 10\%$  arises from the error on the lever arm. The right reservoir is connected to the current preamplifier and slightly warmer than the left reservoir. (b) Average temperature  $\langle T_L \rangle$  obtained over several repeated  $T_L$  measurements, as a function of refrigerator temperature  $T_{MC}$ . The dot configuration was not changed during this temperature sweep. The error bars shown are the statistical errors from repetition of the  $T_L$  measurement. An additional uncertainty of  $\lesssim 10\%$  on  $\langle T_L \rangle$  needs to be added to the error bars shown, arising from the uncertainty of the lever arm. Inset: SEM picture of a device similar to the one measured (P: plunger gate, scale bar: 200 nm).

Due to the sizable charge noise, we cannot use an individual temperature measurement as in Fig. 4.2(a), but rather have to gather statistics in order to obtain a more reliable measure of temperature. In Figure 4.2(b), we extract the average temperature of the left reservoir  $\langle T_L \rangle$  measured with the quantum dot at fixed configuration for several refrigerator mixing chamber temperatures  $T_{MC}$ , measured with a Cerium-Magnesium-Nitrate (CMN) thermometer. The CMN thermometer was calibrated using a standard fixed point device with 6 superconducting transitions between 1.2 K and 96 mK, giving excellent agreement between fixed point device and CMN. A calibrated  $\text{RuO}_2$  resistor (also in very good agreement with the fixed points) was used to extend the CMN calibration range to lower temperatures, giving excellent agreement with the CMN to below 20 mK. Almost identical CMN temperatures are obtained in the range from

10 mK to 200 mK, regardless of whether a Curie law or a Curie-Weiss law is used to calibrate the CMN thermometer [39].

The standard deviation resulting from the repeated current traces is used to give the error bars on  $\langle T_L \rangle$  in Fig. 4.2(b). The lever arm uncertainty  $\lesssim 10\%$  is in addition to the error bars shown. As seen in Fig. 4.2(b), we find decent agreement between  $\langle T_L \rangle$  and  $T_{MC}$  within the error bars over the temperature range from  $\sim 20$  mK to  $\sim 130$  mK. At the lowest temperatures, however,  $\langle T_L \rangle$  appears to saturate at  $\sim 20$  mK for the particular gate configuration used for this temperature sweep. When the measurement is further optimized and the tunnel rates are decreased a bit more (trading off current signal amplitude), the lowest temperature we extract in direct current through the dot is  $\langle T_L \rangle = 11 \pm 3$  mK (including all errors) averaged over several traces similar to the data shown in Fig. 4.2(a). This is within the error bars of the base temperature  $T_{MC} = 9$  mK. Given agreement between  $\langle T_L \rangle$  and  $T_{MC}$  over a wide temperature range, we can be confident that the sample is well thermalized and the dot thermometer is properly working, reading a reliable temperature despite charge noise.

## 4.4 Thermometry with Charge Sensing

We now turn to thermometry with a charge sensor adjacent to a double quantum dot device. The design of the device was adapted from Ref. [105], see inset of Fig. 4.3(a), employing quantum dots as very sensitive charge detectors, directly adjacent on either side of the double dot. Here, we focus on data from one of the sensors since the other sensor gave very similar results. A GaAs 2DEG material very similar to the wafer used for the single dots was used, again experimentally tested to exhibit excellent charge stability. The differential conductance  $g_s = dI/dV$  of the charge sensing quantum dot was measured with standard analog lock-in technique with an AC bias voltage  $\leq 2 \mu\text{V}$ . The sensor bias voltage was carefully experimentally restricted to avoid excess heating. The voltage and current noise of the measurement setup was carefully monitored and minimized, with optimal rms values of  $0.5 \mu\text{V}$  and  $50$  fA, respectively.

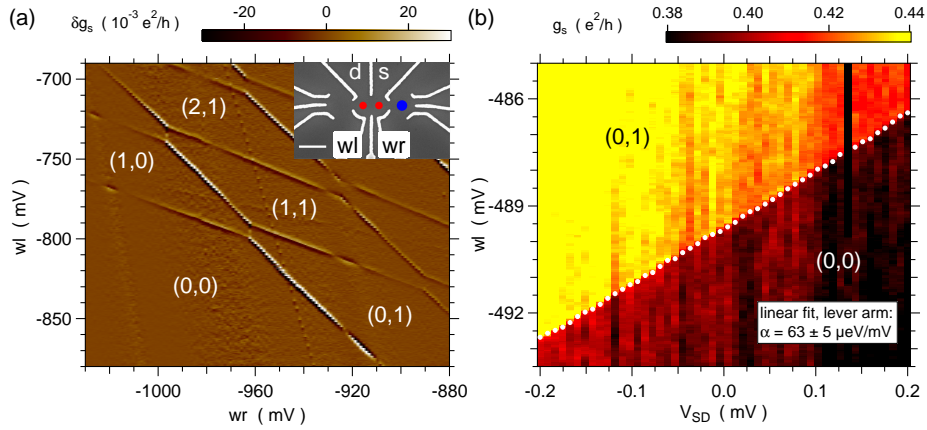


**Figure 4.3:** (a) Change in differential conductance  $\delta g_s$  of the sensor on the right side measured as a function of the voltage on the left wall  $w_l$  and right wall  $w_r$  of the double dot. The average of each vertical trace was subtracted to improve visibility. The charge stability diagram shows the honeycomb structure typical of a double dot. The absolute electron occupation  $(n,m)$  is labeled, indicating the charge state in the left and right dot, respectively. Inset: SEM picture of a device similar to the one measured ( $d/s$ : drain/source, scale bar: 400 nm, red dots: DQD, blue dot: charge sensing quantum dot). The colored dots refer to the estimated positions but not the actual sizes of the quantum dots. (b) Sensor differential conductance  $g_s$  as a function of  $w_l$  and  $V_{SD}$  around the  $(0,0)$  to  $(0,1)$  transition, allowing extraction of the lever arm  $\alpha$ , see text.

The sensitivity of the charge sensor can be defined as  $2|g_1 - g_2|/(g_1 + g_2) = |\Delta g|/g_{avg}$  with the conductance values  $g_1$  and  $g_2$  corresponding to the charge states before and after the transition and  $g_{avg} = (g_1 + g_2)/2$ . The charge sensor was operated in the lifetime broadened regime, tuned on a steep slope of a Coulomb blockade peak, giving excellent sensitivities of up to 100%. This is clearly superior to typical quantum point contact charge sensors, as previously reported [105]. Even better sensitivities could be achieved when tuning the sensor dot into the temperature broadened regime, where much narrower, sharp peaks result. However, staying on such a sharp peak becomes experimentally difficult due to parasitic capacitive coupling between double dot gates and the sensor dot. Once the sensor is shifted to a region where the slope is very small (e.g. a Coulomb blockade valley with nearly vanishing conductance), the charge sensitivity is lost. Already in the lifetime broadened sensor regime used here, changes on the double dot gate voltages needed to be carefully compensated on the plunger gate of the sensor dot in order to maintain charge sensitivity.



The double dot charge stability diagram, as measured with the charge sensor, is shown in Fig. 4.3(a) as a function of gate voltage on the left wall  $w_l$  and right wall  $w_r$  of the double dot, as labeled in the inset. The typical honeycomb pattern as expected for a double dot [99] is observed. Each dot can be emptied of all electrons (bottom left), as evidenced by the absence of further charge transition lines in the diagram at more negative gate voltages. This allows us to label the double dot charge state  $(n,m)$ , indicating the absolute electron occupation in the left and right dot, respectively. A couple of additional weak charge transitions are also appearing with slopes deviating from those occurring in the honeycomb of the double dot, presumably due to some nearby charge traps in the semiconductor. These are also related to the charge noise as seen in the temperature measurements.

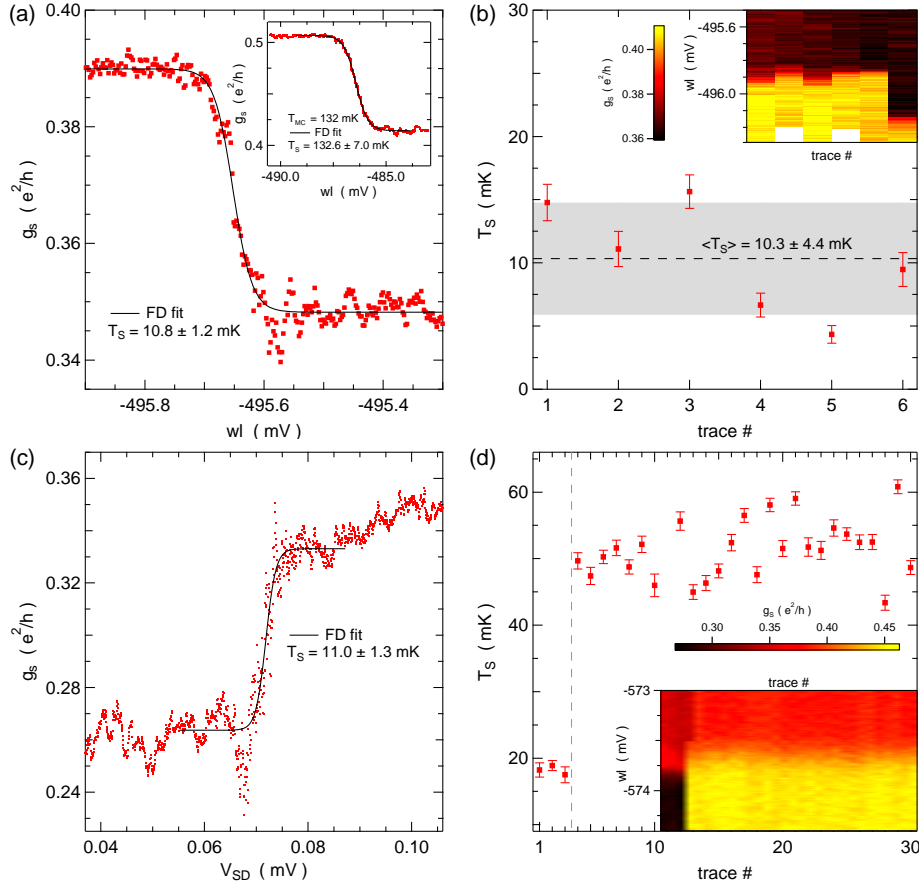


**Figure 4.4:** (a) Sensor differential conductance  $g_s$  (sensor dot on the right side) as a function of gate voltage  $w_l$  at  $T_{MC} = 9$  mK, showing the transition from the (0,0) to (0,1) charge state. The reservoir temperature  $T_S$  is extracted from a FD fit (black curve) to sensor data, as indicated. Inset: Similar measurement with corresponding fit at  $T_{MC} = 132$  mK showing  $132.6 \pm 7.0$  mK. (b) Series of repeated  $T_S$  measurements in the same dot configuration with an average temperature  $\langle T_S \rangle = 10.3 \pm 4.4$  mK (dashed line: average; gray shaded area: standard deviation). Inset: Corresponding sensor conductance  $g_s$  as a function of gate voltage  $V_{wl}$  versus trace number. (c) Sensor conductance  $g_s$  of the right charge sensor as a function of  $V_{SD}$  at the transition from (0,0) to (0,1), with FD fit (black curve) and extracted temperature (see text) as labeled. (d) Reservoir temperature  $T_S$  extracted with the sensor from several repeated  $w_l$  sweeps (see inset) versus trace number, showing an abrupt change of the electronic dot configuration after three sweeps, which increases the temperature reading from 18 mK to 52 mK. The systematic lever arm error of  $\lesssim 8\%$  is to be added to all error bars here in (a) through (d).

The reservoir temperature can again be extracted, here from the charge sensor signal with analogous FD fits to any of the charge transitions in the honeycomb involving one of the reservoirs. The data are fitted using Eq. (4.1) by replacing currents  $I$  with sensor conductances  $g_s$  as well as  $V_P$  and  $V_{P_0}$  with  $w_l$  and  $w_{l0}$ , respectively. As before,

the corresponding lever arm is required for the conversion from gate voltage to energy, and is extracted from measurements at high enough temperatures where double dot reservoir temperature  $T_S$  measured with the sensor is equal to  $T_{MC}$ . Bias triangles were not accessible in the regime the double dot was operated here due to tunnel rate asymmetries. We note that the inter-dot tunnel rate was tuned to be very small for the temperature measurements, with the double dot operated in a gate voltage configuration different from the one shown in Fig. 4.3(a).

Alternatively, the same charge transition can be followed for various double dot source-drain voltages  $V_{SD}$  applied to the reservoir involved in the transition, as shown in Fig. 4.3(b). Due to a finite capacitance of this reservoir to the dot, this gives an upper bound for the lever arm and the extracted temperature. However, the lever arm extracted at high temperature turns out to be the same as the upper bound (within the error bars of 10%), thus indicating that the reservoir-dot capacitance is small compared to the total dot capacitance for the configurations used in our device – at least at the very low tunnel rates utilized here. Hence, the slope of the charge transition line in the  $wl-V_{SD}$  plot gives the inverse of the lever arm. The lever arm error of  $\lesssim 10\%$  needs to be added to all temperatures appearing in this section (unless noted otherwise) as a systematic rather than fluctuating error, i.e. affecting all temperatures in the same way. All temperature measurements shown here were carried out at the transition from (0,0) to (0,1), although similar results were obtained for other transitions.

Figure 4.4(a) shows a charge sensor measurement through the (0,0)-(0,1) transition and a FD fit at  $T_{MC} = 9$  mK, resulting in  $T_S = 10.8 \pm 1.2$  mK. While the sensor measurements give very good agreement with the FD fits at elevated temperatures (see Fig. 4.4(a) inset, giving  $T_S = 132.6 \pm 7.0$  mK at  $T_{MC} = 132$  mK) over a broad temperature range, the charge sensor temperature measurement again becomes more difficult at the lowest temperatures. The inset of Fig. 4.4(b) shows the sensor signal for the same charge transition repeated a few times under identical conditions. Both the position and width of the transition is seen to fluctuate as a function of time, resulting

in fluctuating temperatures  $T_S$  extracted with the FD fit, see Fig. 4.4(b), similar as described for temperature measurements via current through the dot. The error bars shown here (and also in Fig. 4.4(d)) are from the FD fit only. In addition, the configuration of the sensor can also affect the extracted temperatures, typically resulting in elevated temperatures for stronger sensor-double dot coupling. Thus, at lower temperature, smaller sensor step heights are required, making fitting more difficult. As before, curves displaying obvious switching events are not considered for determining temperature.

We can also use the double dot source-drain voltage  $V_{SD}$  instead of gate voltage to drive the charge transition and directly obtain a temperature value without needing a lever arm, since the reservoir-dot capacitance is small here, as previously discussed. In this way, we obtain an upper bound on the reservoir temperature which here is close (within 10%) to the actual temperature. Such a  $V_{SD}$  charge transition measurement is illustrated in Fig. 4.4(c), again for the (0,0)-(0,1) transition, and gives a very similar temperature as obtained from the gate sweep. The undershoot before and the overshoot after the rising edge has been observed in several measurement curves at the lowest temperatures, both by sweeping  $V_{SD}$  or a gate, though it is not seen in some other traces, e.g. Fig. 4.4(a). These features are only seen for certain gate voltage configurations, and their origin is not currently understood.

The extreme sensitivity of the charge transition to the electrostatic environment is demonstrated in Fig. 4.4(d). While scanning the same transition 30 times, an abrupt change in the charge configuration during the fourth scan has altered the charge sensor conductance considerably, even inverting the sign of the sensor response to the dot charge transition. This switching event caused the apparent FD fit temperature to change from 18 mK to 52 mK. While the sensor conductance and double dot configuration can be strongly altered by a local charge rearrangement, the temperature of the large reservoirs was most certainly not affected by this single switching event. Thus, the lower temperature 18 mK reflects the reservoir temperature both before and

after the switching event, while the higher temperature is artificially elevated due to improper dot/sensor configuration. Scanning charge transitions different from (0,0) to (0,1) revealed similar temperatures but also suffered from the same problems with charge instabilities.

## 4.5 Discussion

After considerable experimental efforts due to the pronounced sensitivity to electronic noise and device charge instabilities, we approach mixing chamber base temperature with both methods, direct transport and charge sensing. By using the nuclear refrigerator ( $T_{NR} < 1$  mK [84]), no further reduction of the electron temperature was observed, in contrast to measurements with other thermometers mounted in the same refrigerator in subsequent cool downs, see chapter 5. In the direct transport measurements, we might suspect lifetime broadening of the quantum dot level as a limiting factor. But the temperatures obtained with the charge sensor are not evidently lower than the temperatures measured in direct transport, despite much lower dot tunneling rates.

In direct transport, dissipative heating from the voltage drop over the dot will eventually become significant at sufficiently low  $T$ . Estimates of the electron temperature  $T$  assuming dominant Wiedemann-Franz cooling, an ohmic contact resistance of  $100\ \Omega$ ,  $V_{SD} = 100\ \mu\text{V}$  and a current of  $8\ \text{pA}$  ( $\Gamma/2 = 50\ \text{MHz}$ ) indicate that the temperature is only increased by  $\Delta T = 0.3\ \text{mK}$  above the bath temperature at  $T_{MC} = 10\ \text{mK}$ . At a much lower temperature  $T_{NR} = 1\ \text{mK}$ , however, the electron temperature is estimated to rise to  $T = 2.8\ \text{mK}$  due to poor thermal contact. This strong increase is due to the ohmic contact resistance, which could potentially be further reduced with improved fabrication. In addition, the voltage bias  $V_{SD}$  can also still be made much smaller, since a temperature of  $T_{NR} = 1\ \text{mK}$  corresponds to a broadening of the FD distribution of only  $\sim 0.1\ \mu\text{V}$ , thus still leaving room to fulfill  $eV_{SD} \gg k_B T$ .

Our experiments indicate that the electronic noise and external disturbances in the measurements setup play a very important role: excess voltage noise clearly increases

the temperatures extracted. Filtering and shielding can be further improved, though already in the present experiment, a significant amount of work was invested [84]. We obtain noise levels as low as several hundred nanovolts across the dot measured at room temperature, but significantly less at the cold device due to filtering. The electron temperature here becomes independent of the noise power at the lowest noise levels, indicating that electronic noise is not the only or not the dominating limitation. The role of the charge sensor as a noise source and possible effects of coupling, back action [98] or sensor heating require further investigation.

The devices used here have outstanding charge stability, with noise on the dot energy level well below  $1 \mu\text{eV}$  [90, 100, 103, 104], making possible temperature measurements as low as  $\sim 10 \text{ mK}$  presented here. Still, device charge instabilities present a serious obstacle if much lower temperatures are to be reached, already severely impeding the measurements here. The temperature measurement would benefit from faster measurements, thus cutting off the noise spectrum at the lowest frequencies and reducing the effect of random telegraph noise. The obvious trade-off is increased signal noise at faster measurement speeds. We emphasize that the charge switching noise exceeds other setup noise such as the voltage sources on the gates, preamplifiers and Johnson noise of the sample wires.

Besides semiconductor charge instabilities, the GaAs nuclear spins can also act as a noise source, giving rise to a fluctuating Zeeman splitting and thus broadening of the single electron energy level (though the energy of a spin singlet would be immune to this noise). With GaAs hyperfine coupling constant  $A = 90 \mu\text{eV}$  [106] and number of nuclear spins  $N \sim 10^5$  to  $10^6$  enclosed in the electron wave function [107], the resulting energy fluctuations are of order  $A/\sqrt{N} \sim 0.1 \mu\text{eV}$ , and become a limiting factor for  $T \lesssim 1 \text{ mK}$ . Finally, heat release from sample holder or other components can also be a limiting factor, resulting in temperatures decaying slowly over a timescale of days. This is difficult to quantify in the present experiment due to the rather large error bars on the extracted temperatures.

---

In conclusion, we have measured the reservoir electron temperature  $T$  with a GaAs quantum dot in both direct transport and charge sensing. We find decent agreement with a CMN thermometer over a broad temperature range down to  $10 \pm 3\text{mK}$ . Currently, the main limitations are charge switching noise in the GaAs device, external electronic noise, heating effects due to the charge sensor as well as potential heat release at the lowest temperatures. Even lower temperatures might be achievable by further improving the setup and device, e.g. by better shielding and filtering, choosing materials with lower heat release and possibly optimizing the wafer material and device fabrication.

### Acknowledgements

We would like to thank G. Frossati, G. Pickett, V. Shvarts, P. Skyba, P. Stano, M. Steinacher and A. de Waard for valuable inputs. This work was supported by Swiss Nanoscience Institute (SNI), NCCR QSIT, Swiss NSF, ERC starting grant, and EU-FP7 MICROKELVIN and SOLID.

## 5 Electron Thermometry using Metallic Nanostructures and the Quantum Hall Regime in an Improved Experimental Setup

L. Casparis, D. Maradan, M. Palma, D. M. Zumbühl

*Department of Physics, University of Basel, CH-4056 Basel, Switzerland*

A. Feshchenko, M. Meschke, J. P. Pekola

*Low Temperature Laboratory (OVLL), Aalto University, 00076 Aalto, Finland*

### Abstract

A wide range of phenomena in solid state physics contain small energy scales and are therefore only accessible at very low temperatures. To achieve low temperatures in nanoelectronic devices, we use a nuclear refrigerator setup and investigate different kinds of electron thermometers. Here, we present measurements on a normal-metal / insulator / superconductor (NIS) junction which we use as a secondary and primary electron thermometer. The I-V curve maps the convolution of the Fermi-Dirac distribution of the normal metal with the superconducting BCS density of states. For secondary thermometry, we extract the size of the thermally broadened gap and observe that the NIS thermometer starts to saturate at temperatures below 20 mK. For primary thermometry, we fit the I-V curves in the linear regime right at the edge of the superconducting gap, where the slope is given by  $T$  only. We observe very good agreement of the mixing chamber temperature and the NIS thermometer between 100 and 45 mK. When using the nuclear refrigerators to cool the Cu stage below 1 mK, the NIS temperature saturates at  $\sim 5$  mK.



## 5.1 Introduction

The saturation of the electron temperature  $T_e$  at  $\sim 10$  mK in both metallic Coulomb blockade thermometers (CBT, chapter 3) and GaAs two dimensional electron gases (2DEG, chapter 4) is a disappointment, as the NRs of our demagnetization stage cool well below 1 mK (chapter 2). Apparently the parasitic heat leak to the sample is too large compared to the thermal conductance between the NR and the sample. Because we suspect the parasitic heat leak to be dominated by either external radiation or internal heat release of the used ceramic [5], we build a new chip carrier containing another filtering stage. The Macor socket is replaced by a homemade Ag-epoxy chip socket [108], which is cooled with a separate NR and rigidly attached to the support structure with three 15 cm long Vespel rods (SP-22), instead of Macor rods. We suspect internal transitions in the Macor to have caused heat release. Ag-epoxy is polymer based and therefore contains hydrogen, causing heat release as well, but due to its good electrical conductivity it can be more efficiently cooled than Macor. Before passing into the chip socket, all twenty measurement leads pass through a newly added Ag-epoxy microwave filter, similar to the microwave filter used at MC level [69]. The sample is mounted on a removable chip carrier (Ag epoxy) and is plugged with Au-plated pins into Au-plated jacks in the chip socket. The Au wire bond to the sample is done directly on the Au-plated pin. The filtered low  $T$  Faraday cage is completed by a thin Ag foil shield, which is screwed and glued to the chip socket.

Another approach would be to reduce the thermal resistance between NR and sample, i.e. by decreasing the Ohmic resistance to the 2DEG, an approach we also pursue [109].

After the above described change of the setup, we report in this chapter on the lowest electron temperatures to date in both metallic CBTs ( $\sim 5$  mK), as well as normal metal/insulator/superconductor (NIS) tunnel junction thermometers ( $\sim 5$  mK). Further, we demonstrate cooling of electrons in a 2DEG below the base  $T$  of the dilution

refrigerator (DR) by examining reentrant states in the fractional quantum Hall regime, although we are not able to establish an exact electron temperature, due to the undefined nature of the thermometer.

## 5.2 Coulomb Blockade Thermometry

In order to test the altered setup, we use two types of CBTs. Two-dimensional junction arrays, equivalent to the ones described in chapter 3, are used as secondary thermometers. The second type of CBTs investigated is a linear junction array, where 8 junctions are connected in series. This geometrically permits for larger metallic islands between the tunnel junctions, allowing for smaller charging energies  $E_C$ , as well as enhancing the cooling through electron-phonon coupling due to the larger volume  $\Omega$  of the island.

### 5.2.1 Two-Dimensional CBT Arrays

The two-dimensional CBT arrays consist of 7 parallel rows with 64 angle evaporated tunnel junctions between metallic islands ( $\Omega = 300 \mu\text{m}^3$ ). We use the conductance dip  $\delta g = 1 - g(V_{SD} = 0)/g_T$  as a secondary thermometer in order to avoid heating at finite bias [69, 84]. At higher temperatures where the CBTs are in thermal equilibrium with the refrigerator,  $E_C$  is determined through the relation  $\delta g = u/6 - u^2/60 + u^3/630$ , where  $u = E_C/(k_B T_{CBT})$  [70]. The differential conductance is measured using standard lock-in technique with the AC excitation experimentally chosen to avoid heating effects. At the lowest temperatures the zero bias conductance  $g(V_{SD})$  drops over a time span of several minutes and eventually saturates at a value  $g_{min}$ , which we use to determine  $\delta g$  and subsequently the electron temperature  $T_{CBT}$ . Figure 5.1 (a) shows  $T_{CBT}$  versus the temperature of the NR  $T_{Cu}$  for a device with total resistance  $\sim 500 \text{ k}\Omega$ . The extracted electron temperature starts to deviate from the NR temperature below  $\sim 15 \text{ mK}$  and saturates after demagnetization at  $T_{CBT} = 6.6 \pm 0.2 \text{ mK}$ . The inset of Fig. 5.1 (a) shows the corresponding thermometer calibration resulting in  $E_C = 17.7 \pm 0.1 \text{ mK}$ .  $T_{CBT}$  versus  $T_{Cu}$  for a different CBT ( $R \sim 150 \text{ k}\Omega$ ,  $E_C = 17.0 \pm 0.1 \text{ mK}$ , see inset of

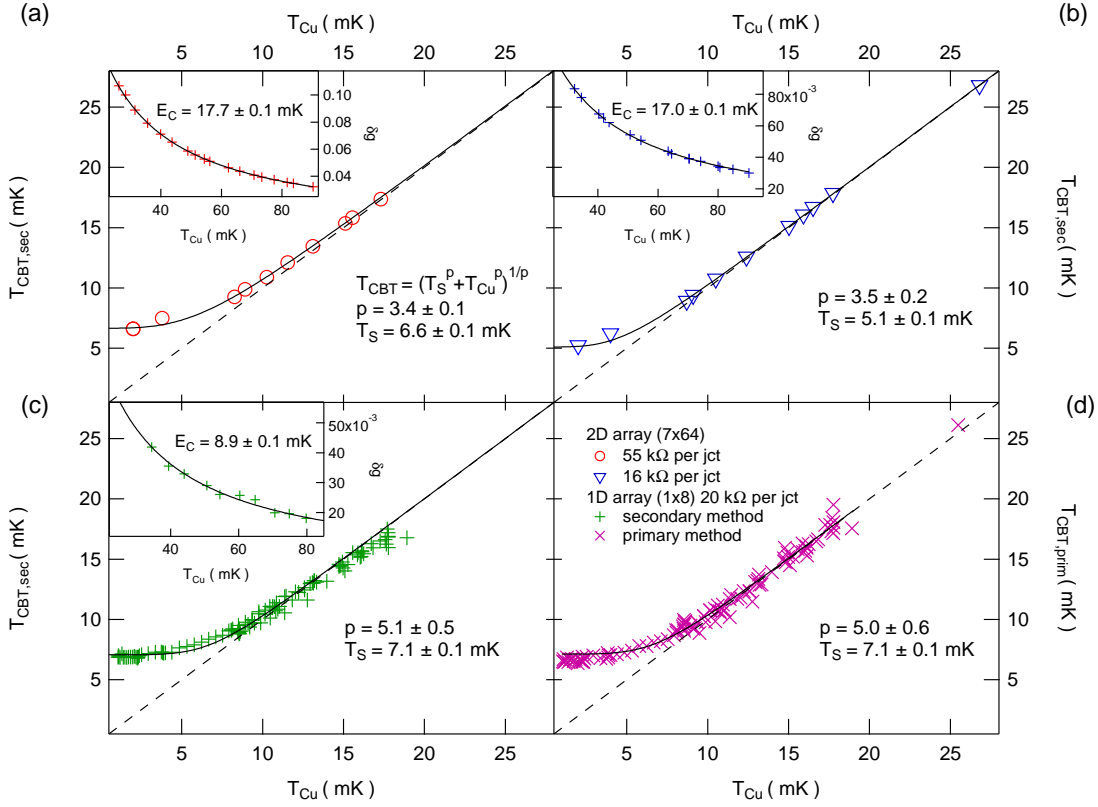


**Figure 5.1:** CBT data measured in the improved setup. The CBTs are measured in a perpendicular field of 100 mT. Ideal thermalization  $T_{CBT} = T_{Cu}$  is indicated in all plots with a dashed black line. (a)-(c)  $T_{CBT,sec}$  versus the NR temperature  $T_{Cu}$  for different sensors: (a) 2D array with  $7 \times 64$  junctions,  $55 \text{ k}\Omega$  per junction ( $R_{sensor} = 500 \text{ k}\Omega$ ), (b) 2D array with  $7 \times 64$  junctions,  $16 \text{ k}\Omega$  per junction ( $R_{sensor} = 150 \text{ k}\Omega$ ), (c) linear device with  $1 \times 8$  junctions,  $20 \text{ k}\Omega$  per junction. (d) The temperature obtained through the primary method  $T_{CBT,prim}$  for the same linear junction array. For all  $T_{CBT}$  curves we fit a saturation curve of the form  $T_{CBT} = (T_S^p + T_{Cu}^p)^{1/p}$  (solid, black). The insets show calibrations for the corresponding devices, where  $\delta g$  is measured at higher  $T_{Cu}$  to extract  $E_C$  (fit, solid black line).

Fig. 5.1 (b)) equivalent to the ones used in Ref.[69] are shown in Fig. 5.1 (b).  $T_{CBT}$  agrees very well with the refrigerator temperature down to the base temperature of the DR. Upon demagnetization the CBT cools, but saturates at an electron temperature  $T_{CBT} = 5.2 \pm 0.3$  mK. We note that by fitting the data with a power law  $T_{CBT} = (T_S^p + T_{Cu}^p)^{1/p}$ , we extract for both CBT arrays exponents  $p$  smaller than  $p=5$ , which would correspond to a dominant electron-phonon coupling mechanism. Thus in the two-dimensional CBT arrays, electron-phonon does not seem to be the dominant cooling mechanism anymore, consistent with previous observations [69, 84].

The lowest temperatures measured in the two-dimensional CBT arrays are already well below  $E_C$ , approaching the regime, where the validity of the secondary thermometry approximation is not given anymore, as the precision of the thermometer suffers at temperatures below  $T \sim 0.4E_C$  [110]. On the other side by using the third order approximation the error in temperature should still be smaller than 1%, very unlikely limiting our temperature measurement. Nevertheless we investigate linear junction arrays, where the volume of the metallic islands can be made much larger, and consequently  $E_C$  lower.

### 5.2.2 Linear CBT Array

The linear CBT arrays consists of 4 islands in series ( $\Omega \sim 40,000\mu\text{m}^3$ , compared to  $\sim 300\mu\text{m}^3$  for the 2D array), corresponding to 8 junctions in series. The resistance of each junction is  $\sim 20$  k $\Omega$ . After every second junction a bonding pad allows for individual island measurements. We do not observe a difference between measurements of 4 islands in series or individual islands. Figure 5.1 (c) shows  $T_{CBT}$  versus  $T_{Cu}$ , using the array as a secondary thermometer for the whole array of 8 junctions. The calibration in the inset of Fig. 5.1 (c) demonstrates the lower charging energy of this sensor ( $E_C = 8.9 \pm 0.1$  mK). Due to the smaller conductance dip the calibration also gets more difficult at the highest temperatures, explaining the deviations seen in the inset of Fig. 5.1 (c). The electron temperature again follows quite nicely the refrigerator

temperature down to the base  $T$  of the DR. After demagnetization the lowest temperature measured is  $6.8 \pm 0.1$  mK. A warm up curve after the demagnetization results in many points below the DR base  $T$ . If we fit a power law to  $T_{CBT}$ , we obtain an exponent  $p \sim 5$ , indicating that due to the larger island volume, the electron-phonon coupling dominates in the linear array. Nevertheless the linear array does not cool to lower temperatures than the two-dimensional array. We speculate that the silicon substrate of the CBTs could play a role for this temperature saturation. The silicon is undoped, therefore at the lowest  $T$  essentially insulating, making it very hard to cool. Potentially this can inhibit also cooling of the metallic CBT islands.

Another interesting observation is, that in contrast to the two-dimensional array, the linear array does not exhibit a long time constant for reaching the minimal conductance  $g_{min}$  at  $V_{SD} = 0$ . This indicates a shorter time constant to reach the equilibrium temperature, perhaps due to the largely reduced number of tunnel junctions. In any case this allows for primary electron thermometry [66], using the relation

$$T_{CBT,prim} = \frac{e}{5.134k_B N} V_{1/2}, \quad (5.1)$$

where  $N$  is the number of junctions and  $V_{1/2}$  the full-width half maximum (FWHM) of the bias voltage of the conductance dip. The extracted temperature for the linear CBT array acting as a primary thermometer is shown in Fig. 5.1 (d).  $T_{CBT,prim}$  agrees very well with the temperatures extracted from secondary thermometry. After demagnetization the lowest measured  $T_{CBT,prim} = 6.5 \pm 0.1$  mK. The power law fit again points toward a dominating electron-phonon coupling mechanism, as  $p = 5.0 \pm 0.6$ . The stronger electron-phonon coupling in the linear device is expected, as we increased the volume of the islands significantly. For an island with junction resistance  $20 \text{ k } \Omega$  and a volume of  $\Omega \sim 40,000 \mu\text{m}^3$ , assuming an electron-phonon coupling constant  $\Sigma = 2 \times 10^9 \text{ Wm}^{-3}\text{K}^{-5}$ , the crossover, where Wiedemann-Franz results in higher thermal conductance than electron-phonon coupling lies at  $\sim 2$  mK. The replacement of the Macor chip socket and carrier, clearly reduced the lowest temperatures measured,

potentially because of a smaller heat leak, either due to smaller heat release or less radiation. A similar problem poses the non-conducting backplane of the CBT, which is made out of Si. Thus it might be that we are not able to cool this substrate and thus it will inhibit a lower  $T_{CBT}$  due to electron-phonon coupling. It might be worth trying a conducting backplane (i.e. doped Si), in order to cool the backplane more efficiently and to see whether this helps lowering  $T_S$ .

## 5.3 Normal Metal/Insulator/Superconductor Thermometer

### 5.3.1 Introduction

It has been realized early on that a tunnel junction between a normal metal and a superconductor, a so called normal metal/insulator/superconductor (NIS) junction, cannot only be used to measure the gap of the superconductor [111], but also to detect small changes in the temperature of the normal metal [112, 113]. The current-voltage (I-V) characteristics of the junction are governed by the density of states (DOS) of both the superconductor and the normal metal. If the tunnel junction is made sufficiently opaque, a one-electron tunneling picture will provide a sufficient description, allowing to neglect many-electron tunneling effects, like cotunneling [114]. In this case, at low temperatures and at a small energy bias, the transport rates should vanish due to the gap  $\Delta$  in the Bardeen-Cooper-Schrieffer (BCS) DOS [115]. The energy level diagram of the NIS junction in Fig. 5.2 (a) depicts the situation at higher bias, where tunneling is allowed due to the empty states in the superconductor above the gap. Well below the critical temperature ( $T_C$ ) of the superconductor ( $T \leq 0.4T_C$ ), the BCS DOS is essentially independent on temperature. Thus only the normal metal DOS carries a temperature dependence, as the Fermi distribution is broadened by temperature. The sharp edge of the BCS DOS serves as a spectrometer for the normal metal energy distribution, very similar to deep Coulomb blockade thermometry, where a quantum dot with a very sharp linewidth probes the Fermi distribution of the 2DEG.

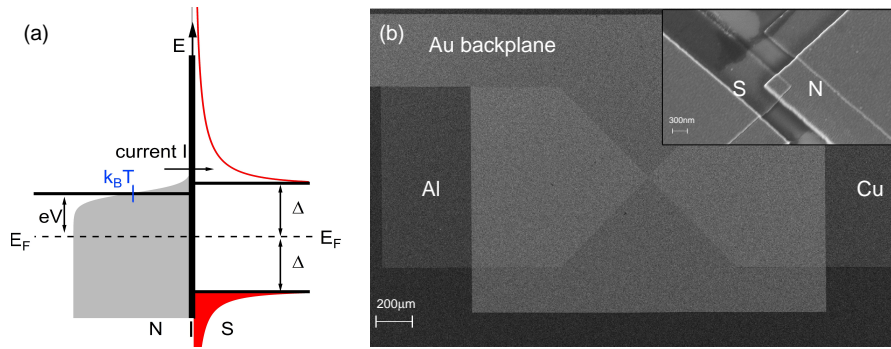


**Figure 5.2:** Normal metal/insulator/superconductor (NIS) junction. (a) Energy level diagram of a NIS junction. The energy gap of the superconductor  $\Delta$  forbids electron tunneling within the gap. A bias voltage  $V$  can induce a difference between the two chemical potentials, eventually leading to tunneling between the temperature broadened Fermi distribution (shaded, grey) and the BCS density of states above the gap (red). (b) SEM image of a device similar to the one used. The inset shows a zoom in of the junction region.

NIS thermometers are important tools for temperature measurements in mesoscopic systems, as they can be made very small and thus easily integrated into mesoscopic devices [116]. For example, NIS thermometry has been employed to measure single mode heat conductance of photons [117] and to demonstrate the Josephson heat interferometer [118]. Including the NIS into a resonant LC circuit enables temperature measurements with MHz bandwidth, potentially allowing for real-time thermal relaxation studies [119]. The lowest temperatures measured with NIS thermometers are around 50 mK [117, 120]. Promising for the use of NIS junctions at ultra-low temperatures is the very small self heating, due to very small currents flowing through the junction. Limitations of a NIS thermometer are the sensitivity to external  $B$ -fields, as this disrupts the superconductor. Further, due to sample to sample deviations from ideal theoretical behavior of the superconductor, NIS thermometers can hardly be described as primary thermometers [121]. For example local gap inhomogeneities, in the junction will result in a smeared superconducting gap. Another low  $T$  thermometry constraint might be the so called sub-gap leakage current. Although an ideal BCS DOS would not allow for any states within the superconducting gap, experimentally a finite current flows within the gapped region [116]. The states allowing for such a sub-gap

current can originate from Andreev reflection processes [122–125] or a smeared DOS within the gap [113], or similar effects like external radiation causing photon-assisted tunneling [126]. Andreev reflection can be avoided with sufficiently opaque junctions, the impact of a finite DOS within the superconductor will be discussed below in more detail.

By knowing how the normal metal is cooled (i.e. electron-phonon coupling), NIS thermometers can also be used as sensitive bolometers [113, 127, 128], because they can detect the slightest temperature changes. Moreover the NIS junction can be employed as spectrometer, where a single photon assisted tunneling effect can lead to current through the junction within the gap [126], even full DOS mappings of mesoscopic systems have been carried out [129]. Further, NIS junction have been demonstrated to function as electronic microrefrigerators [130–132]. When the junction is biased close to the gap voltage (see Fig. 5.2 (a)), only electrons occupying states above the chemical potential of the metal can tunnel into the superconductor – hot electrons are removed from the normal metal, and the electron temperature will be lowered. In combination with another NIS junction, which supplies cold electrons, temperatures can be reduced from 230 mK to 130 mK [133]. In the following we will restrict ourselves to NIS thermometry only, trying to implement it in our nuclear demagnetization setup.

### 5.3.2 Sample

Figure 5.2 (b) shows a SEM image of a NIS junction similar to the one used in our experiments. The junctions are fabricated on top of an undoped silicon wafer. At the bottom, in order to minimize environment-assisted tunneling effects [126], we evaporate a 80 nm thick Au ground plane. On top of that a 100 nm thick  $\text{Al}_2\text{O}_3$  film is formed by atomic layer deposition. The metallic junctions are then patterned and formed with standard e-beam lithography and shadow evaporation technique. After depositing 50 nm of Al, the superconductor is oxidized in situ. 150 nm of Cu is then evaporated at a different angle, resulting in a junction of 350 nm times 350 nm in size (see Fig. 5.2 (b))



inset). The normal metal and superconductor electrodes are both roughly  $1.1 \text{ mm}^2$  in area, together with the normal state tunneling junction resistance  $R_T \sim 14.2 \text{ k}\Omega$ , this makes cooling effects of the NIS junction negligible. In terms of gap inhomogeneities, it has been observed that thin films of Al behave as type II superconductors [134], where a perpendicular field can penetrate the thin film at vortex sites. There the superconducting gap is locally suppressed, leading to spatial gap inhomogeneities and allowing for quasiparticle relaxation. The length scale of this vortices is on the order of the coherence length  $\xi$ , which for bulk Al is  $\xi_0 \sim 1.6 \text{ }\mu\text{m}$ . In similar Al thin films than used in our experiments, a coherence length  $\xi \sim 100 \text{ nm}$  has been estimated from the relation  $\xi = 0.855(\xi_0 l)^{0.5}$ , where  $l$  is the normal state mean free path [135].

### 5.3.3 I-V Characteristics

All NIS thermometer measurements are DC measurements, with a long time constant (average over 100 ms) and a low pass  $RC$ -filter (5 Hz), with which we achieve a current noise of around 30 fA. To obtain the voltage over the junction, we have to subtract the voltage which drops over the in-line resistance of the filters (8.4 k $\Omega$ ). Figure 5.3 plots typical current voltage (I-V) curves of the NIS junction at different temperatures. The increasing size of the gapped region with lower temperatures can be easily recognized. For a more quantitative description of the current  $I$  through the junction, one can write

$$I = \frac{1}{eR_T} \int n_S(E) [f_N(E - eV) - f_S(E)] dE, \quad (5.2)$$

where  $V$  is the voltage across the junction,  $R_T$  the normal state junction tunneling resistance, the BCS DOS of the superconductor is  $n_S(E) = \left| \text{Re} \left( \frac{E}{\sqrt{E^2 - \Delta^2}} \right) \right|$  and  $f_N$  and  $f_S$  are the Fermi functions of the normal metal and the superconductor respectively ( $f_{N/S} = [\exp(E/k_B T_{N/S}) + 1]^{-1}$ ). For  $k_B T \ll eV, \Delta$ , the integral reduces to

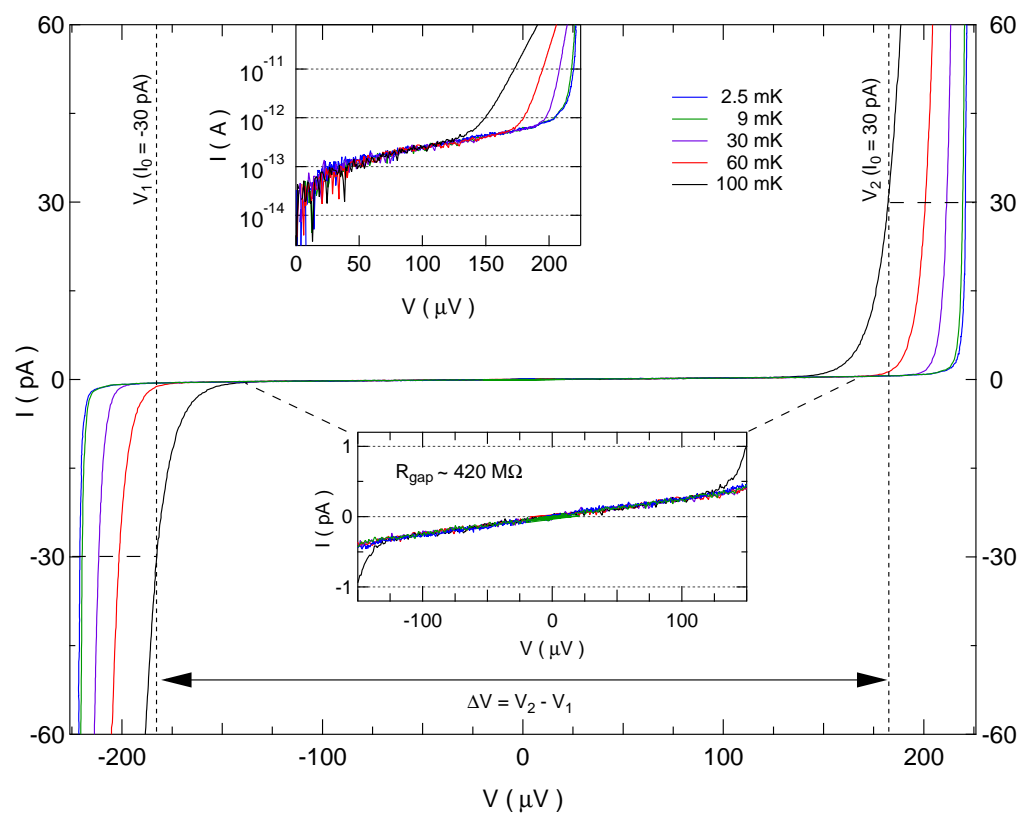


**Figure 5.3:** NIS current-voltage ( $I$ - $V$ ) curves for different temperatures well below  $T_C$  of Al. The vertical black lines indicate the extraction of  $\Delta V = V_2 - V_1$  for  $I_0 = 30$  pA. The lower inset is a zoom-in of the gapped region, displaying the typical linear form, which is temperature independent. The upper inset shows the log-version of the  $I$ - $V$  curve for three temperature.

$$I = \frac{1}{eR_T} \int_{\Delta}^{\infty} n_S(E) f_N(E - eV) dE. \quad (5.3)$$

Solving the integral for low  $T$  and to the lowest order for  $eV \leq \Delta$ , one finds

$$I \approx \frac{\sqrt{2\pi\Delta k_B T}}{2eR_T} e^{-(\Delta - eV)/k_B T}. \quad (5.4)$$

Equation 5.4 predicts an exponentially suppressed current within the gap  $eV < \Delta$ . Experimentally often a sub-gap current, linear in bias voltage, is observed [120, 126, 136]. Phenomenologically, the sub-gap leakage is well described with a Dynes density of states [137, 138], a BCS like DOS, including lifetime broadening in the superconductor. Recently it has been shown that the physical origin of the finite DOS in the gap is the result of environment-assisted tunneling [126] and is equivalent to the Dynes DOS formalism. Both mechanisms lead to an altered superconductor DOS,  $n_S^D(E) = \left| \text{Re} \left( \frac{E/\Delta + i\gamma}{\sqrt{(E/\Delta + i\gamma)^2 - 1}} \right) \right|$ , where  $\gamma$  is the Dynes parameter, effectively introducing states within the gapped region. Note that for  $\gamma \rightarrow 0$ , the original BCS DOS is restored. It can be shown that  $\gamma = \frac{R_T}{R_{gap}}$ , the ratio between the normal state tunneling resistance and the resistance in the gap [126]. The inset in Fig. 5.3 shows a zoom-in for transport within the gap. From a linear fit in this region we extract  $R_{gap} \sim 420 \text{ M}\Omega$ . Together with  $R_T \sim 14.2 \text{ k}\Omega$  this corresponds to  $\gamma \sim 2.8 \cdot 10^{-5}$ , comparable to the lowest leakages experimentally determined [126].

Solving Eq. 5.4, which is valid to the lowest order for  $eV \leq \Delta$ , for the voltage, leads to

$$V \approx \frac{\Delta}{e} - \frac{k_B T}{e} \ln \left( \frac{2eR_T I}{\sqrt{2\pi\Delta k_B T}} \right). \quad (5.5)$$

Therefore a simple expression for the voltage across the junction for a bias current  $I$  exists, depending only on  $R_T$  and  $\Delta$ . Upon inversion of the bias, current will flow in the opposite direction, but the bias dependence is symmetric around the Fermi energy  $E_F$ . Hence for a fixed current  $|I_0|$ , the difference between the voltages  $V_2(I_0)$  and  $V_1(-I_0)$

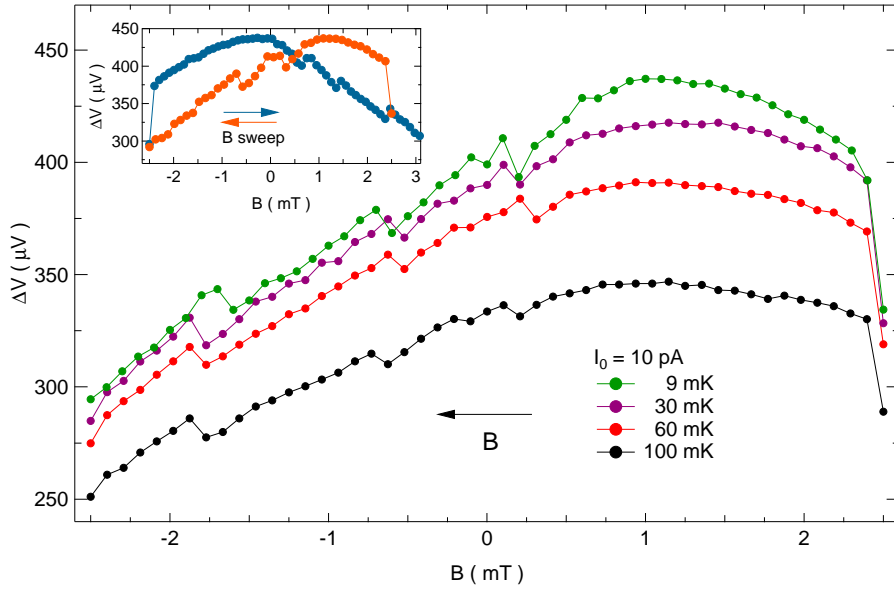


**Figure 5.4:**  $\Delta V$  for  $I_0 = 10$  pA as a function of magnetic field  $B$  for different temperatures. The field is swept from positive to negative  $B$ . The peak of  $\Delta V$  decreases at higher  $T$  and appears at non-zero field. The inset demonstrates hysteretic behavior, as the field position of the peak changes with opposite sweep directions.

is given by

$$\Delta V = V_2 - V_1 \approx \frac{2\Delta}{e} - \frac{2k_B T}{e} \ln \left( \frac{2eR_T I_0}{\sqrt{2\pi\Delta k_B T}} \right). \quad (5.6)$$

Thus  $\Delta V$  essentially increases linearly in temperature over a large range of temperatures. Figure 5.3 demonstrates how we extract  $\Delta V$  for  $I_0 = 10$  pA at 100 mK. Because of experimental issues like voltage drifts, we decide to measure the whole I-V curves as shown in Fig. 5.3 and then determine  $\Delta V$ .

### 5.3.4 B-Field Dependence

First, we investigate the effect of an external magnetic field on the NIS junction. Figure 5.4 plots  $\Delta V$  for  $I_0 = 10$  pA against the  $B$ -field for different temperatures, while the  $B$ -field is swept from positive to negative. There exists a field position for which  $\Delta V$  is maximal at  $B_{max} \sim 1$  mT, which is independent of temperature. After sweeping through  $B_{max}$ ,  $\Delta V$  decreases monotonically, disrupted by reproducible jumps at intervals of  $\sim 1$  mT. To check whether the non-zero  $B_{max}$  is caused by an external

field, we sweep the field in the opposite direction, shown in the inset of Fig. 5.4. Clearly  $B_{max}$  depends on the sweep direction, behaving hysteretically. Again jumps in  $\Delta V$  show up after passing through  $B_{max}$ . The origin of both the  $B$ -field offset and the jumps in  $\Delta V$  are presently not understood. For the jumps one could speculate that an addition of a vortex into the superconductor could aid quasiparticle relaxation [139], resulting in a reduced temperature of the superconductor, in turn giving rise to larger  $\Delta V$ . On the other hand for the area of the NIS junction ( $350 \text{ nm} \times 350 \text{ nm}$ ), one would expect an addition of a flux quantum only every 17 mT, an order of magnitude larger period than observed experimentally. Nevertheless a similar explanation has been used recently to address the improved performance of a NIS refrigerator at finite  $B$ -field [135, 139]. There the flux vortex, enabling quasiparticle relaxation in the superconductor and thus better cooling, has been determined to be inserted quite a distance away from the actual tunnel junction. We note that in our case the superconducting region away from the junction is very large  $\sim 1 \text{ mm}^2$ , and thus vortex induced relaxation in proximity to the junction might be possible on the observed field scales.

For thermometry,  $B_{max}$  represents the best field position, as the temperature sensitivity is largest there. Thus the presented  $\Delta V$  data is always extracted at the  $B$ -field position, where it is maximal. For dilution refrigerator operation  $B_{max}$  is very stable, as soon as we ramp up  $B_{demag}$ , the maximum will shift due to a finite stray field at the sample position ( $B_{max} \sim -60 \text{ mT}$  at  $B_{demag} = 9 \text{ T}$ ).

### 5.3.5 NIS Thermometry

Figure 5.5 displays  $\Delta V$  for three different  $I_0$  versus the temperature of the Cu NRs measured with a CMN and a LCMN at the lowest  $T$ . The CMN thermometer is calibrated using a standard fixed point device with 6 superconducting transitions between 1.2 K and 96 mK. The solid lines in Fig 5.5 are fits to the data points between 30 mK and 100 mK using Eq. 5.6. The current  $I$  we fix to  $I_0$  and the normal state resistance  $R_T$  to  $14.2 \text{ k}\Omega$ , the open fit parameter is  $\Delta$ , which should be independent of  $I_0$ . We

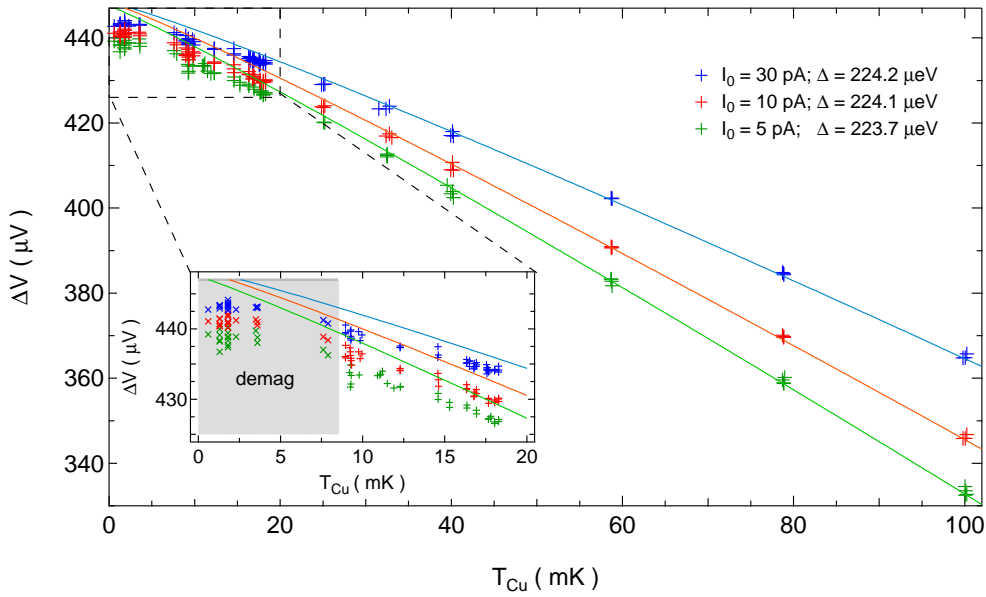


**Figure 5.5:**  $\Delta V$  as a function of  $T$  for different currents  $I_0$ . The solid lines are fits to  $\Delta V(T, I_0)$  between 100 mK and 15 mK to calibrate the temperature sensor. The fitted superconducting gaps  $\Delta$  are shown for the different  $I_0$ . The lower left inset shows a zoom in for the region below base  $T$  of the DR reach with demagnetization (shaded). A deviation of  $\Delta V(T)$  for  $T_{Cu} \leq 20$  mK from theoretical behavior become apparent.

find that  $\Delta/e \sim 224 \mu\text{eV}$ , consistent with previous reported superconducting gaps in thin film NIS junctions [113]. A slight dependence of  $\Delta$  on  $I_0$  is observed. For higher  $I_0$ ,  $\Delta$  is also increasing, this is why the three different fits do not converge to a single point for  $T_{cu} = 0$ . The inset of Fig. 5.5, which is a zoom-in for the measurements obtained at low  $T$  (the temperature region reached with demagnetization runs is shaded), shows that upon demagnetization the normal metal cools, as  $\Delta V$  increases a little bit. Fig. 5.3 already pointed toward this direction, where the 2.5 mK I-V curve is measured after demagnetization and shows a wider gapped region than the I-V curve at 9 mK. On the other hand, below 20 mK, the measured  $\Delta V$  starts to deviate from the expected values from the fits and eventually saturates. The saturation temperature after demagnetization is roughly 10 mK.

It could well be that the temperature of the NIS indeed does not drop below 10 mK. On the other hand, the sub-gap leakage might obscure the measurement at very low currents, as  $\gamma$  essentially broadens the I-V characteristics at the gap edge [120]. To

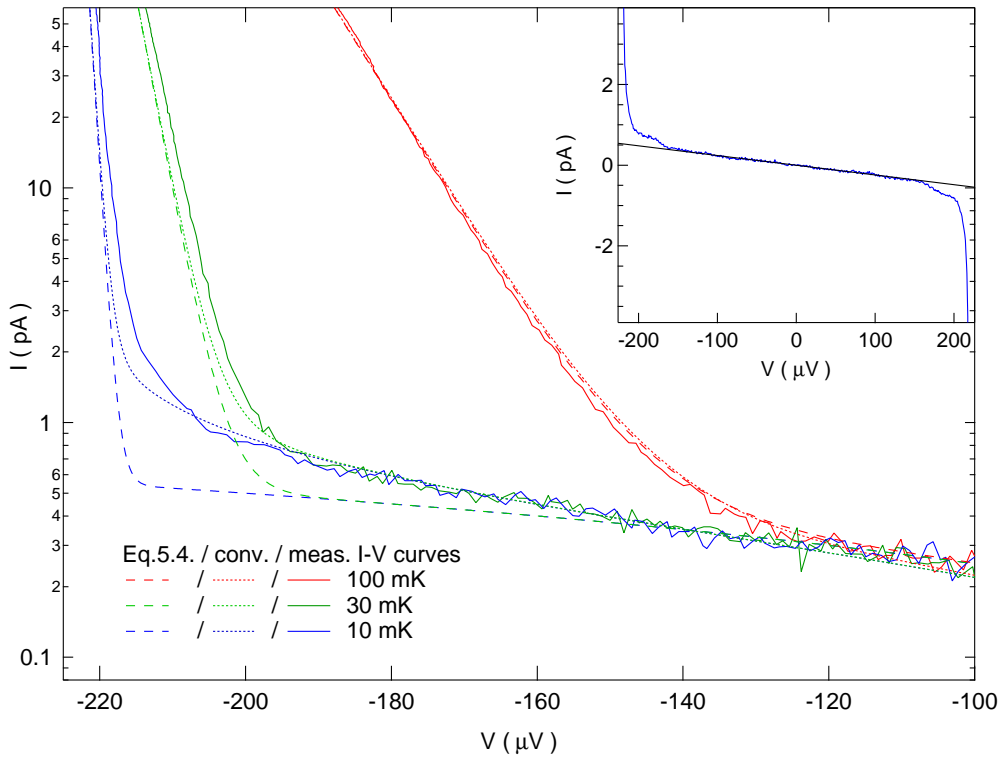


**Figure 5.6:** Comparison between the numerically calculated I-V curve using Eq. 5.3 (dotted), the I-V behavior expected from the approximation in Eq.5.4 (dashed) and the measured I-V curves (solid) for three different temperatures. The numerical calculation is a convolution of the Fermi distribution of the normal metal and the Dynes density of states in the superconductor ( $\Delta = 224 \mu\text{eV}$ ,  $R_T = 14.2 \text{ k}\Omega$ ,  $\gamma = 2.8 \cdot 10^{-5}$ ). The inset shows an I-V curve for both sides of the gap. A linear fit within the gap was added (black) to illustrate the effect of the additional tail right at the gap edge.

illustrate this effect, we plot a zoom-in on one flank of the I-V curves in Fig. 5.6. The plot compares measured curves (solid lines) with calculated  $I(V)$ , using Eq. 5.4 (dotted line) and solving the the integral (Eq. 5.3) numerically with a Dynes DOS (dashed line). The numerical calculation uses a Dynes parameter  $\gamma \sim 2.8 \cdot 10^{-5}$ , whereas we added a linear background corresponding to  $R_{gap} \sim 420 \text{ M}\Omega$  for  $I(V)$  calculated through Eq. 5.4. For both calculations we used  $R_T = 14.2 \text{ k}\Omega$  and  $\Delta = 224 \text{ }\mu\text{eV}$ . At 100 mK the agreement between the two calculations and measurement is very good. At 30 mK the effect of the Dynes DOS can be seen, as the two calculated  $I(V)$  differ at low currents. At 10 mK the difference is bigger, demonstrating that  $\gamma$  has an effect on  $\Delta V$  at the lowest currents. For  $I_0 = 5 \text{ pA}$  or below, we thus expect some kind of  $\Delta V(T)$  saturation due to  $\gamma$  [120]. Above  $I_0 = 10 \text{ pA}$  the two calculated  $I(V)$  agree well with each other, the leakage should therefore play no role there. This is not what we have observed in Fig. 5.5, where  $\Delta V(T)$  saturates irrespective of the current  $I_0$ .

Indeed from Fig. 5.6 it becomes apparent that the actual measurement deviates quite a bit from calculations – the measured current increases at lower absolute voltages than expected and never quite agrees with the calculations. The inset of Fig. 5.6 shows both flanks of an I-V curve (blue). The linear behavior within the gap is emphasized through a linear fit (black). At the edge of the gap there is a clearly visible additional increase of current, before the current starts to increase exponentially. As seen in the main plot of Fig. 5.6, this additional tail signifies a deviation from the I-V curve described by BCS theory. Including a Dynes DOS cannot reproduce the tail completely either. Therefore at the lowest temperatures and at currents below 20 pA the temperature reading from the NIS thermometer can become unreliable, as  $I(V)$  deviates from the expression in Eq. 5.3. Further the measured data never reaches the calculated curves, reflecting the saturation observed in Fig. 5.5. An explanation for the deviation at lower currents could be additional absorption of external radiation, for example black-body radiation. As the NIS junction is also a sensitive spectrometer, thermal radiation could allow for current right at the edge of the gap, effectively reducing the gap. The



maximum in the intensity distribution for black-body radiation at 10 mK is around  $4 \mu\text{V}$ , a value not inconsistent with the apparent voltage shift at the lowest currents. Further the voltage preamplifier can cause problems at these low currents, as it gives out a small current, giving rise to an increased measured current. As discussed at the end of this chapter, another explanation could be voltage noise across the device, broadening the Fermi-Dirac distribution. On the other hand the magnitude of the apparent voltage shift is larger than typical measured voltages noise ( $V_{rms} \sim 1 \mu\text{V}$ ). At this point, we cannot verify whether the deviation of the I-V curve at the edge of the gap is indeed stemming from blackbody radiation, but it seems that is certainly making a temperature measurement for the lowest  $I_0$  difficult.

An alternative but in principle equivalent way of extracting temperature is to fit the full  $I(V)$  curve. As a calibration we use the superconducting gaps extracted from the  $\Delta V(T)$  fits in Fig. 5.5. At elevated temperatures (above 40 mK) the full  $I(V)$  fits agree quite well with the data, reproducing the MC temperatures. At lower temperatures, again due to the deviations of the I-V curves from theoretical behavior at low  $T$ , the fits do not agree nicely with the data (not shown). The lowest temperature extracted using the full fit are similar to the ones extracted with the  $\Delta V$  method ( $T_{NIS} \sim 9 \text{ mK}$ ). Apart from the low current deviations, one of the problems with the full fit method is the  $I_0$  dependence of  $\Delta$ . Depending then on the exact  $\Delta$ , the extracted temperature can vary significantly.

Although in literature NIS junctions are not considered to be primary thermometers [116], mainly due to the uncertainty of the material parameter  $\Delta$ , which might vary from device to device. We now show that the NIS junction can constitute an absolute thermometer, not invoking  $\Delta$ . Using Eq. 5.4 one can show that the derivative of the natural logarithm of the current with respect to voltage is given by

$$\frac{\partial \ln I}{\partial V} = \frac{e}{k_B T_{NIS}}. \quad (5.7)$$

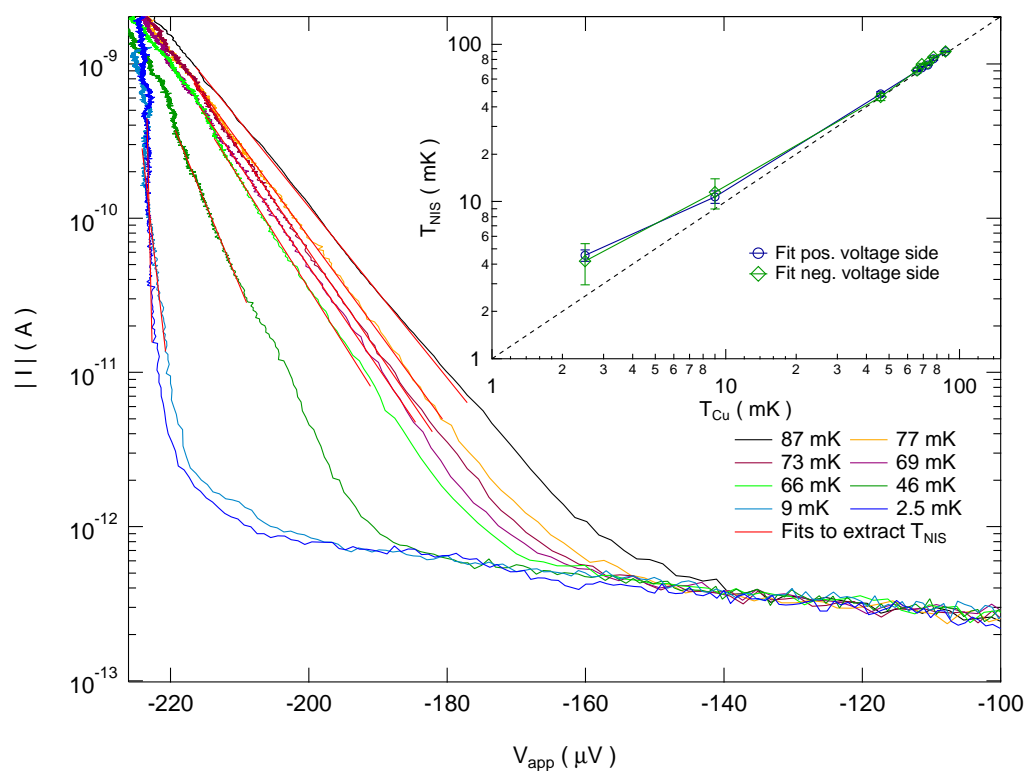


**Figure 5.7:** Primary NIS thermometer. I-V curves for a wider voltage range, where the currents increase up to  $\sim 2$  nA for different temperatures and with linear fits (red). The inset shows  $T_{NIS}$  extracted by the linear fits to  $\ln I(V)$  versus  $T_{Cu}$ . The dashed black line represents  $T_{NIS} = T_{Cu}$ .

As described above, this relation only holds where the approximation  $eV < \Delta$  is fulfilled. Further we neglect any higher order contributions for the approximation used to derive  $I(V)$  in Eq. 5.4, which can cause deviation from the linear behavior in  $\ln I(V)$ , when  $eV$  approaches  $\Delta$ . From the slope of linear fits to  $\ln I$  as a function of  $V$ , we can now directly derive the temperature without any additional calibration. Thus the NIS junction can serve as an absolute thermometer, depending on the temperature and the fundamental constants  $e$  and  $k_B$  only. The material parameter  $\Delta$  is eliminated with this method. Figure 5.7 plots several I-V curves at different temperatures for currents up to a few nA versus the applied voltage  $V_{app}$ . We use  $V_{app}$  instead of the measured  $V$  because small fluctuations of the measured  $V$  can have a large effect on the I-V curve. At very low  $T$  the current is increasing very strongly while the voltage is changing only very weakly (strong slope). We find that temperature fits become more reliable when plotting  $I(V_{app})$ . The inset in Fig. 5.7 plots the extracted  $T_{NIS}$  versus  $T_{Cu}$  from linear fits (red) to the curves displayed in the main plot (negative voltage) and on the other I-V flank (positive voltage, not shown in main plot). The dashed line indicates ideal thermalization.  $T_{NIS}$  at higher  $T_{Cu}$  agrees rather well with the MC temperature, although all  $T_{NIS}$  show a small offset ( $\sim 2$  mK) compared to  $T_{Cu}$ . This is something we expect from numerical calculations, where both the effect of  $\gamma$  and non-linear behavior in  $\ln I(V)$  close to the gap edge increase the temperature (not shown). This potentially absolute thermometer should be investigated in more detail in the future, especially because also the effect of heating due to the larger operating currents is unclear. For the moment we stick to our simple relation of Eq. 5.7. By doing so, at base  $T$  of the DR, we determine  $T_{NIS}$  to be  $\sim 11$  mK. Upon demagnetization the NIS junction cools, at  $T_{Cu} \sim 2.5$  mK,  $T_{NIS} \sim 4.5 \pm 1$  mK. The error of the linear fit itself is very small, the error displayed in the inset of Fig. 5.7, we obtain by fitting  $I(V)$  several times for different ranges within the linear regime.

In summary, we use a low leakage NIS junction ( $R_{gap} \sim 420$  M $\Omega$ ,  $\gamma = 2.8 \cdot 10^{-5}$ ) both as primary and secondary thermometer by measuring I-V curves across the junction.

We observe a dependence of the I-V curves on  $B$ -field. The position of the largest gap reading in field is hysteretic, something which is presently not understood. Measuring at the  $B$ -field with the largest gap, we demonstrate secondary NIS thermometry down to 10 mK. At the very lowest  $T$ , we observe a deviation from the theoretical I-V curve, which then limits the temperature reading and causes  $T_{NIS}$  to saturate. We speculate that the deviation of  $I(V)$  for low currents, could be due to background blackbody radiation. We further use the NIS junction as a primary thermometer. This is possible because for the approximation in Eq. 5.4 at higher currents,  $\frac{\partial \ln I}{\partial V}$  is constant and depends only on  $T$ . With this absolute method, we extract  $T_{NIS} \sim 4.5 \pm 1$  mK after demagnetization. Further studies to investigate the effect of the Dynes DOS and non-linear behavior close to the gap are needed to describe this thermometer in more detail. Further effects of heating due to the high currents flowing are not taken into account in our analysis. Similar to the CBT, the NIS junction is fabricated on top of a Si wafer. In order to improve shielding further and help to cool the substrate to lower  $T$ , it might be worth fabricating the next generation of NIS thermometers on a conducting backplane (i.e. doped Si).

#### 5.4 Reentrant State Quantum Hall Thermometer

After establishing with CBT and NIS thermometry, that we reach electron temperatures well below 10 mK in metallic nanostructures, we test cooling below base  $T$  of the DR in semiconducting samples. As a thermometer we use the temperature dependence of reentrant quantum Hall states in high mobility GaAs quantum wells [140–142]. These states are highly temperature sensitive at the lowest temperatures [143, 144], but unfortunately neither the underlying physics of these states nor the exact temperature dependence is known, making it only a qualitative diagnostic tool, rather than a quantitative thermometer.

The signature of reentrant integer quantum Hall states is that at some nominally fractional  $R_{xy}(B)$  as a function of field,  $R_{xy}$  jumps back or jumps ahead, assuming

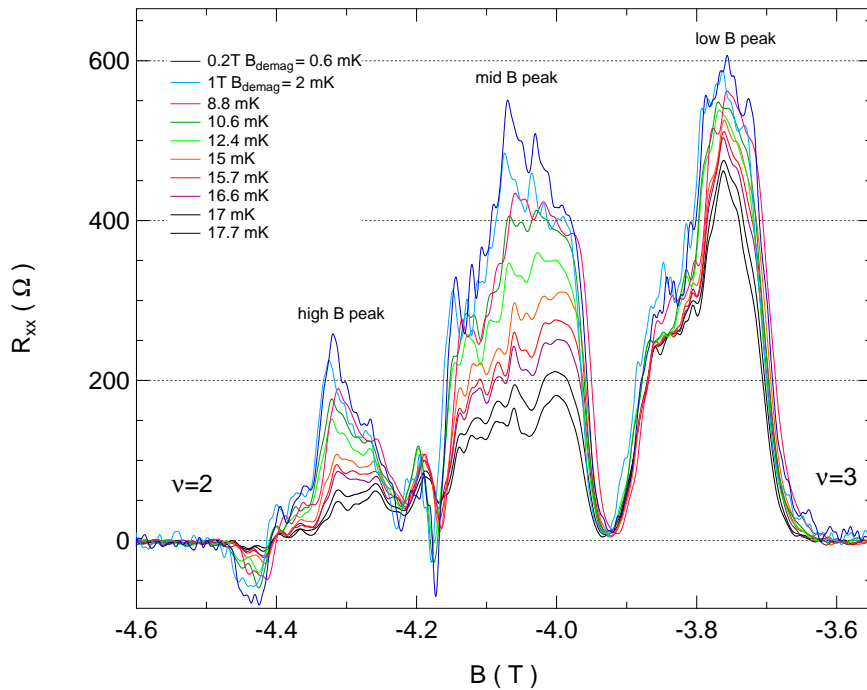


**Figure 5.8:** Longitudinal resistance  $R_{xx}$  as a function of magnetic field  $B$ , between filling factors  $\nu = 3$  and  $\nu = 2$  for different  $T$ . This side of  $B$ -field polarity shows only signature of reentrant states, see chapter 6 for details.

the quantized value of a neighboring integer filling factor [141, 142]. Due to a density gradient present in the sample, reentrant states show up in the longitudinal resistance  $R_{xx}$  [145] as peaks, at least for one  $B$ -field polarity. This helps us to separate the reentrant states from the conventional  $R_{xx}$  signal. For more information about the density gradient and its consequences, we refer to chapter 6. The nature of the reentrant states is presently still under investigation. They have so far only been observed at the lowest temperatures in the highest quality samples. It is speculated that they are a consequence of so called bubble phases [146]. Their abrupt temperature dependence [143, 144] and sensitivity to in-plane magnetic fields [143] has been interpreted as a melting of the bubble phases [144]. Nevertheless, at present a more detailed theoretical description is lacking. For estimating the electron temperature quantum Hall features have been previously used [80]. Peak height and position in field of  $R_{xx}$  values have been recorded as a function of temperature and then, by assuming a linear dependence on temperature, the lowest temperatures have been extrapolated. Here we follow a

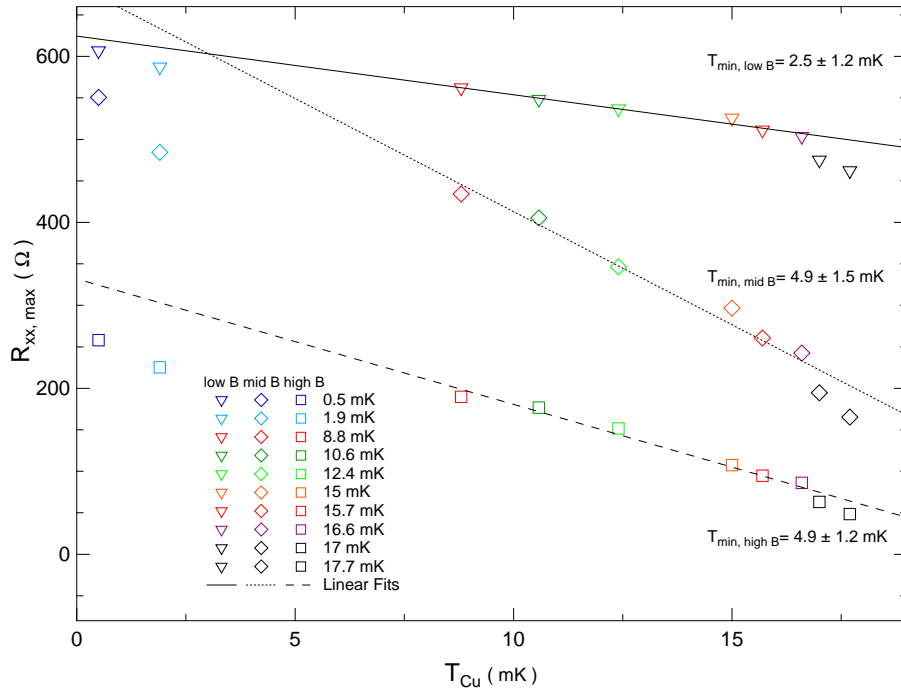


**Figure 5.9:** The maximum in longitudinal resistance  $R_{xx,max}$  from Fig. 5.8 for the three peaks at low (triangle), medium (diamond) and high (square)  $B$ -field versus  $T_{Cu}$ . The color code is the same as in Fig. 5.8. The black lines are linear fits for  $R_{xx,max}$  between 17 mK and 8.8 mK for high (dashed), medium (dotted) and low (solid) fields.

similar approach, but measure the reentrant features as a function of  $T$ , rather than conventional  $R_{xx}$  data. Due to the theoretical void this allows only for a qualitative measurement, but with this method we demonstrate cooling of electrons in a 2DEG upon demagnetization.

The sample, which is described in more detail in chapter 6 (sample A therein), is measured with standard four-wire lock-in techniques, with an a.c. current-bias excitation of 0.5 nA at 2.4 Hz. The bulk mobility of the device at base  $T$  is  $\mu = 1.9 \times 10^7 \text{ cm}^2 \text{ V}^{-1} \text{ s}^{-1}$ , the electron density is on the order of  $2.3 \times 10^{11} \text{ cm}^{-2}$ . The 2DEG is electrically contacted with In soldered contacts, resulting in very low resistive ohmic contacts.

Figure 5.8 shows  $R_{xx}$  versus  $B$ -field between filling factors  $\nu = 3$  and  $\nu = 2$  for different  $T$ . The  $B$ -field is swept with  $0.12 \text{ mT s}^{-1}$  in order to avoid heating of the sample. Three reentrant quantum Hall states manifest themselves as peaks in  $R_{xx}$ , which we name high  $B$ , mid  $B$  and low  $B$  peaks according to their position in  $B$ -field. The height

and position of the peaks is independent on  $B$ -field sweep direction. As the reentrant quantum Hall states usually appear within a very small temperature range [144], we only plot  $R_{xx}$  below 18 mK. Above  $\sim 30$  mK the peaks in  $R_{xx}$  are barely visible anymore (not shown). We observe more pronounced reentrant states at lower temperatures for all three reentrant features, as  $R_{xx}$  increases for lower  $T$ . Due to the quality of the sample the reentrant  $R_{xy}$  values do not yet reach the quantized value of one of the neighboring integer filling factors, thus this obvious source of low  $T$  saturation can be excluded.

In order to characterize the temperature dependence further, we plot in Fig. 5.9 the peak values  $R_{xx,max}$  of the all peaks versus temperature. The temperature sensitivity is largest for the mid  $B$  peak, but all peaks clearly increase in resistance at lower  $T$ . After demagnetization,  $R_{xx,max}$  is higher than at base T, demonstrating further cooling. If we use a linear fit between 17 mK and 8.8 mK as a calibration, the temperature after demagnetization to  $B_{demag} = 0.2$  T is  $\sim 5 \pm 1.5$  mK for the peaks at high and medium B-field. The temperature extracted through the low field peak is  $\sim 2.5 \pm 1.2$  mK.

## 5.5 Electrical Noise as a Limiting Factor for Reaching $\mu\text{K}$ Temperatures

The experiments presented above demonstrate that we can cool both metallic and semiconducting nanostructures to  $\sim 5$  mK or below. In order to explain the saturation at low  $T$ , we considered the equilibrium situation, where the heat that is removed from an object will at some point be canceled by the heat leaking into the object. Crucial for this balance is the thermal resistance  $R_{th}$  between the object and the cold reservoir. For a given heat leak, the higher  $R_{th}$ , the higher the temperature difference between the reservoir and the object will be (Eq. 2.1). Our conclusion has been one hand side that the heat leak to our device is too high, thus we introduced additional shielding and filtering, replaced potentially unfavorable material, and tried to reduce measurement related heating i.e. minimize bias. Depending on the dominant

coupling mechanism, the temperature dependence of the thermal resistance can differ significantly, making the approach of reducing heat leaks quite inefficient in certain cases. For electron-phonon coupling the saturation temperature is depending only very weakly on the residual heat leak  $\dot{Q}_0$ ,  $T_S \propto \Omega \dot{Q}_0^{1/5}$ . Therefore another promising route for circumventing this limitation, is to reduce  $R_{th}$  by increasing the volume  $\Omega$  of the object. Using another channel for heat conduction with a more beneficial temperature dependence (i.e. Wiedemann-Franz) is the other option to achieve lower  $R_{th}$ . We tried to reduce  $R_{th}$  with both approaches, but all the experiments resulted in similar saturation temperatures. This could mean that some other effect could limit us at the lowest temperatures. For example the Si backplane of the CBT and NIS chips releasing heat over a long time scale or not cooling to low lattice temperatures due to their insulating nature.

Another explanation for the saturated temperatures and their insensitivity to improvements of  $R_{th}$ , could be noise. We thus consider the effect of electrical noise, which does not exactly heat up our devices by heat dissipation, but broadens the Fermi-Dirac distribution. It is important to note that all electron thermometers discussed in this and other chapters (chapters 3 and 4) are essentially mapping the thermally broadened Fermi-Distribution in a reservoir of electrons. Voltage noise can be regarded as fluctuations of the chemical potential in the reservoir. For a measurement slower than the fluctuations, the Fermi-Dirac distribution will appear broadened due to these fluctuations. We now try to estimate the broadening of the Fermi distribution for two different devices, metallic CBTs and quantum dot CBTs and show how this will change the temperature reading of the thermometers. From our estimate we deduce that this line broadening can play a role for temperatures below 10 mK, potentially being one of the limiting factors for cooling below 1 mK.



### 5.5.1 Metallic CBT

According to Eq. 5.1, for primary electron thermometry with a CBT, one has to measure the full-width half maximum (FWHM)  $V_{1/2}$  of the differential conductance dip. For simplicity we approximate this conductance dip with a Lorentzian lineshape. In order to estimate the line broadening due to voltage noise, we assume a Gaussian voltage noise distribution around zero, thus the variance is given by the typically measured root mean square voltage ( $V_{rms} = \sigma$ ). The FWHM of the noise distribution can be calculated through

$$f_G = 2\sigma\sqrt{2\ln(2)}. \quad (5.8)$$

For the broadening of the CBT Lorentzian lineshape due to the Gaussian noise distribution we consider a convolution of the two lineshapes, resulting in a Voigt profile [147]. The FWHM of the Voigt profile can be approximated by

$$f_V \approx 0.5346f_L + \sqrt{0.2166f_L^2 + f_G^2}, \quad (5.9)$$

where  $f_L$  is the FWHM of the Lorentzian distribution [147], which again according to Eq. 5.1 is directly proportional to  $T_{CBT}$ .

Due to the voltage noise, the FWHM of the Voigt profile will always be larger than for the pure Lorentzian distribution ( $f_V \geq f_L$ ). Hence the extracted temperature  $T_{ext}$  will be larger than the actual device temperature  $T_{CBT}$ . By substituting, one can write  $T_{ext}$  as a function of  $V_{rms}$  and  $T_{CBT}$

$$T_{ext} = 0.5346T_{CBT} + \sqrt{0.2166T_{CBT}^2 + \frac{4e^2V_{rms}^2 2\ln(2)}{5.1345Nk_B}}. \quad (5.10)$$

Figure 5.10 shows  $T_{ext}$  from a single island device ( $N=2$ ) as a function of  $T_{Cu}$  and for different noise levels. For base temperatures of the dilution refrigerator  $\sim 9$  mK, the effect is rather small: for typical voltage noise levels of  $1 \mu\text{V}$  measured over the device, the extracted temperature should be roughly 9.7 mK. This is not inconsistent

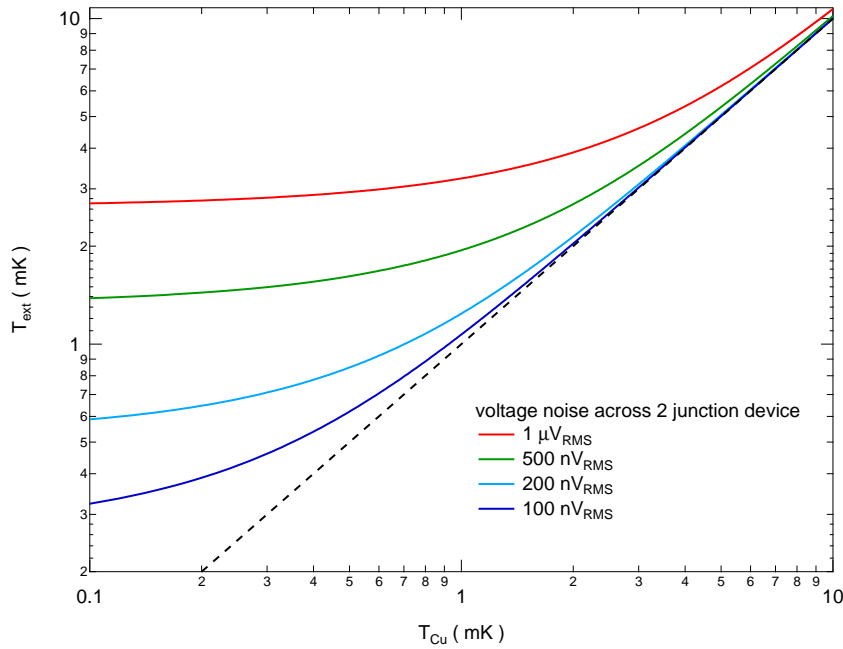


**Figure 5.10:** The extracted temperature of a single island (two junctions,  $N=2$ ) CBT device as a function of the NR temperature  $T_{Cu}$  calculated through Eq. 5.10 for different voltage noise levels. The dashed black line indicates the case for no voltage noise.

with our measurements, but could well be due to other effects. It should be noted that the voltage noise is measured on top of the fridge, thus it is not clear that the sample sees the exactly same  $V_{rms}$ . Due to the many filtering stages in our system which are which can work in both directions,  $V_{rms}$  at the sample could be both higher and lower than on top of the fridge. In a simple picture where the noise sources lie at room temperature (we neglect low  $T$  Johnson noise of our two stage filters ( $\sim 80$  nV) and noise coming from the wafer), the noise at the sample should be lower than on top, due to the significantly reduced bandwidth.

The number of junctions  $N$  plays an important role: from Eq. 5.10 it becomes clear that for an array of tunnel junctions the line broadening can be reduced due to a larger  $N$ . The saturation temperature in the limit where  $T_{Cu} \rightarrow 0$  is given by  $T_S = \frac{5.32mK}{N\mu eV_{rms}}$ . For the linear array of tunnel junctions we do not observe a dependence of  $T_S$  on the number of tunnel junctions, probably because of lower actual noise levels at the device and some other effect, preventing lower  $T_e$ .

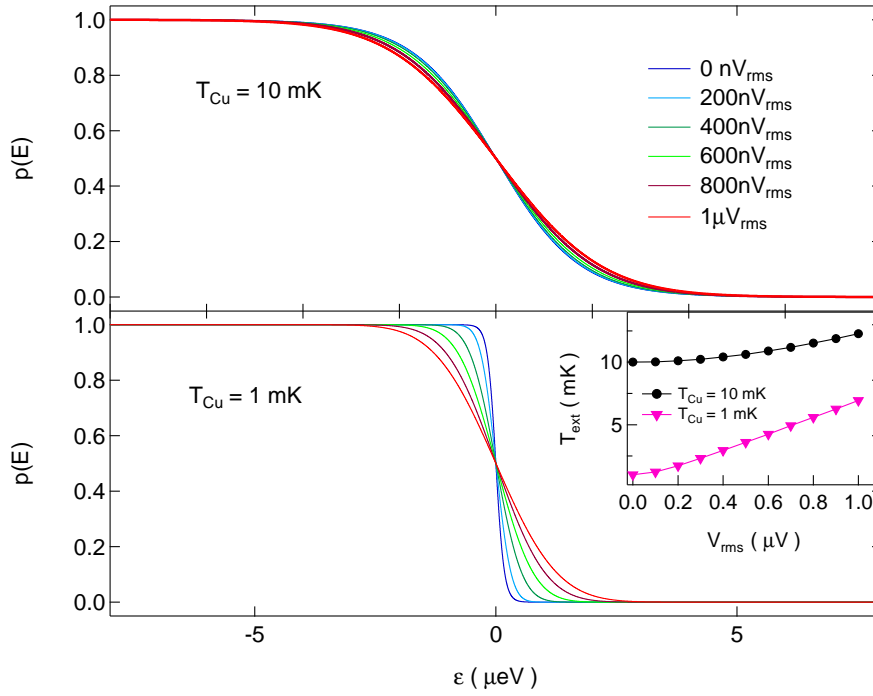


**Figure 5.11:** Convolution of Fermi-Dirac distributions with Gaussian voltage noise distribution for different  $V_{rms}$  for a fixed  $T_{Cu}$ . The calculated occupation probability  $p(E, V_{rms})$  is plotted as a function of energy with respect to the Fermi energy ( $\epsilon = \mu - E_F$ ) for  $T_{Cu} = 10$  mK (top panel) and  $T_{Cu} = 1$  mK (bottom panel). The inset shows the extracted temperatures  $T_{ext}$ , obtained by applying a Fermi-Dirac fit to the broadened distributions, as a function of  $V_{rms}$ .

### 5.5.2 Quantum Dot Coulomb Blockade Thermometry

Quantum dot thermometers, operated in the deep Coulomb blocked regime, probe the Fermi-Dirac distribution of the 2DEG with the sharp dot level. In order to account for the effects of noise in this specific case, we convolve the derivative of the Fermi-Dirac distribution ( $\propto \cosh^{-2}(\frac{\mu - E_F}{2k_B T})$ ) with the Gaussian noise distribution. As we are not aware of any analytical function for this convolution, we first take the derivative of the Fermi-Dirac function for a given temperature  $T$ . Then we numerically convolve this derivative with a Gaussian distribution and then numerically integrate this convolution to obtain the occupation probability distribution, which appears broadened.

Figure 5.11 displays the calculated curves resulting from the convolution for  $T_{Cu} = 10$  mK (top panel) and  $T_{Cu} = 1$  mK (bottom panel) for different  $V_{rms}$ , showing a clear

broadening of the distributions with increased noise. The inset plots the extracted temperatures  $T_{ext}$ , if the broadened distributions are again fitted with a Fermi-Dirac function. It becomes clear that the line broadening can effectively increase the temperature measured with the quantum dot thermometer. It is interesting that in the case of the metallic CBT,  $1 \mu\text{V}$  of noise at base temperature increases the extracted temperature by  $\sim 7\%$ , whereas for the quantum dot thermometer the effect is more pronounced, as  $T_{ext} = 12.3 \text{ mK}$  at  $T_{Cu} = 10 \text{ mK}$ , a  $23\%$  increase. The difference between the two cases is that the Lorentizan FWHM for the metallic CBT is given by  $5.1345Nk_B T$ , whereas in the case of a quantum dot thermometer the FWHM of the  $\cosh^{-2}$ -function is given by  $3.5k_B T$ . For  $N = 2$  the FWHM of the CBT is thus factor 3 larger, making it less vulnerable to line broadening due to voltage noise. Increasing the number of junctions  $N$  can further reduce the effect of voltage noise line broadening. A way around this effect would be to suppress voltage noise by filtering more, although the device can also have some intrinsic noise, which has the same line broadening effect [100]. Another option is to measure the Fermi-Dirac distribution on a faster time scale than the fluctuations occur, which is technically challenging. Last but not least, one could try to cool another degree of freedom, less susceptible to electrical noise, through the electron bath, similar to a Pt nuclear magnetic resonance (NMR) thermometer.

Finally, we note that these line broadening effects will occur in any thermometer mapping the Fermi-Dirac distribution, as long as the measuring time is long compared to the time scale of the fluctuations. Therefore also NIS thermometers are susceptible to this effect. We have not analyzed the effect of voltage noise on the NIS thermometer in detail, but it should be similar to quantum dot thermometers, because the Fermi distribution is broadened in the same way. The NIS junction might even serve as a testing ground, in order to study the line broadening experimentally. Because of the large device resistance, an artificial voltage noise broadening should be experimentally realizable without significant Joule heating. Nevertheless such noise experiments should be carefully designed to avoid any additional, unwanted heating.

---

## 6 Longitudinal Resistance Quantization and Density Gradient in the Integer Quantum Hall Regime

L. Casparis, M. Lafkioti, T.-M. Liu, D. Maradan,

D. M. Zumbühl

*Department of Physics, University of Basel, CH-4056 Basel, Switzerland*

C. Reichl, W. Dietsche, W. Wegscheider

*Solid State Physics Laboratory, ETH Zürich, CH-8046 Zürich, Switzerland*

### Abstract

We present quantum transport measurements in high-mobility GaAs 2D electron gases at low temperatures. We find a novel sequence of finite resistance plateaus in longitudinal resistance  $R_{xx}$  in the integer quantum Hall regime, accompanied by a striking  $B$ -field asymmetry and weak or absent fractional quantum Hall states. These signatures can be well understood with charge density gradients across the sample, as confirmed by  $R_{xy}$  data. The activation energies of the novel  $R_{xx}$  plateaus are surprisingly small, allowing experimental observation only at the lowest temperatures and in ultra-clean samples. Density gradients can be reduced with improved waver growth (rotation) and smaller distances between ohmic contacts. Nevertheless, our results show that  $R_{xx}$  can easily be misleading, characterizing gradients rather than quantum Hall gaps, thus fundamentally jeopardizing  $R_{xx}$  as the predominant probe of integer and fractional quantum Hall physics.

This chapter is prepared for publication.

## 6.1 Introduction

The quantum Hall effect (QHE) is observed in two-dimensional electron gases (2DEGs) exposed to high magnetic fields, where the density of states is described by Landau levels. The characteristic signature of the QHE is a quantized off-diagonal resistivity  $\rho_{xy}$  in steps of  $\frac{h}{\nu e^2}$ , where the integer  $\nu$  is the filling factor, indicating the occupation of the Landau levels. Concurrently, the diagonal resistivity  $\rho_{xx}$  is zero because of avoided backscattering. In high quality 2DEGs, electron-electron interactions can lead to the formation of an additional energy gap within the Landau levels, resulting in the fractional QHE (FQHE), where  $\nu$  is a rational number. The composite fermion picture has been extremely successful in describing the FQHE by combining flux quanta and electrons to form composite quasiparticles [6]. The theory can account for the existence of odd denominator FQHE states. However even denominator states have been observed experimentally [63, 78, 148], most prominently the  $\nu = 5/2$  state in the second Landau level. Moore and Read have proposed a many body wavefunction describing the ground state of the  $\nu = 5/2$  state [19]. This ‘‘Pfaffian’’ state has received considerable interest due to its exotic quantum statistics which are predicted to be non-Abelian. Kitaev and Das Sarma *et al.* have envisioned a fault tolerant topological quantum computer exploiting the non-Abelian nature of the  $\nu = 5/2$  quasiparticles [149–151]. Other theoretical proposals put forward the realization of Majorana fermions in the  $\nu = 5/2$  state [61]. On the experimental side, a major effort has been put into confirming the Moore-Read description through various experiments, including quasiparticle shot-noise [152], quasiparticle tunneling [80, 153], interferometry [154–156] and spin polarization [157] measurements. These experiments are complicated by the small energy gap of the  $\nu = 5/2$  state,  $\Delta_{5/2} \sim 600$  mK [158], which is roughly 4 times smaller than theoretically calculated [159]. Considerable efforts have been put into optimizing wafer growth in order to increase the energy gap and also to get some insight into the mechanisms limiting  $\Delta_{5/2}$  [144, 158, 160, 161]. From the observation of the  $\nu = 5/2$  state only at the highest mobilities it has been realized, that disorder

plays a crucial role in the stability of the 5/2 state. Although the correlation between mobility and  $\Delta_{5/2}$  has not been so clear in later experiments [144, 162]. Recent results suggest that disorder is indeed a key ingredient [161, 163], but a distinction has to be made between remote impurities, background impurities, alloy disorder in the 2DEG and the interface roughness.

The typical way of extracting  $\Delta_{5/2}$  is by determining the increasing  $\rho_{xx}$  (by measuring the differential longitudinal resistance  $R_{xx}$ ) as a function of temperature. Due to the increased population of the excited state, causing scattering across the sample bulk, the temperature dependence of  $\rho_{xx}$  allows for identification of the thermal activation over the ground state. It has been previously shown that this method of extracting the energy gap can be fundamentally flawed in the presence of a density gradient, because in that case  $R_{xx}$  contains no information about the underlying  $\rho_{xx}$  [145, 164]. *Pan et al.* also observed a quantization in  $R_{xx}$  similar to the one reported in this letter, but only in the special case for reentrant states next to fractional states.

## 6.2 Experiment

In this letter we report on quantized Shubnikov-de-Haas (SdH) oscillation peaks in longitudinal differential resistance  $R_{xx}$ . The strength of this quantization is dependent on the measured contact pairs. Our data can be explained by invoking a charge carrier density gradient. A simple binary charge carrier density gradient model, which is based on the edge channel picture is discussed. The binary gradient model also can account for the highly asymmetric behavior of  $R_{xx}$  with respect to the sign of the magnetic field  $B$ . Additionally, we investigate the temperature dependence of the  $R_{xx}$  quantization. An energy gap associated with the density gradient can be extracted and possibly explain why such a clear observation of the  $R_{xx}$  quantization has to the best of our knowledge not been reported before, as these gaps are on the order of few tens of millikelvin the most. Therefore very low electron temperatures seem to be a prerequisite for the observation. We further demonstrate that the density gradient has

an impact on the energy gap determination of the fractional states  $\nu = 5/2$  state. Our data shows that the role of disorder and temperature saturation in these systems is not resolved yet and fundamentally questions the role of  $R_{xx}$  as a characterization for fractional quantum Hall states.

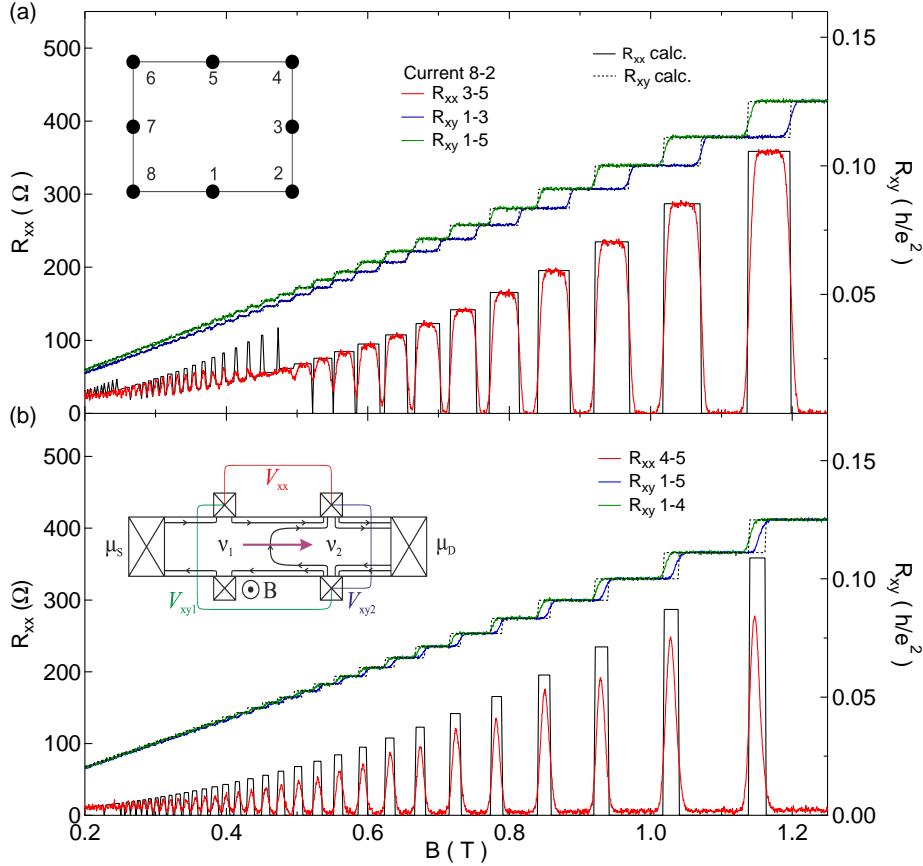


**Figure 6.1:** Longitudinal resistance quantization. (a) The inset shows a sample contact scheme. Transversal resistance  $R_{xy}$  (blue, green) for contact pairs 1-3 and 1-5 versus magnetic field  $B$ . The corresponding longitudinal resistance  $R_{xx}$  (red) for contacts 3-5 versus magnetic field  $B$ , current flows through contacts 8-2. Black traces are calculated  $R_{xy}$  (dashed) and  $R_{xx}$  (solid), based on a binary gradient model, see text. (b)  $R_{xy}$  and  $R_{xx}$  for a different voltage probe configuration with the same current contacts 8-2 and calculated  $R_{xy}$  (black, dashed) and  $R_{xx}$  (black, solid). The inset illustrates an edge channel picture for the measured device with a density gradient (purple arrow), resulting in two filling factors  $\nu_1$  and  $\nu_2$ .

### 6.2.1 Samples

The devices used in this work are AlGaAs/GaAs quantum wells grown by molecular beam epitaxy (MBE). Two different samples from different wafers are measured. For



sample A the 2DEG forms in a 30 nm wide potential well which lies 245 nm below the surface. Sample B contains a 30 nm wide 2DEG, buried 195 nm below the surface. It is important to note that the two wafers have not been rotated during MBE growth. The bulk mobility of device A at base temperature is  $1.9 \times 10^7 \text{ cm}^2 \text{ V}^{-1} \text{ s}^{-1}$  and the electron density is on the order of  $2.3 \times 10^{11} \text{ cm}^{-2}$ . The 2DEGs are electrically contacted on all 4 corners and in the middle of the 4 edges with In soldered contacts. For a sample contact scheme of this van-der-Pauw geometry see the inset in Fig. 6.1 (a), the samples are roughly 4 mm times 6 mm in size. Measurements on sample A are carried out in a dilution refrigerator with a base temperature of 9 mK using standard four-wire lock-in techniques, with an a.c. current-bias excitation of 2 nA at 2.4 Hz. The setup has been optimized for low temperature measurements, including several filtering stages and Ag sinters in the mixing chamber, thermalizing every measurement lead [84]. The differential longitudinal resistance  $R_{xx}$  and the two corresponding differential Hall resistances  $R_{xy}$  are measured simultaneously as a function of magnetic field. All quoted temperatures are measured using a Cerium Magnesium Nitrate (CMN) thermometer mounted on the mixing chamber. The CMN thermometer was calibrated using a standard fixed point device with 6 superconducting transitions between 1.2 K and 96 mK.

### 6.2.2 Magnetic Field Dependence

In Fig. 6.1 (a)  $R_{xx}$  between contacts 3 and 5 (current flowing through contacts 8 and 2) is plotted against magnetic field  $B$  for sample A. At low field SdH oscillations are visible, exhibiting a clear beating pattern (see also Fig. 6.2 (a) inset), indicating the presence of two different densities. At higher fields the minima in  $R_{xx}$  reach zero, as expected. The striking feature of our data is the quantized value of the maxima in  $R_{xx}$ , visible as clear flat-top peaks. The corresponding  $R_{xy}$  traces for contacts 3 and 5 provide further evidence, that the densities for contacts 3 and 5 significantly differ. Analyzing the slope of the two  $R_{xy}$  traces in the low field region gives the two different

densities  $n_1 = 2.36 \times 10^{11} \text{ cm}^{-2}$  and  $n_2 = 2.48 \times 10^{11} \text{ cm}^{-2}$ . With a definition for the density gradient,  $\frac{2\Delta n}{n_1+n_2}$ , this results in a 5% density gradient. The dashed black curves are calculated Hall resistances for  $n_1$  and  $n_2$ , fitting the experimental data quite well. The black solid line is the difference between the calculated  $R_{xy}$  for the two densities, reproducing the quantization in  $R_{xx}$ . Thus the quantization in  $R_{xx}$  is the consequence of a difference in density on the order of 5% within the sample. As the density gradient might be anisotropic and nonhomogenous, different contact configurations might give different  $R_{xx}$  traces, which is indeed observed. Fig. 6.1 (b) displays the  $R_{xy}$  and  $R_{xx}$  traces of a different contact pair on the same sample. The difference in density is lower, roughly 2% ( $n_1 = 2.36 \times 10^{11} \text{ cm}^{-2}$ ,  $n_2 = 2.41 \times 10^{11} \text{ cm}^{-2}$ ), and the maximum  $R_{xx}$  values do not reach the quantization values. In the simplest case, a linear density gradient might be easily eliminated choosing the right contact configuration along the direction perpendicular to the gradient. We do not observe such a simple density gradient distribution in our samples.

Plateaus in  $R_{xx}$  have been previously observed in samples with spatially varying electron densities, either due to inhomogeneities in the wafer [145, 164, 165] or due to a constriction in which the density was different [166–168]. In an edge state picture [169], valid at fields above a few hundred millitesla, the two different densities can result in a sample with two different integer filling factor regions (i.e. integer filling factor  $\nu_1$  for the lower density region and integer  $\nu_2$  for the higher density region). This is schematically drawn in the inset of Fig. 6.1 (b). Combining this binary density edge state picture with the Landauer-Büttiker formalism [170], one can again reproduce the observed data. One can show that, if the innermost edge channel is returning to the other sample side between the two upper  $V_{xx}$  contacts,  $R_{xx}$  is quantized,

$$R_{xx} = \frac{h}{e^2} \left( \frac{1}{\nu_1} - \frac{1}{\nu_2} \right). \quad (6.1)$$

This is due to a voltage “jump”, due to the return of an edge channel between the two  $V_{xx}$  contacts. The measured quantized  $R_{xx}$  values are described by the above formula

within a few percent accuracy (see also inset of Fig. 6.3). Following the observation of plateaus in  $R_{xx}$  for fractional states next to reentrant states by *Pan et al.* [164], *Ilan et al.* could show with a classical model, that in presence of density gradients,  $R_{xx}$  on one sample side is given by the difference of the local Hall resistivities [171]. According to the model, as current is almost entirely flowing along this sample side, on the opposite sample side no voltage drops between the two contacts, thus  $V_{xx}$  is very small. This is consistent with the edge state picture depicted in the inset of Fig. 6.1 (b), where the return of one edge channel from the lower to the upper side of the sample is not noticed on the lower side voltage contacts. Thus  $R_{xx}$  stays in the zero resistance state. In the case of a linear, homogeneous density gradient the intrinsic  $\rho_{xx}$  might be reconstructed by combining  $R_{xx}$  measurements on opposite sample edges (or in opposite field polarity), see Eq. 20 in [171]. But due to the non-uniform density gradient in our samples this method is not applicable. Furthermore the density gradient is large, such that we are not able to measure  $R_{xx}$  in the opposite field direction, because it is becoming so small (see below).

### 6.2.3 Asymmetry in Magnetic Field

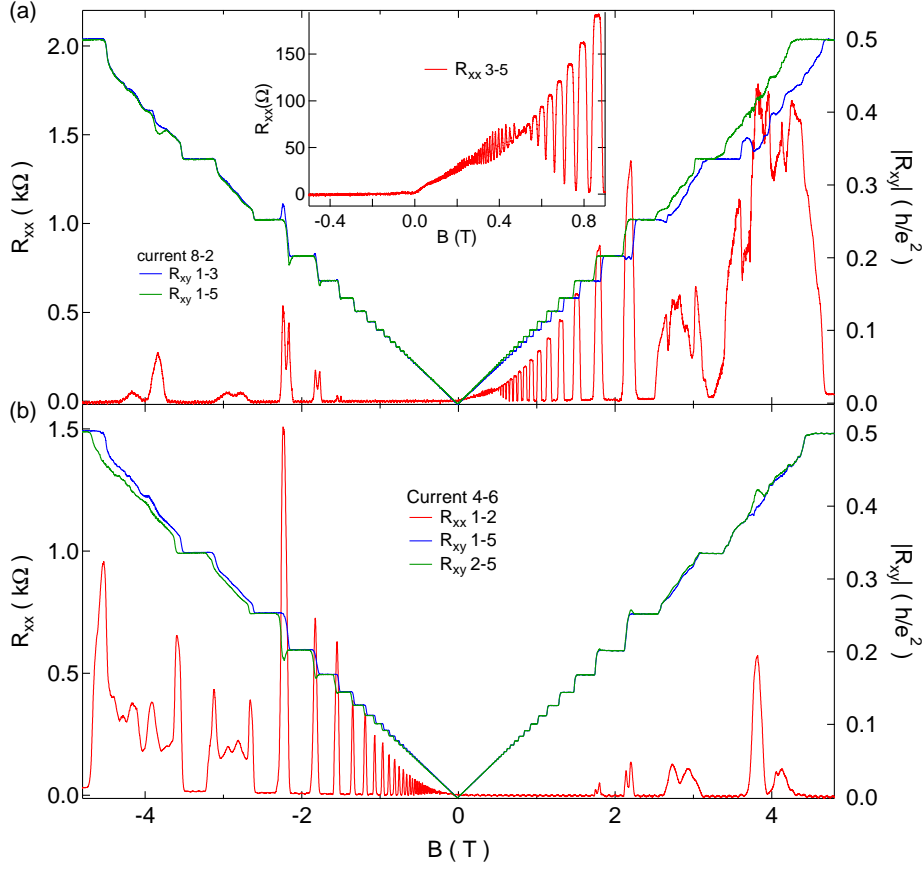


**Figure 6.2:** Asymmetry in  $B$ -field. (a)  $R_{xy}$  and  $R_{xx}$  versus  $B$  for both field polarities. The inset shows a zoom-in for  $R_{xx}$  around zero field. (b)  $R_{xy}$  and  $R_{xx}$  for a current and voltage configuration, which probes the opposite sample side, plotted against  $B$ .

The analog of switching to the other sample side is the inversion of the  $B$ -field polarity, as this changes the direction of current flow. Thus either changing the sample side, or changing the  $B$ -field polarity should result in a vanishing  $R_{xx}$ . Figure 6.2 (a) shows the same contact configuration as in Fig. 6.1 (a) but now for a wider field range and field inversion. One can clearly see the asymmetry upon  $B$ -field sign change. The inset in Fig. 6.2 (a) shows a zoom-in around zero field, making the asymmetry even more clear. At low negative  $B$ -field both  $R_{xy}$  traces lie on top of each other, thus  $R_{xx}$  stays at zero. At higher negative magnetic fields, overshoots and reentrant features can be observed, leading to a peak in  $R_{xx}$ . As suggested by *Pan et al.*, reentrant features could be viewed as an inversion of filling factors, being consistent with our observations [164].

A recent paper suggests co-existing evanescent incompressible strips as the origin for resistance overshoots [172], which we cannot explain with our model. Interestingly, the overshoots appear for the two different densities always on opposite sides of the QHE plateaus. In Fig. 6.2 (b) we plot a different contact configuration with  $V_{xx}$  contacts on the other sample side. The qualitative behavior of  $R_{xy}$  and  $R_{xx}$  is very similar, except for the inverted polarity for the  $B$ -field. Further the quantization in  $R_{xx}$  is not that clear, which indicates a lower density gradient. We propose the inversion of the  $B$ -field polarity as a detection tool for possible density gradients, as in homogeneous samples the two field sides should be perfectly symmetric. For not so dramatic density gradients ( $\leq 1\%$ ), Eq. 20 in [171] could help to reconstruct information about the intrinsic  $\rho_{xx}$  [145]. We further note that at the time inexplicable  $B$ -field asymmetry has been observed before [173], but has been interpreted as an anisotropic resistance state [174].

### 6.2.4 Temperature Dependence

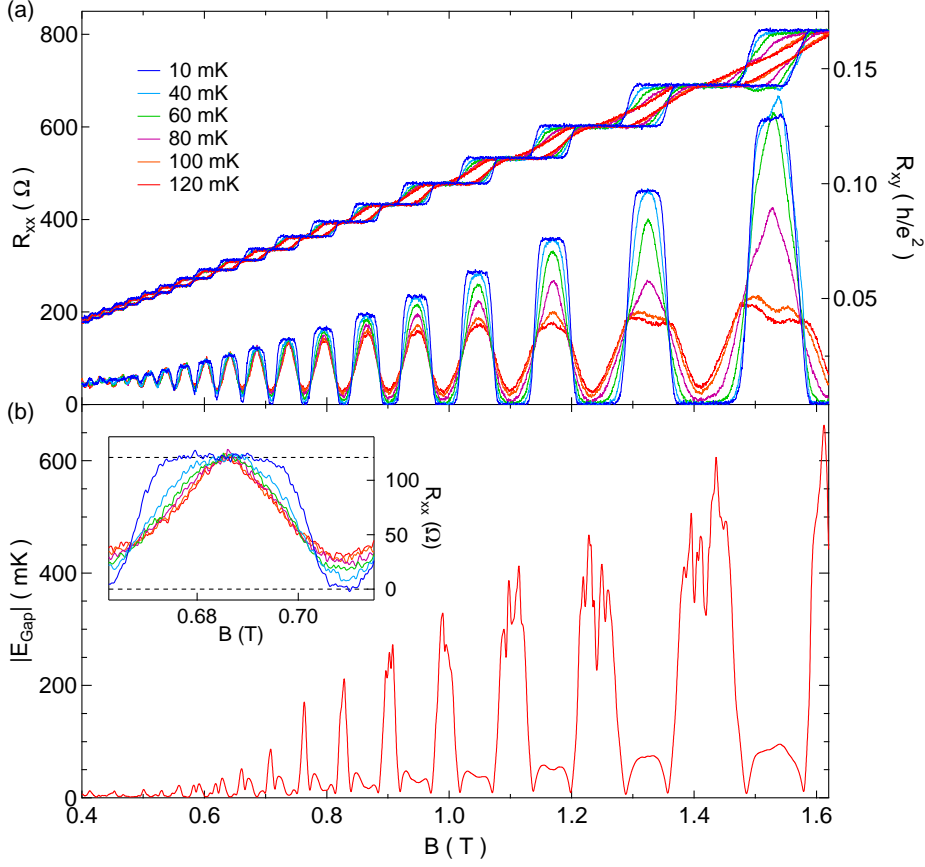


**Figure 6.3:** Temperature dependence. (a)  $R_{xy}$  and  $R_{xx}$  against magnetic field  $B$  for different temperatures  $T$ . (b) From the temperature dependence of  $R_{xx}(B, T)$  an energy gap is extracted and plotted against  $B$ , see text. The inset shows a zoom-in for the  $T$  dependent  $R_{xx}$  measurement. Dashed black lines indicate zero resistance line and expected value of quantized  $R_{xx}$  based on the binary gradient model.

In order to characterize the density gradient further, we measure the temperature dependence of the  $R_{xx}$  quantization. Figure 6.3 (a) plots both  $R_{xy}$  and  $R_{xx}$  against  $B$ -field for temperatures between 10 mK and 120 mK. Already at 40 mK the  $R_{xx}$  quantization is barely visible anymore. To quantify the temperature range where the effect of the density gradient can be observed, we introduce an energy gap  $E_{gap}$ . The gap is extracted by plotting the  $R_{xx}$  values for different temperature traces (zoom-in in Fig. 6.3 (b)) at a given  $B$ -field against inverse temperature in an Arrhenius plot. We extract  $E_{gap}$  with a linear fit to the natural logarithm of the resistance plotted

against the inverse temperature using  $\ln(R_{xx}) \propto \frac{E_{gap}}{2T}$ . For the  $R_{xx}$  quantization, the quantized resistance value is reduced by higher temperatures, whereas at  $R_{xx} = 0 \Omega$  the resistance increases at higher temperatures, which results in opposite slopes for the two cases. We therefore plot  $|E_{gap}|$  in Fig. 6.3 (b). One can clearly see that as the field is increased, the gap of the integer states also increases, which is expected. But the magnitude of the gap is much lower than expected, as at a  $B$ -field of 1 T, the cyclotron energy is on the order of 20 K. Generally, in high mobility samples the QHE plateaus starts only to develop well below 4 K [16, 145]. In our case the density gradient is reducing the gap even further, because of the effective smearing of the integer plateaus. The noise on  $|E_{gap}|$  values extracted around the  $R_{xx} = 0$  positions is due to the fact that it is impossible to characterize an energy gap which lies above 300 mK with a highest measured temperature of 120 mK. The energy gap of the  $R_{xx}$  quantization is even smaller, showing gaps on the order of few tens of mK. Therefore not only a high gradient, but also low electron temperatures are required to observe the quantization in  $R_{xx}$ .

### 6.2.5 $\nu = 5/2$ State Gap Characterization

Another important aspect of our findings is the influence of the gradient on the thoroughly investigated region between filling factors  $\nu = 3$  and  $\nu = 2$ . In the case of the high gradient contact configuration, the  $R_{xx}$  trace between 3.2 T and 4.8 T look very unstructured (Fig. 6.2 (a)) and not comparable to other high mobility samples used in typical  $\nu = 5/2$  studies [63]. On the other hand the lower gradient  $R_{xx}$  data (Fig 6.2 (b)) exhibits the typical minima for different fractional states, i.e. the  $\nu = 7/3$  and  $\nu = 8/3$  states. It has been established that for very high quality samples the fractional  $R_{xx}$  minima should drop to zero [63], indicating full condensation into the FQHE ground state. Typically the  $R_{xx}$  minimum value of a given fractional state is measured as a function of temperature. This is then used to extract the energy gap for the state under investigation. It has been reported that due to disorder or lack of

thermalization the minimal  $R_{xx}$  value saturates at higher temperatures than expected. We now find that the magnitude of the density gradient might influence the saturation temperature and thus distorts the extraction of the energy gap.

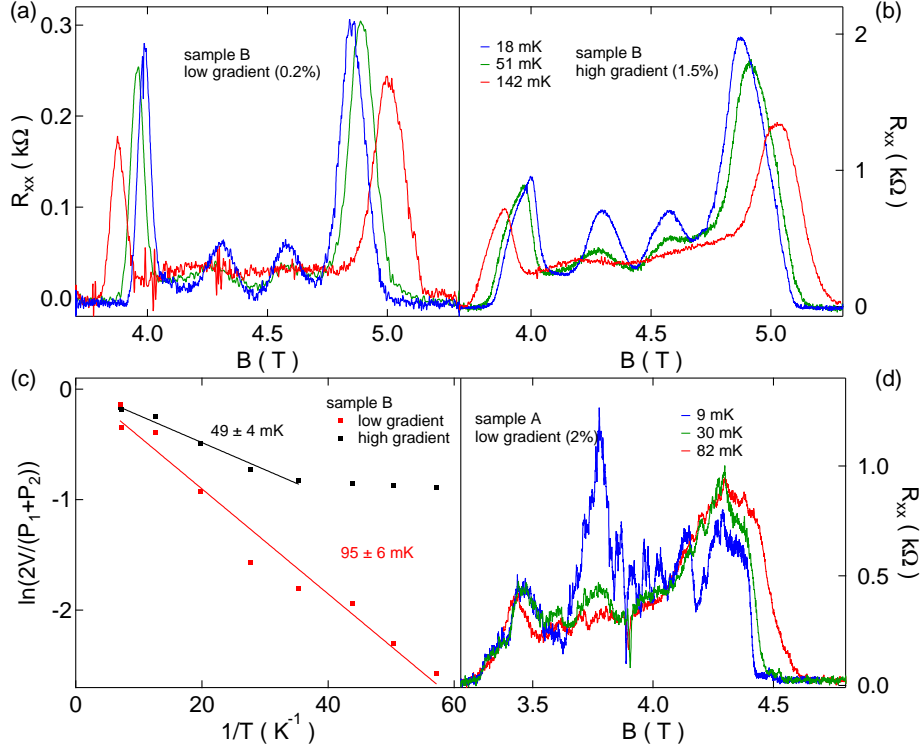


**Figure 6.4:** Density gradient influence on energy gap of the  $\nu = 5/2$  state. (a)  $R_{xx}$  between  $\nu = 3$  and  $\nu = 2$  at three different temperatures for the lowest density gradient contact configuration on sample B. (b)  $R_{xx}$  between  $\nu = 3$  and  $\nu = 2$  at three different temperatures for the highest density gradient contact configuration on sample B. (c) Arrhenius plot to extract the energy gap of the  $\nu = 5/2$  state for the high gradient (black) and the low gradient (red) configurations. Linear fits give the accordant energy gaps. (d)  $R_{xx}$  between  $\nu = 3$  and  $\nu = 2$  at three different temperatures for the lowest density gradient contact configuration on sample A.

Figure 6.4 presents data from sample B with an electron density of approximately  $3 \times 10^{11} \text{ cm}^{-2}$ , and a mobility of  $\sim 1.9 \times 10^7 \text{ cm}^2 \text{ V}^{-1} \text{ s}^{-1}$ . Sample B also exhibits a density gradient, but not as pronounced as sample A. Data for sample B is recorded at a frequency of 27.3 Hz in a different dilution fridge with a base  $T$  of 5 mK. An excitation of 1 nA was chosen in order to prevent heating of the electrons, especially for the sensitive  $\nu = 5/2$  gap measurement. Figure 6.4 (a) displays  $R_{xx}$  data between filling factors  $\nu = 3$  and  $\nu = 2$  for the lowest gradient contact pair (0.2%) for three



temperatures. As a comparison the highest gradient contact pair (1.5%) in sample B is plotted between  $\nu = 3$  and  $\nu = 2$  in Fig. 6.4 (b). One can immediately see that the amplitudes of the  $R_{xx}$  peaks are lower for the low gradient pair. Further the  $\nu = 5/2$  minima is lower for the lower gradient contacts. We then extract the energy gap of the  $\nu = 5/2$  for the different density gradients. As a measure of ground state population, we divide twice the depth of the minimum  $2V$  of  $R_{xx}$  by the averaged peak heights  $P_1$  and  $P_2$  flanking the minimum [92, 175]. In Fig. 6.4 (c) the Arrhenius plot for the two different contact configurations in Fig. 6.4 (a) and (b) are plotted. The low electron density gradient results in a nicely temperature dependent minimum, down to roughly 17 mK, whereas the high gradient data already saturates at 28 mK. In a very simple picture, the density differences in the sample lead to a smearing effect of signatures of intrinsic FQHE features. If the temperature broadening is smaller than the density smearing one only sees the effect of the density gradient, i.e.  $R_{xx}$  saturates at a temperature given by the density smearing. At higher temperatures the broadening due to temperature will be visible again, as observed in our data. Interestingly, the energy scale of the saturation is on the same order as the gaps of the  $R_{xx}$  quantization extracted by the temperature sweeps in Fig. 6.3 (b), and seems to be correlated to the gradient magnitude.

Interestingly, the extracted  $\Delta_{5/2}$  differ by a factor of 2 for the two contact configurations. The high gradient  $R_{xx}$  measurement results in a gap of approximately 50 mK. Note that we fit for the  $\Delta_{5/2}$  extraction  $\ln\left(\frac{2V}{(P_1+P_2)}\right) \propto \frac{\Delta_{5/2}}{2T}$ . On the same sample the low electron density gradient configuration yields  $\Delta_{5/2} \sim 100$  mK. For the low gradient contact configuration the density gradient is actually comparing to gradients observed in very high quality samples [164]. Therefore the saturation of the temperature dependence of  $\frac{2V}{(P_1+P_2)}$  (below 16 mK) and  $\Delta_{5/2}$  seem to be limited by disorder, rather than the density gradient. The low wafer quality makes it thus difficult to assign differences in gap size and temperature saturation only to the density gradient. In order to compare the two samples A and B Fig. 6.4 (d) plots the minimal gradient configuration

(2%) for sample A, where still no gap extraction was possible.

As a consequence of the density gradient defining  $R_{xx}$ , we observe that the amplitude of the  $R_{xx}$  peaks flanking the region between  $\nu = 2$  and  $\nu = 3$  correlates with the size of the density gradient (and thus indirectly with the gap size). The larger the gradient is, the higher the  $R_{xx}$  peaks are, the smaller is  $\Delta_{5/2}$ . Interestingly, a similar effect has recently been observed in the presence of alloy disorder [163]. For increased disorder, the high  $T$  value of  $R_{xx}$  at  $\nu = 5/2$  increases too. This has been attributed to enhanced scattering of composite fermions at the alloy disorder in the quantum well, which then limits the  $\nu = 5/2$  gap. Of course a density gradient does not cause increased scattering, but it seems that a high  $R_{xx}$  can result because of an additional energy scale (be it density gradient or disorder), which then limits the development of the  $\nu = 5/2$  state at the lowest temperatures.

### 6.3 Discussion

In summary, we have demonstrated that a density gradient in a 2DEG can lead to a longitudinal resistance  $R_{xx}$ , which is governed solely by the difference in local electron density between the two contacts, in extreme cases leading to quantization of  $R_{xx}$  in the integer regime. The quantized values are given by the difference of the reciprocal filling factors. As  $R_{xx}$  is given by local properties, different contact configurations result in different  $R_{xx}$  measurements. Based on previous experiments [145, 164, 165] and theory [171], a binary density model is introduced, which can explain the main features of our data. Upon inversion of the magnetic field or current direction, the  $R_{xx}$  traces are highly asymmetric, consistent with the prediction of the model. The temperature dependence of  $R_{xx}$  shows that even for the biggest density gradient the quantization is only visible at the lowest electron temperatures, showing energy gaps on the order of tens of millikelvin.

We emphasize that the  $R_{xx}$  quantization is only the manifestation of an extreme density gradient, but its influence should not be underestimated, especially as it is not always

easily detectable. We show that a significant density gradient can fundamentally flaw the  $\Delta_{5/2}$  extraction, because  $R_{xx}$  is not reflecting the intrinsic  $\rho_{xx}$  [164], which would carry the information about the ground state population of the  $\nu = 5/2$  state. Depending on the contact configuration,  $\Delta_{5/2}$  vary between 100 mK and 50 mK on the same wafer, apparently correlated with the density gradient. The temperature below which  $R_{xx}$  at  $\nu = 5/2$  saturates also seems to be related to the gradient. We speculate that the saturation comes about because of a smearing effect due to the density differences. This highlights the importance of the density gradient and its detrimental effect on characterizing wafer quality through  $R_{xx}$ . Although we cannot rule out some other energy scale like disorder limiting both  $\Delta_{5/2}$  and the saturation temperature, it is peculiar how nicely the density gradient and  $\nu = 5/2$  are correlated. Of course establishing a clear influence of the density gradient on the  $\nu = 5/2$  features calls for further experiments.

Generally, it is not clear to us, how previous experiments could have been affected by the effect of a gradient, although we believe that better wafers did not suffer from this problem, or only slightly. Anyway the asymmetry in  $B$ -field could be a nice tool to check for density gradient effects. We further suggest that in order to determine  $\Delta_{5/2}$ , future experiments should focus not on  $R_{xx}$  (or only after thoroughly investigating it), but rather on  $R_{xy}$ . For example the field range over which  $R_{xy}$  is quantized at  $\frac{2h}{5e^2}$  as a function of temperature could serve as an indication for the strength of the gap.

It is very likely that rotation during wafer growth, as the standard procedure is, will suppress the density gradient. But probably rotation can also not avoid the density gradient completely, due to different locations of the MBE targets within the vacuum chamber. Another approach to overcome the limitation of different densities across the wafer could be a reduction of contact to contact distances. The density difference between the contacts then might be smaller and the effect less dramatic. Further this could enable more detailed and controlled studies on how the  $\nu = 5/2$  characterization is influenced by the density gradient.

## 7 Evidence for Disorder Induced Delocalization in Graphite

L. Casparis, D. Hug, D. Koelbl, D. M. Zumbühl

*Department of Physics, University of Basel, CH-4056 Basel, Switzerland*

A. Fuhrer

*IBM Research, Zürich Research Laboratory, Säumerstrasse 4, CH-8803 Rüschlikon, Switzerland*

### Abstract

We present electrical transport measurements in natural graphite and highly ordered pyrolytic graphite (HOPG), comparing macroscopic samples with exfoliated, nanofabricated specimens of nanometer thickness. The latter exhibit a very large *c*-axis resistivity  $\rho_c$  – much larger than expected from simple band theory – and non-monotonic temperature dependence, similar to macroscopic HOPG, but in stark contrast to macroscopic natural graphite. A recent model of disorder-induced delocalization is consistent with our transport data. Furthermore, Micro-Raman spectroscopy reveals clearly reduced disorder in exfoliated samples and HOPG, as expected within the model – therefore presenting further evidence for a conceptual novelty in electronic transport in graphite.

This chapter is prepared for publication.

## 7.1 Introduction

Graphite is a paradigmatic layered material and has been investigated intensively for many decades. The in-plane resistivity  $\rho_{ab}$  is rather well described by a simple Drude model. However, the resistivity  $\rho_c$  along the  $c$ -axis, perpendicular to the graphite basal planes, as well as its temperature dependence  $\rho_c(T)$ , are not described by the simple band structure model [176, 177], and currently lack theoretical understanding despite extended efforts. The resistive anisotropy  $R_A = \rho_c/\rho_{ab}$  is a convenient dimensionless parameter characterizing transport properties.

Carbon atoms in the graphite basal planes are strongly bound by covalent bonds, while much weaker Van der Waals forces bind the graphene sheets along the  $c$ -axis. Non-trivial disorder such as stacking faults and crystalline grains result in a mosaic angle and complicate electronic transport. For isotropic disorder, simple band theory [176] predicts  $R_A = m_c/m_{ab} \sim 140$ , the ratio of the corresponding band masses. This agrees well with measurements in natural graphite (NG) [178, 179]. In highly oriented pyrolytic graphite (HOPG), the anisotropy was found to be much larger, even exceeding 10'000 in some experiments [180, 181]. Moreover, band theory [176] predicts a monotonic metallic temperature dependence for both  $\rho_{ab}$  and  $\rho_c$ , resulting in a temperature independent anisotropy  $R_A$ . This is seen in NG [182], but not in HOPG, where  $\rho_c$  is non-monotonic with a maximum around 40 K [180, 181, 183], similar to  $\rho_c$  in other layered materials, such as  $\text{NaCo}_2\text{O}_4$  [184] and Cuprates [185]. A large anisotropy far exceeding 100 combined with the non-metallic temperature dependence – together referred to as anomalous behavior – are currently not understood and present a fundamental problem in condensed matter physics [182, 186, 187].

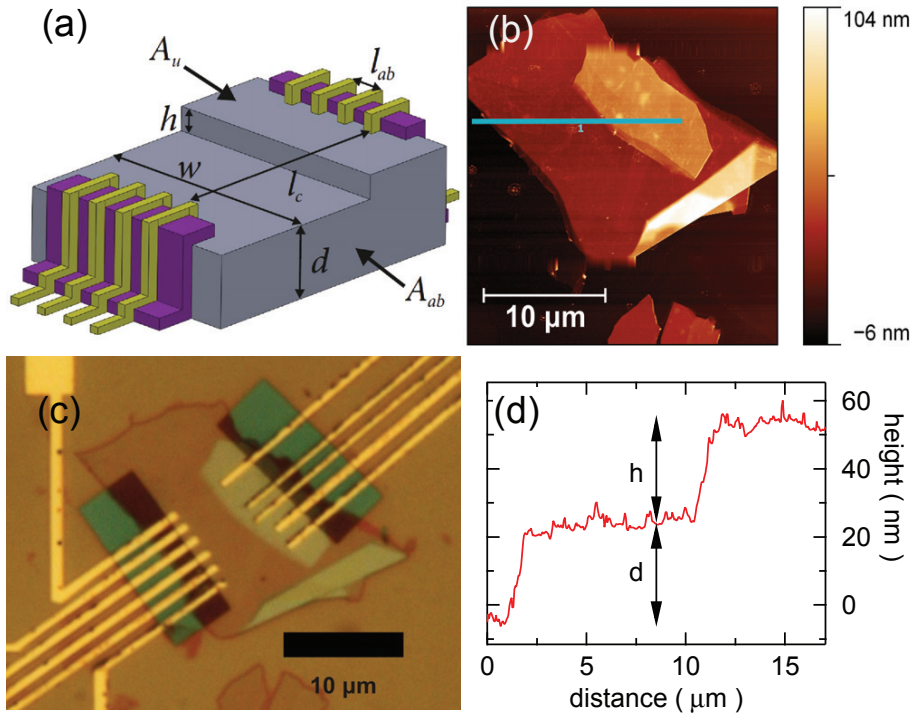


**Figure 7.1:** Nano-graphite samples. (a) Device schematic. Ti/Au contacts (yellow) for 4-wire measurements are patterned on each plateau, isolated from the graphite walls by a  $SiO_2$  layer (purple). AFM picture (b) and optical microscope image (c) of an HOPG flake with two plateaus. (d) Cross section along the blue line in (b), giving plateau heights.

### 7.1.1 Overview

In this Letter, we for the first time use exfoliation and nano-fabrication techniques to investigate both  $\rho_{ab}$  and  $\rho_c$  (see Fig. 7.1) in graphite flakes of various thickness in the nanometer range. Remarkably, we find in all types of graphite anomalous behavior – namely a large resistive anisotropy as well as a non-metallic temperature dependence. Previous experiments measure  $\rho_{ab}$  only [188]. This permits a comparison of  $R_A$  in samples with thicknesses in the nanometer range with macroscopic samples. The in-plane resistivity of all samples is in good agreement with reported values [178–180], and shows no size-dependence. Therefore the large  $R_A$  in the anomalous samples are to be attributed to a large  $\rho_c$ . The measured anisotropies appear consistent with a recent model based on disorder induced delocalization by *Maslov et al.* [189, 190], further corroborated by a disorder characterization of our samples using micro-Raman

spectroscopy. Conduction path mixing due to a finite mosaic angle can account for the non-monotonic temperature dependence [191], altogether presenting first experimental evidence for a novel paradigm of electrical transport in graphite.

## 7.2 Experimental Techniques

### 7.2.1 Sample Fabrication

To produce nanostep samples, we use the design shown in Fig. 7.1(a). We exfoliate graphite onto a Si wafer with a 300 nm thick thermal oxide and identify suitable flakes with two plateaus differing in height by optical microscopy. The lower plateau height  $d$  and the step height  $h$  are determined from AFM images [see Fig. 7.1(b,d)], giving heights between 14 and 150 nm. To extend the range to larger step heights, we use e-beam lithography and oxygen-plasma etching to carve steps up to  $h = 450$  nm.

For contacting the plateaus, we first cover parts of the exterior edges of both plateaus with SiO<sub>2</sub> of at least 80 nm thickness [192] in order to prevent short-circuiting the  $c$ -axis. Contacts (typically a few hundred nanometers in width) and bonding pads are patterned in a final e-beam step, evaporating a Ti/Au layer thicker than 110 nm (SiO<sub>2</sub> thickness plus 30 nm). A typical device is shown in Fig. 7.1(c). All resistances are measured with standard 4-wire lock-in techniques. This layout allows measurements of both  $\rho_{ab}$  and  $\rho_c$  on the same device, as needed to obtain the anisotropy. However, due to variations in the current distribution related to the individual device geometries, corrections to the measured resistances must be applied. We do this by means of a rough estimate based on the simplified geometry shown in Fig. 7.1(a). On the other hand, we also performed more elaborate numerical calculations of the current distribution to verify the observed effects, see supplementary information section.

### 7.2.2 Measurements

The in-plane resistivity  $\rho_{ab} = R_{ab}A_{ab}/l_{ab}$  is estimated from the 4-wire resistance  $R_{ab}$  with current and voltage probes on the same plateau and assuming a simple rectangular shape of the graphite sample, with voltage probe distance  $l_{ab}$  and total graphite cross section  $A_{ab}$  [see Fig. 7.1(a)]. This is a good approximation for thin, elongated samples and small anisotropy and evenly distributed contacts. For realistic devices as the one shown in Fig. 7.1(b)+(c) and for large anisotropy, the extracted  $\rho_{ab}$  presents an upper bound. Since the current cannot penetrate easily along the highly resistive c-axis and it's in-plane distribution is not homogeneous between the current contacts, the effective conduction channel is thinner and narrower than our estimate. The  $\rho_{ab}$  extracted here (see Fig. 7.2 and Table I in the supplementary information section) agree rather well with literature [178–180, 193]. Moreover,  $\rho_{ab}$  appears independent of the graphite thickness and is similar for NG (from two different sources, Indian NG and Madagascar NG) and HOPG samples, as seen in Fig. 7.2, open symbols.

Next, we determine the c-axis resistivity  $\rho_c$ . Since  $l_c$ , the contact to contact distance across the step, is much larger than the step height  $h$  (see Fig. 7.1(a)), we need to subtract the in-plane contributions to the measured resistance  $R_c$  to obtain the actual c-axis resistance  $\widehat{R}_c$  using

$$\widehat{R}_c = R_c - \rho_{ab} \cdot \left( \frac{l_{cl}}{w_l \cdot d} + \frac{l_{cu}}{w_u \cdot (d + h)} \right), \quad (7.1)$$

with upper/lower contact to step distance  $l_{cl}/l_{cu}$  and corresponding plateau widths  $w_l/w_u$ .  $\rho_c$  is then obtained from  $\rho_c = \widehat{R}_c A_u / h$ , where  $A_u$  is the upper plateau area. Depending on the sample geometry, the in-plane correction can be a large fraction of  $R_c$ , see supplementary information for an overview. We note that as previously for  $\rho_{ab}$ , we again overestimate the thickness  $d$  for large anisotropy. However, here, this tends to effectively cancel the overestimated  $\rho_{ab}$ , making the extracted  $\rho_c$  quite robust.



## 7.3 Results

### 7.3.1 Thickness Dependence

Figure 7.2 displays the resulting  $\rho_c$  as a function of height (filled symbols), giving very large  $\rho_c$  and correspondingly large anisotropy  $R_A$  for all nano-graphites, both NG and HOPG. A power-law fit (linear fit on the log-log graph, slope  $-1 \pm 0.4$ ) through all NG nanostep  $\rho_c$  data points seems to indicate a trend of reduction of  $\rho_c$  with increasing step height towards the macroscopic  $\rho_c$  value in NG samples. HOPG nanostep data is excluded from the fit, since HOPG has no apparent size dependence when going from macroscopic to nanostep samples (filled red diamonds). In order to make a stronger statement, samples with step heights between  $1 \mu\text{m}$  and  $100 \mu\text{m}$  might give more insight [194].

In order to test for the validity of the in-plane correction of Eq. 7.1, we numerically calculate the current distribution for the various contact and sample geometries, taking into account the anisotropy. From a simultaneous fit of the two measurements of  $R_{ab}$  and  $R_c$  to the calculated resistances we can extract  $\rho_{ab}$ ,  $\rho_c$  and  $R_A$ , see the supplementary information. As anticipated the simulated  $\rho_{ab}$  are lower than the approximated  $\rho_{ab}$ . For both methods the  $\rho_c$  values agree well with each other, corroborating our approach.

To allow a comparison with previous experiments, we also investigate macroscopic NG and HOPG samples, again measuring both  $\rho_{ab}$  and  $\rho_c$ . Due to the geometry used, corrections due to a spreading of the current flow are small and not necessary for the macroscopic samples. On the other hand, the overestimation of the sample thickness due to a large anisotropy is still present. The values obtained are also added to Fig. 7.2, together with typical values from literature [178–180]. We find decent agreement between our macroscopic data and previous measurements, reproducing here again the large discrepancy in  $\rho_c$  between HOPG and NG in macroscopic samples.

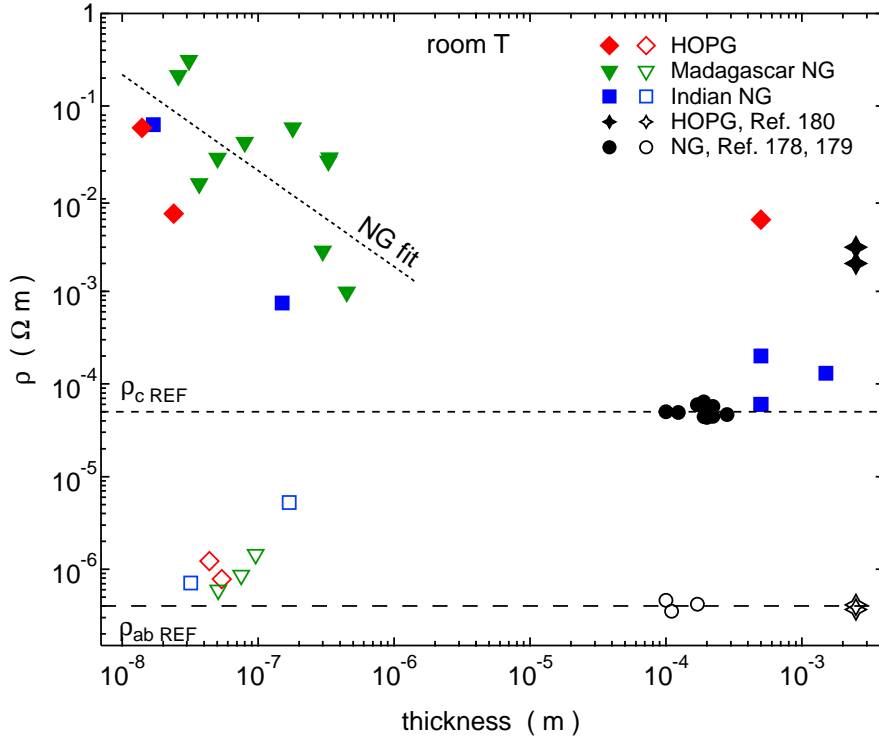


**Figure 7.2:** Influence of graphite thickness on  $\rho_c$  (solid markers) and  $\rho_{ab}$  (empty markers) at room temperature, comparing HOPG (red) with Madagascar NG (green) and Indian NG (blue). For  $\rho_{ab}$ , the abscissa value used is  $d + h$ , the overall flake thickness, see Table I in the supplementary information section. Previous measurements of macroscopic samples (black) were added for both HOPG [180] (stars) and NG [178, 179] (circles) for comparison. Dashed horizontal lines indicate literature values  $\rho_{ab, \text{REF}}$  for  $\rho_{ab}$  and  $\rho_{c, \text{REF}}$  for  $\rho_c$ . Further, the best power-law fit to all NG nanostep data yields an exponent of  $-1.0 \pm 0.4$  and is shown by a dotted line to indicate a potential trend, see text.

### 7.3.2 Temperature Dependence

Next, we turn to the temperature dependence  $\rho_c(T)$  of the macroscopic samples [195]. For HOPG, we find a non-metallic  $\rho_c$  at high  $T$  ( $d\rho_c/dT < 0$ ), see Fig. 7.3 (a). Around 40 K,  $\rho_c$  displays a rather shallow maximum, in good agreement with previous HOPG measurements [180]. In contrast, macroscopic Indian NG behaves weakly metallic and monotonic down to 4 K [see Fig. 7.3 (b)], also in agreement with previous NG data [178]. Overall, our data from macroscopic samples fully agrees with the literature, giving us confidence that a comparison of the exfoliated samples with literature is appropriate.

The temperature dependence of the exfoliated nano-graphite samples are shown in

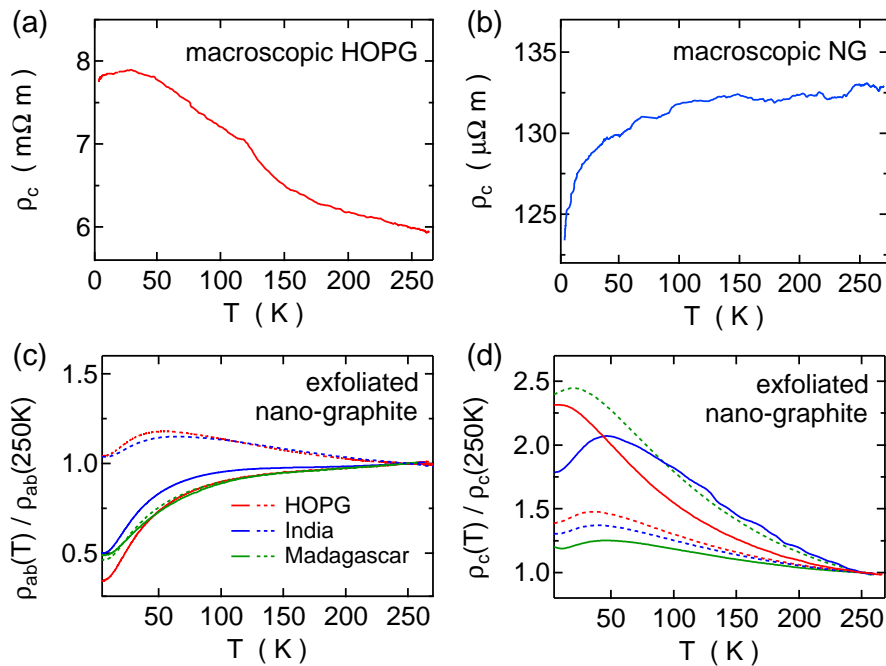


**Figure 7.3:** Temperature dependence of resistivities.  $\rho_c(T)$  in macroscopic HOPG (a) and macroscopic Indian (b) NG. (c)  $\rho_{ab}(T)$  in nanoscale samples for HOPG (red) and NG India (blue) and Madagascar (green). Two samples are presented for each graphite type (solid, sample 1; dashed, sample 2). For numerical values see Table I in the supplementary information section. (d)  $\rho_c(T)$  for the same samples.

Fig. 7.3 (c) and (d), normalized to the high- $T$  value. In most samples,  $\rho_{ab}(T)$  is metallic and monotonous, as expected, and in agreement with macroscopic data [178, 196]. In two specimens,  $\rho_{ab}$  exhibits a shallow maximum. This seems to occur occasionally in nanoscale samples, as previously reported [188, 197]. Remarkably,  $\rho_c(T)$  of all nanostep samples is qualitatively the same, showing a non-metallic and non-monotonic temperature dependence, qualitatively identical to macroscopic HOPG, and clearly different from the macroscopic NG data. We emphasize that the non-metallic  $\rho_c(T)$  combined with the large anisotropy  $R_A$  constitutes anomalous behavior for all nanoscale samples. In contrast, only macroscopic HOPG is anomalous, not macroscopic NG.

## 7.4 Discussion

### 7.4.1 Disorder induced Delocalization

Motivated by an anisotropy far exceeding the band structure expectation, we consider a recent theory by Maslov et al. [189]. A similar effect was also previously observed for photons [190]. Within this theory, c-axis transport is strongly suppressed in samples with weak bulk disorder due to 1D Anderson localization along the c-axis induced by randomly spaced barriers (e.g. stacking faults). This gives a very large  $\rho_c$  and anisotropy  $R_A$ , in absence of strong bulk disorder. However, c-axis localization is destroyed by bulk scattering out of the c-axis direction, leading to reduced  $\rho_c$  and smaller  $R_A$ . Interestingly, here, disorder can *suppress* Anderson localization, rather than enhancing it, as is usually the case.

Therefore, HOPG and nanostep samples are expected to have weak bulk disorder. In contrast macroscopic NG specimens either have significantly more bulk disorder (suppressing c-axis localization), or fewer c-axis barriers, insufficient for localization (barriers spacing exceeding coherence length).

To characterize disorder, we measure spatially resolved micro-Raman spectra, see Fig. 7.4. The penetration depth of the probing laser ( $\lambda=532$  nm) into graphite is roughly 50 nm [198]. For the presented sample dimensions micro-Raman thus allows for a bulk investigation of disorder, remarkably in exactly the samples studied by transport measurements.

Graphitic bulk disorder such as dislocations and impurities appear as a D-peak in Raman spectra of graphite, whereas planar stacking faults and mosaic angles cannot be detected. We plot  $\xi = I_D/I_G$ , the ratio of the G-peak intensity  $I_G$  and D-peak intensity  $I_D$  after background subtraction, obtaining an intensity independent characterization of disorder. For graphite,  $0 \leq \xi \lesssim 1$ . Due to a finite integration time,  $\xi$  has measurement noise of  $\sim 1/50$ , i.e.  $\xi \lesssim 1/50$  indicates an invisible D-peak and weak disorder. A large  $\xi$  indicates a high degree of disorder (large  $I_D$ ).

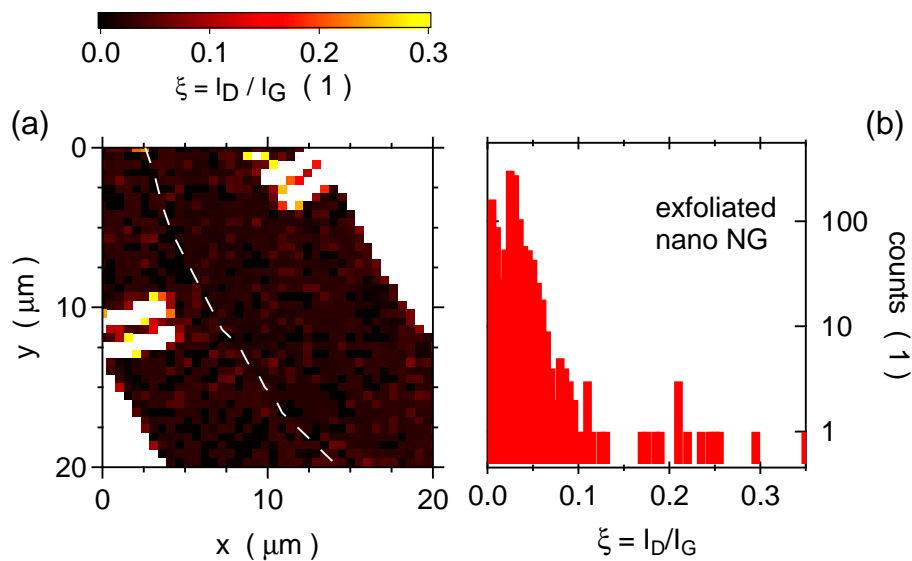


**Figure 7.4:** Disorder characterization with micro-Raman spectroscopy. (a) Ratio  $\xi = I_D/I_G$  of the D-peak and the G-peak intensities, scanned (resolution  $\sim 0.5 \mu\text{m}$ ) on a 50 nm thick, exfoliated Madagascar NG flake. White is off the graphite flake or on metal contacts. The white dashed line indicates the location of the step between upper and lower plateau. (b) Histogram of  $\xi$  for the corresponding scan area.

Exfoliated Madagascar NG flakes display very low disorder, see Fig. 7.4(a) for a typical scan (Madagascar 3). The location of the step between the two plateaus is indicated by the white dashed line, but remains invisible in  $\xi$ . A histogram of  $\xi$  is displayed in Fig. 7.4(b) further demonstrating the weak disorder. Several other exfoliated NG and HOPG samples are inspected, all exhibiting similar distributions in  $\xi$ , indicating very low disorder, consistent with expectations from the model.

We note that on the surface of pristine, macroscopic Madagascar NG samples disorder tends to be large ( $\xi \sim 1/3$ ). Exfoliating macroscopic NG only once already results in strongly reduced surface disorder probed as by Raman spectroscopy. However we emphasize that a  $\rho_c$  measurement of a one time exfoliated macroscopic NG sample does not result in high  $\rho_c$ .

Clearly, exfoliating somehow exposes clean surfaces [199] and after repeating many times possibly removes bulk disorder, though the mechanism is not clear. This could potentially explain the size dependence mentioned in Fig. 7.2: thinner samples tend to

require more exfoliation steps, therefore becoming cleaner, more localized, and obtaining a larger  $\rho_c$ . Ultimately, for sufficiently small  $h$ , 1D localization should break down and  $\rho_c$  decrease strongly – not visible in the present data, presumably because  $h$  is still too large. Overall, the Raman data is consistent with the predictions of the model, namely weak disorder in all exfoliated samples.

#### 7.4.2 Non-monotonic Temperature Dependence

Finally, we turn to the anomalous temperature dependence of  $\rho_c$ . If the c-axis resistivity  $\rho_c$  is very large, the c-axis conductance path could easily be mixed with the ab-conductivity  $\sigma_{ab}$  due to the finite mosaic angle  $\theta$ , effectively short circuiting the intrinsic c-axis conductivity  $\sigma_c$ . Assuming small tilting  $\theta \ll 1$ , the measured conductivity  $\widetilde{\sigma}_c$  can be written as [191]

$$\widetilde{\sigma}_c(T) = \sigma_c(T) + \langle \theta^2 \rangle \cdot \sigma_{ab}(T), \quad (7.2)$$

where  $\langle \theta^2 \rangle$  is the variance of  $\theta$ . In low bulk-disorder samples at low temperatures, the intrinsic  $\sigma_c$  is very small (strongly localized) and  $\widetilde{\sigma}_c(T)$  obtains a significant component from  $\sigma_{ab}$ , including the (weakly) metallic temperature dependence  $\sigma_{ab}(T)$ , leading to a slight increase of  $\rho_c(T)$  upon increasing  $T$ . At higher  $T$ , localization is weakened (due to phonon scattering, equivalent to increasing bulk disorder for increasing  $T$ ),  $\sigma_c$  is enhanced and becomes increasingly more dominant, leading to a decreasing  $\rho_c$  above some cross-over  $T$ . For both HOPG and NG graphite we measure a mosaic angle between  $0.2^\circ$  and  $2^\circ$  (not shown), which is in agreement with the mixing mechanism, as a mosaic angle of about  $0.8^\circ$  corresponds to a cross-over  $T$  of 40 K. For disordered samples, on the other hand, the intrinsic  $\sigma_c$  is dominating  $\widetilde{\sigma}_c(T)$  since localization is already lifted by disorder, resulting in the usual metallic temperature dependence, as seen in macroscopic NG [182].

## 7.5 Conclusion

In conclusion, we observe anomalous behavior, namely high  $\rho_c$  and non-monotonic  $\rho_c(T)$ , in both NG and HOPG exfoliated samples. This is in stark contrast to macroscopic samples, where the anomalous behavior is only seen in HOPG, consistent with previous experiments. A recently proposed transport theory [189] can consistently explain this convergence on the nanoscale, the macroscopic data, and the temperature dependence. Furthermore, it is consistent with our finding of low disorder in exfoliated and HOPG samples, and high disorder in macroscopic NG. We note additionally that neutron irradiation experiments [180, 186] inducing bulk disorder also give consistent results, namely reduced  $\rho_c$  after irradiation of HOPG, further corroborating the model. We therefore present first, clear evidence of disorder induced delocalization, a conceptual novelty, as a new paradigm of electronic transport in graphite.

Though beyond the scope of the present work, it would be very interesting to subject the model to further scrutiny: studying intermediate steps filling the thickness gap in Fig. 7.2, but also even smaller thicknesses, ultimately down to few- or bi-layer graphene, potentially revealing the localization length. This might be facilitated by bottom contacts with layers deposited on top, followed by top contacts. We note that the minimum thickness in the present samples is 14 nm, corresponding to about 50 graphene layers. Further, a characterization of graphite disorder would be of great interest, e.g. investigating stacking faults and angles, intercalation, grain and boundary formation [200], aiming at identifying the localization mechanism, leading ultimately to a microscopic understanding of electrical transport in graphite. The results presented here were obtained in graphite, but it would be intriguing to learn if similar arguments apply to some of the numerous other layered materials.

## 7.6 Supplementary Information

In this supplementary section we present detailed information about the geometry of all samples and the transport measurements on these samples. Further we describe the method we applied for determining the current distribution in our samples. The results from these numerical calculations are then compared to the approximative method used in the main text.

### 7.6.1 Geometry of Nano Graphite Flakes

Table 1,2 and 3 summarize all sample geometries of the nano graphite devices shown in Fig.7.2 of the main text. For Madagascar Samples 4-9 no  $\rho_{ab}$  measurement was possible because no suitable contacts were available. Despite the missing separate  $\rho_{ab}$  measurement on those samples, we nevertheless correct for the in-plane contribution to  $R_c$ . We use  $\rho_{ab} = 0.8 \mu\Omega m$  as a fixed value and show values derived from this in parenthesis. Sample numbers 1 and 2 of every type of graphite are also included in Fig.3 of the main text showing the temperature dependence. The solid (dashed) lines in this figure correspond to sample numbers 1 (2), respectively.

Table 1: Nano-sample parameters for the determination of  $\rho_{ab}$ , see main text for definitions, and Fig.1 therein for an illustration. Samples listed here are represented in Figs.2 and 3. Fig.3 shows the temperature dependence for samples 1 and 2 of each specimen.

Material	$R_{ab}$ ( $\Omega$ )	$A_{ab}$ ( $\mu m^2$ )	$l_{ab}$ ( $\mu m$ )	$\rho_{ab}$ ( $\mu\Omega m$ )
HOPG 1	3.8	0.8	2.5	1.2
HOPG 2	5.6	0.45	3.3	0.8
India 1	18.9	0.25	7	0.7
India 2	67	0.8	10	5.3
Madagascar 1	7.6	1.5	8	1.5
Madagascar 2	11.8	0.3	6	0.6
Madagascar 3	9.1	0.8	8	0.9



Table 2: Nano-sample parameters for the correction of  $R_c$ , see main text for definitions, and Fig. 1 therein for an illustration. Samples listed here are represented in Figs. 2 and 3. Fig. 3 shows temperature dependence for samples 1 and 2 of each specimen. For samples where no  $\rho_{ab}$  measurement was possible, values derived from a typical  $\rho_{ab}=0.8\mu\Omega m$  are shown in parenthesis.

Material	$R_c(\Omega)$	$l_{cl}(\mu m)$	$w_l(\mu m)$	$l_{cu}(\mu m)$	$w_u(\mu m)$	$d(nm)$	$h(nm)$	$\widehat{R}_c(\Omega)$
HOPG 1	12	4	25	2.5	25	30	14	2.3
HOPG 2	12	6	20	2	20	30	24	2.9
India 1	19	1	20	3	20	15	17	11
India 2	37	2.4	20	2	15	20	150	1.3
Mada 1	27	1.2	10	2.3	10	16	80	13
Mada 2	26	4.2	8	3.3	5	14	37	5.6
Mada 3	31	2.5	15	2	22	44	31	21
Mada 4	68	6.5	26	2	20	10	26	(28)
Mada 5	26	7	18	1	18	21	50	(11)
Mada 6	100	2.6	16	2	12	20	330	(88)
Mada 7	16	5.5	9	5.5	9	150	300	(8.5)
Mada 8	9	4	15	6.2	8.5	100	450	(3.2)
Mada 9	104	1	12	4.5	11	65	335	(101)

### 7.6.2 Numerical Simulation of Current Distribution

The approximative method which is used to extract  $\rho_{ab}$ ,  $\rho_c$  and ultimately  $R_A$ , includes several simplifications. In order to improve the extraction of these parameters, we numerically simulate the current flow for our sample geometries. The simulation allows us to determine  $\rho_{ab}$  taking into account the effectively reduced current carrying cross-section due to the point like contact geometries. Further, we can include the resistivity anisotropy in the simulation, enabling an estimate for the concentration of the current flow in the layers closest to the contacts, which again improves the determination of  $\rho_{ab}$ ,  $\rho_c$  and  $R_A$ .

Combining Ohm's law and the continuity equation gives:

$$0 = \dot{\rho} = \sigma \Delta \Phi \quad (7.3)$$

Table 3: Nano-sample parameters, see main text for definitions, and Fig. 7.1 therein for an illustration. Samples listed here are represented in Figs. 7.2 and 7.3. Fig. 7.3 shows temperature dependence for samples 1 and 2 of each specimen. Values derived from an average  $\rho_{ab} = 0.8 \mu\Omega m$  are shown in parenthesis.

Material	$\widehat{R}_c(\Omega)$	$h(nm)$	$A_u(\mu m^2)$	$\rho_c(m\Omega m)$	$R_A$
HOPG 1	2.3	14	361	58	48k
HOPG 2	2.9	24	57	6.9	8.8k
India 1	11	17	100	63	89k
India 2	1.3	150	88	0.78	140
Mada 1	13	80	248	41	28k
Mada 2	5.6	37	95	15	24k
Mada 3	21	31	458	311	360k
Mada 4	(28)	26	200	(213)	(266k)
Mada 5	(11)	50	127	(28)	(35k)
Mada 6	(88)	330	92	(25)	(31k)
Mada 7	(8.5)	300	96	(2.7)	(3.4k)
Mada 8	(3.2)	450	140	(1)	(1.35k)
Mada 9	(101)	335	96	(28)	(35k)

where we have assumed that sigma is a spatially constant tensor of the form:

$$\sigma = \begin{pmatrix} \sigma_{ab} & 0 & 0 \\ 0 & \sigma_{ab} & 0 \\ 0 & 0 & \sigma_c \end{pmatrix} \quad (7.4)$$

In order to solve equation (7.3) we map our samples to a rectangular, evenly spaced, grid. The typical grid spacing ( $da, db, dc$ ) in the  $a$ - and  $b$ -direction is on the order of microns. For the  $c$ -direction a grid spacing of 0.5 nm is used. By rewriting the three dimensional grid as a vector, we reduce the calculation to the solution of a system of linear equations, which can be written in matrix form and subsequently solved using standard procedures i.e. Gaussian elimination.

The boundary conditions are chosen such that no current flows perpendicular to the sample boundary except at the contacts. This means  $E_{\perp} = -\nabla\Phi_{\perp}=0$  at the sample boundary where there are no contact pads. On the contact pads  $E_{\perp} = -\nabla\Phi_{\perp}=\text{const}$  and the bias current is evenly distributed over the contact-sample interface.

The fitting of the measured values is performed as follows: First, from the device and contact geometry of the  $R_{ab}$  measurement, the corresponding  $\rho_{ab}^{sim}$  is calculated as a function of the anisotropy ratio  $R_A$ . In a second step, taking into account the used contact geometry, the measured c-axis resistance  $R_c$  is simulated as a function of  $R_A$ . To calculate  $R_c$ , we assume the sample to consists of two cuboids sitting on top of each other and split the calculation into two steps. The current is injected from a metal contact into the first cuboid and drained on the entire interface area of the two cuboids. For the second cuboid, the current is injected at the interface area and drained on a metal contact. We find that reducing the area where current flows from one cuboid into the other does not change our results by more than a few percent, validating the assumption of a homogenous current flow at the interface between the cuboids.

By matching the simulated  $R_c(R_A)$  to the measured value  $R_c$ , we find  $R_A^{sim}$ . Together with the first calculation step this determines  $\rho_{ab}^{sim}$ . Knowing  $\rho_{ab}^{sim}$  and  $R_A^{sim}$ , we calculate  $\rho_c^{sim}$ .

Table 4 compares the results obtained through the approximative method with the ones extracted from the numerical calculation. For the samples where a  $R_{ab}$  measurement was not possible, we fixed  $\rho_{ab}^{sim} = 50 \text{ n}\Omega\text{m}$ , in order to calculate  $\rho_c^{sim}$ . These values are again given in parenthesis. For two samples the numerical calculation did not converge, these values are omitted in Table 4. The reason for the divergence in this two cases could be that  $\rho_{ab}$  is actually lower than the fixed  $\rho_{ab}^{sim}$ . By lowering the fixed  $\rho_{ab}^{sim}$  the simulation converges, but we omit these points, because  $R_A$  then highly depends on the fixed parameter.

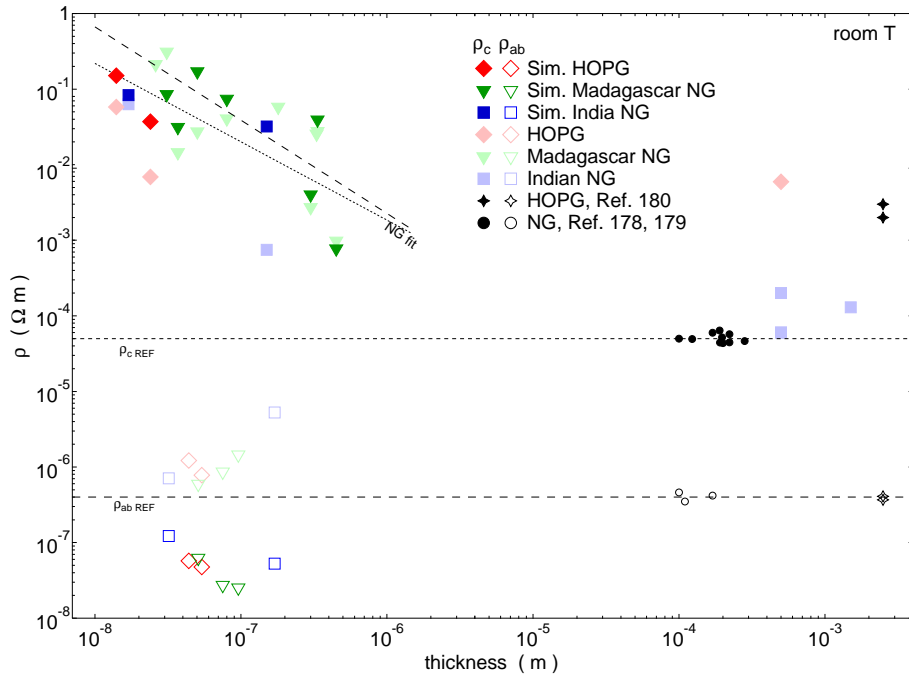
As already stated in the main text the approximated  $\rho_{ab}$  presents an upper bound. This is confirmed by our simulation which give  $\rho_{ab}^{sim} < \rho_{ab}$ , ranging from ratios between  $\rho_{ab}$  and  $\rho_{ab}^{sim}$  of 6 (India 1) to 100 (India 2). We think the main reason for this deviation from the approximative method is the neglected anisotropy for the extraction of  $\rho_{ab}$ , which effectively reduces the current carrying cross-section  $A$ . This is confirmed by the observation that the reduction in  $\rho_{ab}^{sim}$  is largest, where  $R_{ab}$  is measured on the

Table 4: Comparing approximated  $\rho_{ab}$ ,  $\rho_c$  and  $R_A$  with numerically simulated values.

Material	$\rho_{ab}(\text{n}\Omega\text{m})$	$\rho_c(\text{m}\Omega\text{m})$	$R_A$	$\rho_{ab}^{sim}(\text{n}\Omega\text{m})$	$\rho_c^{sim}(\text{m}\Omega\text{m})$	$R_A^{sim}$
HOPG 1	1,200	58	48k	57	150	2,600k
HOPG 2	780	6.9	8.8k	48	37	780k
India 1	710	63	89k	120	84	680k
India 2	5,300	0.78	140	53	32	610k
Madagascar 1	1,500	41	28k	25	74	2,900k
Madagascar 2	600	15	24k	62	32	500k
Madagascar 3	860	310	360k	27	171	6,300k
Madagascar 4	(800)	210	(266k)	(50)		
Madagascar 5	(800)	28	(35k)	(50)	(85)	(1,700k)
Madagascar 6	(800)	25	(31k)	(50)		
Madagascar 7	(800)	2.7	(3.4k)	(50)	(4)	(80k)
Madagascar 8	(800)	1	(1.35k)	(50)	(0.8)	(16k)
Madagascar 9	(800)	28	(35k)	(50)	(39)	(780k)

thickest samples (India 2, Madagascar 1), and smallest for the thinnest sample (India 1). Further, our rather point-like contact geometries have to be corrected for a spread in current, effectively changing the sample geometry in the  $ab$ -plane. That this is indeed a relevant effect can be seen in the potential distribution in the  $ab$ -plane of the sample as calculated by numerical simulation (not shown).

Because of the agreement between  $\rho_{ab}$  and literature values,  $\rho_{ab}^{sim}$  is also much smaller than previously measured in macroscopic samples [178–180]. Although in previous experiments it may have been possible to use more suitable contact geometries to extract  $\rho_{ab}$ , we cannot exclude a similar effect for the deviation of  $\rho_{ab}^{sim}$  from literature values. Another reason for the low  $\rho_{ab}^{sim}$  in exfoliated, nanoscale samples could be the reduction of bulk disorder during exfoliation, actually suggested by our data and the disorder induced delocalization model. Further an  $ab$ -measurement in a macroscopic specimen will extend over several grain boundaries, whereas the multiply cleaved nanosamples are single or few grain graphite.



**Figure 7.5:** Comparison of extraction method for  $\rho_c$  and  $\rho_{ab}$  at room temperature, comparing HOPG (red) with Madagascar NG (green) and Indian NG (blue). Filled, dark markers show  $\rho_c^{sim}$ , empty, dark markers display  $\rho_{ab}^{sim}$  both extracted using the anisotropic resistivity solver. Filled, light markers are  $\rho_c$  and empty, light markers indicated  $\rho_{ab}$ , evaluated using the estimate given and were already included in Fig 2 in the main text. For  $\rho_{ab}$  and  $\rho_{ab}^{sim}$ , the abscissa value is  $d + h$ , the overall flake thickness, see Table 2. Previous measurements of macroscopic samples (black) were added for both HOPG [180] (stars) and NG [178, 179] (circles) for comparison. Dashed horizontal lines indicate literature values  $\rho_{ab,REF}$  for  $\rho_{ab}$  and  $\rho_{c,REF}$  for  $\rho_c$ . Further, the best power-law fits to all NG nanostep data (dotted line for  $\rho_c$  approximated in the main text, slope of  $-1.0 \pm 0.4$ ; dashed line for  $\rho_c^{sim}$  obtained with the simulation, slope of  $-1.2 \pm 0.4$ ;) are added to indicate a potential trend

Despite some big deviations for  $\rho_{ab}$ , the simulations show that  $\rho_c^{sim}$  values are on the same order of magnitude as  $\rho_c$ , obtained using the approximative method. There seems to be a tendency of slightly higher  $\rho_c^{sim}$  (factor of 2-3), but this qualitative agreement clearly strengthens the approximative method to determine  $\rho_c$ . As an overall consequence, the numerically calculated  $R_A^{sim}$  is even higher than shown in the main text, reaching values up to 6,000,000 (Madagascar 3). Notably for India 2, for which we previously extracted a rather low  $\rho_c \sim 0.8$  m $\Omega$ m, now  $\rho_c^{sim} \sim 53$  m $\Omega$ m, in good agreement with all the other samples. Fig. 7.5 compares the two calculation methods graphically, including all samples measured. The results of the approximation already

included in the main text, are plotted in weaker colours. The trend of the thickness dependence for numerically calculated (dashed line) and approximated  $\rho_c$  (dotted line) persists. The slopes of linear fits in the log-log plot lie within the corresponding error bars. The two data points for which the simulation did not converge were omitted in Figure 7.5.

## 7.7 Acknowledgements

We are very grateful to D. Maslov for initiating the experiments and numerous invaluable discussions and to S. Tongay for performing XRD and Raman measurements. Further, we thank F. Dettwiler, D. Maradan and P. Jurcevic for experimental help. This work was supported by the Swiss Nanoscience Institute (SNI), Swiss NSF, ERC starting grant and NCCR QSIT.

## 8 Conclusion & Outlook

Motivated by the benefit from low temperatures in condensed matter systems, especially in semiconducting devices, be it for quantum computation or novel states of matter, this work has successfully implemented an adiabatic nuclear refrigerator (AND) scheme for cooling nanostructured condensed matter samples. The AND setup is characterized in terms of heat leaks and entropic cooling down to  $\sim 200 \mu\text{K}$  is demonstrated. Given the determined heat leak of  $\dot{Q}_0 \leq 1 \text{ nW/mol}$ , the time the nuclear refrigerator can stay below 1 mK is 50 hours (1 week below 2 mK), sufficient for transport experiments in nanostructures. Metallic Coulomb blockade thermometers (CBTs) were in a first experiment cooled to  $\sim 10 \text{ mK}$ , exhibiting a deviation from a predominant electron-phonon coupling mechanism for cooling at the lowest temperatures.  $T_e$  in a two-dimensional electron gas (2DEG) is measured with an electrostatically defined GaAs quantum dot, operated in deep Coulomb blockade, using both direct transport through the dot, as well as charge sensing. The thermometer is demonstrated to work between 20 mK and 120 mK. At base temperature, we find that the 2DEG temperature saturates at 10 mK, and is very sensitive to changes in the wafer i.e. charge switches. We speculate that the intrinsic wafer noise might pose a limit for the lowest temperatures measured.

After replacing the Macor chip socket and chip carrier with an Ag epoxy version, where every wire is additionally filtered, we are able to reduce the lowest  $T_e$  in metallic nanostructures to  $\sim 6 \text{ mK}$ . For these experiments we implement yet another primary electron thermometer based on a normal metal/insulator/superconductor (NIS) tunnel junction. The NIS thermometer shows a peculiar dependence on  $B$ -field, and a deviation from the theoretical I-V behavior at the lowest currents at the lowest temperature. Both effects are not understood at present, but we speculate that the  $B$ -field dependence could be caused by flux trapping like behaviour in the superconductor. In terms of  $T_e$  in semiconductors, we employ a GaAs high mobility 2DEG, using very tempera-

ture sensitive reentrant quantum Hall states, to demonstrate cooling of electrons below base  $T$  upon demagnetization. Extrapolation of the temperature dependence of the reentrant features gives  $T_e \sim 5$  mK. On top of the limitations of thermal conductance and residual heat leaks in our system, we discuss the effect of voltage noise on our electron thermometers.

It certainly would be interesting to remeasure GaAs quantum dot devices in the improved setup with the Ag epoxy Faraday cup. The 2DEG potentially could cool below 10 mK and there might be the possibility to investigate effects of different kinds of noise, similar to a recent measurement in optically active quantum dots [100]. Further, there exists a recent proposal for backaction effects [201], fundamentally interesting and also relevant for spin and charge qubits [98]. In addition the investigation of correlated many body states like the Kondo effect and higher order manifestations could be enabled by our low electron temperatures [82, 202].

With low temperatures at hand, we attempt to investigate the elusive  $\nu = 5/2$  and other fractional quantum Hall states with low energy gaps. Due to an electron density gradient in the sample, we find quantized longitudinal resistance  $R_{xx}$  in the integer quantum Hall effect (QHE). We can show that the density gradient has a detrimental effect on the  $\nu = 5/2$  gap extraction. After having improved the wafer quality, our low electron temperatures will be very beneficial for probing the  $\nu = 5/2$  statistics in tunneling [80, 153], interferometer [154–156] and antidot [203–205] type of experiments. Along similar lines, low electron temperatures could facilitate experimental tests of a recently put forward stripe model [206] of the quantum Hall effect, like a nuclear phase transition in the one-dimensional stripes [207]. Similarly, experimental evidence for an electron-mediated nuclear ferromagnetic phase transition in two dimensions is still lacking [36, 37]. Another open question in condensed matter physics is, if the electron phase coherence time saturates at the lowest temperatures [88] or not [208]. Our setup could extend the investigated range considerably, shedding some light onto the matter.

In summary, this PhD work is a first step toward future low temperature electron



transport experiments, enabling the investigation of exotic and exciting condensed matter physics.

## References

- [1] M. Planck. *Über das Gesetz der Energieverteilung im Normalspectrum*. Annalen der Physik **309**, 553 (1901).
- [2] A. Cho. *Higgs Boson makes its debut after decades-long search*. Science (2012).
- [3] W. Kohn. *An essay on condensed matter physics in the twentieth century*. Review of Modern Physics **71**, S59 (1999).
- [4] P. Debye. *Zur Theorie der spezifischen Wärme*. Annalen der Physik **39**, 789 (1912).
- [5] C. Enss and S. Hunklinger. *Low-Temperature Physics*. SpringerLink: Springer e-Books (Springer, 2005).
- [6] J. K. Jain. *Composite-fermion approach for the fractional quantum Hall effect*. Physical Review Letters **63**, 199 (1989).
- [7] K. Andres, J. E. Graebner, and H. R. Ott. *4f Virtual-Bound-State Formation in CeAl<sub>3</sub> at Low Temperatures*. Physical Review Letters **35**, 1779 (1975).
- [8] F. Steglich, J. Aarts, C. D. Bredl, W. Lieke, D. Meschede, W. Franz, and H. Schäfer. *Superconductivity in the Presence of Strong Pauli Paramagnetism: CeCu<sub>2</sub>Si<sub>2</sub>*. Physical Review Letters **43**, 1892 (1979).
- [9] K. S. Novoselov, A. K. Geim, S. V. Morozov, D. Jiang, M. I. Katsnelson, I. V. Grigorieva, S. V. Dubonos, and A. A. Firsov. *Two-dimensional gas of massless Dirac fermions in graphene*. Nature **438**, 197 (2005).
- [10] Y. Zhang, Y.-W. Tan, H. L. Stormer, and P. Kim. *Experimental observation of the quantum Hall effect and Berry's phase in graphene*. Nature **438**, 201 (2005).
- [11] E. Majorana. *Teoria simmetrica delle elettrone e del positrone*. Il Nuovo Cimento **14**, 171 (1937).
- [12] V. Mourik, K. Zuo, S. M. Frolov, S. R. Plissard, E. P. A. M. Bakkers, and L. P. Kouwenhoven. *Signatures of Majorana Fermions in Hybrid Superconductor-Semiconductor Nanowire Devices*. Science **336**, 1003 (2012).
- [13] Bose. *Plancks Gesetz und Lichtquantenhypothese*. Zeitschrift für Physik **26**, 178 (1924).
- [14] M. H. Anderson, J. R. Ensher, M. R. Matthews, C. E. Wieman, and E. A. Cornell. *Observation of Bose-Einstein Condensation in a Dilute Atomic Vapor*. Science **269**, 198 (1995).
- [15] K. von Klitzing, G. Dorda, and M. Pepper. *New Method for High-Accuracy Determination of the Fine-Structure Constant Based on Quantized Hall Resistance*. Physical Review Letters **45**, 494 (1980).

- 
- [16] D. C. Tsui, H. L. Stormer, and A. C. Gossard. *Two-Dimensional Magnetotransport in the Extreme Quantum Limit*. Physical Review Letters **48**, 1559 (1982).
- [17] M. Z. Hasan and C. L. Kane. *Colloquium: Topological Insulators*. Review of Modern Physics **82**, 3045 (2010).
- [18] F. Wilczek. *Quantum Mechanics of Fractional-Spin Particles*. Physical Review Letters **49**, 957 (1982).
- [19] G. Moore and N. Read. *Nonabelions in the fractional quantum hall effect*. Nuclear Physics B **360**, 362 (1991).
- [20] H. K. Onnes. *Further experiments with liquid helium. C. On the change of electric resistance of pure metals at very low temperatures etc. IV. The resistance of pure mercury at helium temperatures*. In *KNAW, Proceedings*, volume 13, 1910–1911 (1911).
- [21] P. W. Anderson. *Localized Magnetic States in Metals*. Physical Review **124**, 41 (1961).
- [22] J. Kondo. *Resistance Minimum in Dilute Magnetic Alloys*. Progress of Theoretical Physics **32**, 37 (1964).
- [23] P. Kapitza. *Viscosity of Liquid Helium below the  $\lambda$ -Point*. Nature **141**, 74 (1938).
- [24] D. D. Osheroff, R. C. Richardson, and D. M. Lee. *Evidence for a New Phase of Solid He<sup>3</sup>*. Physical Review Letters **28**, 885 (1972).
- [25] T. A. Fulton and G. J. Dolan. *Observation of single-electron charging effects in small tunnel junctions*. Physical Review Letters **59**, 109 (1987).
- [26] U. Meirav, M. A. Kastner, and S. J. Wind. *Single-electron charging and periodic conductance resonances in GaAs nanostructures*. Physical Review Letters **65**, 771 (1990).
- [27] M. A. Kastner. *The single-electron transistor*. Review of Modern Physics **64**, 849 (1992).
- [28] M. A. Nielsen and I. L. Chuang. *Quantum Computation and Quantum Information* (Cambridge University Press, 2004), 1<sup>st</sup> edition.
- [29] E. Knill, R. Laflamme, and G. J. Milburn. *A scheme for efficient quantum computation with linear optics*. Nature **409**, 46 (2001).
- [30] J. I. Cirac and P. Zoller. *Quantum Computations with Cold Trapped Ions*. Physical Review Letters **74**, 4091 (1995).
- [31] J. Clarke and F. K. Wilhelm. *Superconducting quantum bits*. Nature **453**, 1031 (2008).
- [32] Y. Nakamura, Y. A. Pashkin, and J. S. Tsai. *Coherent control of macroscopic quantum states in a single-Cooper-pair box*. Nature **398**, 786 (1999).

- [33] D. Loss and D. P. DiVincenzo. *Quantum computation with quantum dots*. Physical Review A **57**, 120 (1998).
- [34] D. P. DiVincenzo. *The physical implementation of quantum computation*. arXiv:0002.077 (2000).
- [35] T. Ihn. *Semiconductor Nanostructures: Quantum States and Electronic Transport* (OUP Oxford, 2010).
- [36] P. Simon and D. Loss. *Nuclear Spin Ferromagnetic Phase Transition in an Interacting Two Dimensional Electron Gas*. Physical Review Letters **98**, 156401 (2007).
- [37] P. Simon, B. Braunecker, and D. Loss. *Magnetic ordering of nuclear spins in an interacting two-dimensional electron gas*. Physical Review B **77**, 045108 (2008).
- [38] O. Lounasmaa. *Experimental Principles and Methods Below 1K*. Academic, London (1974).
- [39] F. Pobell. *Matter and Methods at Low Temperatures* (Springer, Berlin, 2007).
- [40] G. Pickett. *Microkelvin physics*. Reports on Progress in Physics **51**, 1295 (1988).
- [41] W. Wendler, T. Hermannsdörfer, S. Rehmann, and P. F. *Electronic and nuclear magnetism in PtFex at milli-, and nanokelvin temperatures*. Europhysics Letters **38**, 619 (1997).
- [42] T. Knuuttila, J. Tuoriniemi, K. Lefmann, K. Juntunen, F. Rasmussen, and K. Nummila. *Polarized Nuclei in Normal and Superconducting Rhodium*. Journal of Low Temperature Physics **123**, 65 (2001).
- [43] V. Venkatachalam, S. Hart, L. Pfeiffer, K. West, and A. Yacoby. *Local thermometry of neutral modes on the quantum Hall edge*. Nature Physics **8**, 676 (2012).
- [44] N. Ashcroft and N. Mermin. *Solid state physics*. Science: Physics (Saunders College, 1976).
- [45] D. Zumbühl, K. Schwarzwälder, and T. Bandi. *Silver Sinter Heat Exchangers*. Ph.D. thesis, University of Basel (2008).
- [46] G. Batey, A. Casey, M. Cuthbert, A. Matthews, J. Saunders, and A. Shihahara. *A microkelvin cryogen-free experimental platform with integrated noise thermometry*. New Journal of Physics **15** (2013).
- [47] I. F. Silvera. *The solid molecular hydrogens in the condensed phase: Fundamentals and static properties*. Review of Modern Physics **52**, 393 (1980).
- [48] A. C. Clark, K. K. Schwarzwälder, T. Bandi, D. Maradan, and D. M. Zumbühl. *Method for cooling nanostructures to microkelvin temperatures*. Review of Scientific Instruments **81**, 103904 (2010).

- [49] S. Brunauer, P. H. Emmett, and E. Teller. *Adsorption of Gases in Multimolecular Layers*. Journal of the American Chemical Society **60**, 309 (1938).
- [50] N. Lawson. *A simple heat switch for use at millikelvin temperatures*. Cryogenics **22**, 667 (1982).
- [51] C. Kittel. *Introduction to Solid State Physics* (Wiley and Sons, 1976).
- [52] D. Paulson, M. Krusius, J. Wheatley, R. Safrata, M. Kolac, T. Thetal, K. Svec, and J. Matas. *Magnetic thermometry to below one millikelvin with lanthanum-diluted cerium magnesium nitrate*. Journal of Low Temperature Physics **34**, 63 (1979).
- [53] R. Mitchell, A. Eastop, E. Faraj, and J. Hook. *The specific heat capacity and thermal conductivity of normal liquid  $^3\text{He}$* . Journal of Low Temperature Physics **64**, 43 (1986).
- [54] V. Shvarts. *private communication*.
- [55] K. Gloos, C. Mitschka, F. Pobell, and P. Smeibidl. *Thermal conductivity of normal and superconducting metals*. Cryogenics **30**, 14 (1990).
- [56] G. Pickett. *Cooling metals to the microkelvin regime, then and now*. Physica B: Condensed Matter **280**, 467 (2000).
- [57] D. Maradan, K. Schwarzwalder, A. Clark, and D. M. Zumbuhl. *Parallel Nuclear Refrigerators for Cooling Nanoscale Samples to Microkelvin Temperatures*. Ph.D. thesis, University of Basel (2010).
- [58] K. Schwarzwalder and T. Bandi. *Towards Cooling Nanoelectronic Devices to Microkelvin Temperatures*. Ph.D. thesis, University of Basel (2008).
- [59] R. Hanson, L. P. Kouwenhoven, J. R. Petta, S. Tarucha, and L. M. K. Vandersypen. *Spins in few-electron quantum dots*. Review of Modern Physics **79**, 1217 (2007).
- [60] C. Nayak, S. H. Simon, A. Stern, M. Freedman, and S. Das Sarma. *Non-Abelian anyons and topological quantum computation*. Review of Modern Physics **80**, 1083 (2008).
- [61] A. Stern. *Non-Abelian states of matter*. Nature **464**, 187 (2010).
- [62] N. Samkharadze, A. Kumar, M. J. Manfra, L. N. Pfeiffer, K. W. West, and G. A. Csathy. *Integrated electronic transport and thermometry at milliKelvin temperatures and in strong magnetic fields*. Review of Scientific Instruments **82**, 053902 (2011).
- [63] W. Pan, J.-S. Xia, V. Shvarts, D. E. Adams, H. L. Stormer, D. C. Tsui, L. N. Pfeiffer, K. W. Baldwin, and K. W. West. *Exact Quantization of the Even-Denominator Fractional Quantum Hall State at  $\nu = 5/2$  Landau Level Filling Factor*. Physical Review Letters **83**, 3530 (1999).

- [64] J. Huang, J. Xia, D. Tsui, L. Pfeiffer, and K. West. *Disappearance of Metal-Like Behavior in GaAs Two-Dimensional Holes below 30 mK*. Physical Review Letters **98**, 226801 (2007).
- [65] L. Spietz, R. J. Schoelkopf, and P. Pari. *Shot noise thermometry down to 10 mK*. Applied Physics Letters **89**, 183123 (2006).
- [66] J. P. Pekola, K. P. Hirvi, J. P. Kauppinen, and M. A. Paalanen. *Thermometry by Arrays of Tunnel Junctions*. Physical Review Letters **73**, 2903 (1994).
- [67] M. Meschke, J. Engert, D. Heyer, and J. P. Pekola. *Comparison of Coulomb Blockade Thermometers with the International Temperature Scale PLTS-2000*. International Journal of Thermophysics **32**, 1378 (2011).
- [68] A. B. Zorin. *The thermocoax cable as the microwave frequency filter for single electron circuits*. Review of Scientific Instruments **66**, 4296 (1995).
- [69] C. Scheller, S. Heizmann, D. Giss, K. Bedner, M. Meschke, D. M. Zumbuhl, J. D. Zimmerman, and A. C. Gossard. *Silver-Epoxy Microwave Filters and Thermalizers for Millikelvin Experiments*. Applied Physics Letters **104**, 211106 (2014).
- [70] M. Meschke, J. P. Pekola, F. Gay, R. E. Rapp, and H. Godfrin. *Electron Thermalization in Metallic Islands Probed by Coulomb Blockade Thermometry*. Journal of Low Temperature Physics **134**, 1119 (2004).
- [71] H. van Houten, C. W. J. Beenakker, and A. A. M. Staring. *Coulomb Blockade Oscillations in Semiconductor Nanostructures* (Published in Single Charge Tunneling, edited by H. Grabert and M. H. Devoret, NATO ASI Series B294, Plenum, New York, 1992).
- [72] L. P. Kouwenhoven, C. M. Marcus, P. L. McEuen, S. Tarucha, R. M. Westervelt, and N. S. Wingreen. *Electron transport in quantum dots*, volume 345 (Proceedings of the NATO Advanced Study Institute on Mesoscopic Electron Transport, Springer, Dordrecht, Netherlands, 1996).
- [73] B. Braunecker, P. Simon, and D. Loss. *Nuclear magnetism and electron order in interacting one-dimensional conductors*. Physical Review B **80**, 165119 (2009).
- [74] C. P. Scheller, T.-M. Liu, G. Barak, A. Yacoby, L. N. Pfeiffer, K. W. West, and D. M. Zumbühl. *Possible Evidence for Helical Nuclear Spin Order in GaAs Quantum Wires*. Physical Review Letters **112**, 066801 (2014).
- [75] C. Jayaprakash, H. R. Krishna-murthy, and J. W. Wilkins. *Two-Impurity Kondo Problem*. Physical Review Letters **47**, 737 (1981).
- [76] P. Nozieres and A. Blandin. *Kondo effect in real metals*. Journal of Physics France **41**, 193 (1980).
- [77] A. Zawadowski. *Kondo-like State in a Simple Model for Metallic Glasses*. Physical Review Letters **45**, 211 (1980).

- [78] R. Willett, J. P. Eisenstein, H. L. Stormer, D. C. Tsui, A. C. Gossard, and J. H. English. *Observation of an even-denominator quantum number in the fractional quantum Hall effect*. Physical Review Letters **59**, 1776 (1987).
- [79] Y. C. Chung, M. Heiblum, and V. Umansky. *Scattering of Bunched Fractionally Charged Quasiparticles*. Physical Review Letters **91**, 216804 (2003).
- [80] I. P. Radu, J. B. Miller, C. M. Marcus, M. A. Kastner, L. N. Pfeiffer, and K. W. West. *Quasi-Particle Properties from Tunneling in the  $\nu = 5/2$  Fractional Quantum Hall State*. Science **320**, 899 (2008).
- [81] D. T. McClure, W. Chang, C. M. Marcus, L. N. Pfeiffer, and K. W. West. *Fabry-Perot Interferometry with Fractional Charges*. Physical Review Letters **108**, 256804 (2012).
- [82] R. M. Potok, I. G. Rau, H. Shtrikman, Y. Oreg, and D. Goldhaber-Gordon. *Observation of the two-channel Kondo effect*. Nature **446**, 167 (2007).
- [83] I. Karakurt, V. J. Goldman, J. Liu, and A. Zaslavsky. *Absence of Compressible Edge Channel Rings in Quantum Antidots*. Physical Review Letters **87**, 146801 (2001).
- [84] L. Casparis, M. Meschke, D. Maradan, A. C. Clark, C. P. Scheller, K. K. Schwarzwalder, J. P. Pekola, and D. M. Zumbühl. *Metallic Coulomb blockade thermometry down to 10 mK and below*. Review of Scientific Instruments **83**, 083903 (2012).
- [85] A. Rossi, T. Ferrus, and D. A. Williams. *Electron temperature in electrically isolated Si double quantum dots*. Applied Physics Letters **100**, 133503 (2012).
- [86] A. Mavalankar, S. J. Chorley, J. Griffiths, G. A. C. Jones, I. Farrer, D. A. Ritchie, and C. G. Smith. *A non-invasive electron thermometer based on charge sensing of a quantum dot*. Applied Physics Letters **103**, 133116 (2013).
- [87] P. Torresani, M. J. Martinez-Perez, S. Gasparinetti, J. Renard, G. Biasiol, L. Sorba, F. Giazotto, and S. De Franceschi. *Nongalvanic primary thermometry of a two-dimensional electron gas*. Physical Review B **88**, 245304 (2013).
- [88] A. G. Huibers, J. A. Folk, S. R. Patel, C. M. Marcus, C. I. Duruöz, and J. S. Harris. *Low-Temperature Saturation of the Dephasing Time and Effects of Microwave Radiation on Open Quantum Dots*. Physical Review Letters **83**, 5090 (1999).
- [89] C. Altimiras, H. le Sueur, U. Gennser, A. Cavanna, D. Mailly, and F. Pierre. *Non-equilibrium edge-channel spectroscopy in the integer quantum Hall regime*. Nature Physics **6**, 34 (2010).
- [90] O. E. Dial, M. D. Shulman, S. P. Harvey, H. Bluhm, V. Umansky, and A. Yacoby. *Charge Noise Spectroscopy Using Coherent Exchange Oscillations in a Singlet-Triplet Qubit*. Physical Review Letters **110**, 146804 (2013).

- [91] A. K. M. Wennberg, S. N. Ytterboe, C. M. Gould, H. M. Bozler, J. Klem, and H. Morkoç. *Electron heating in a multiple-quantum-well structure below 1 K*. Physical Review B **34**, 4409 (1986).
- [92] P. L. Gammel, D. J. Bishop, J. P. Eisenstein, J. H. English, A. C. Gossard, R. Ruel, and H. L. Stormer. *Ultralow-temperature behavior of the  $\nu = 5/2$  fractional quantum Hall effect*. Physical Review B **38**, 10128 (1988).
- [93] H. L. Edwards, Q. Niu, and A. L. de Lozanne. *A quantum-dot refrigerator*. Applied Physics Letters **63**, 1815 (1993).
- [94] M. Field, C. G. Smith, M. Pepper, D. A. Ritchie, J. E. F. Frost, G. A. C. Jones, and D. G. Hasko. *Measurements of Coulomb blockade with a noninvasive voltage probe*. Physical Review Letters **70**, 1311 (1993).
- [95] J. M. Elzerman, R. Hanson, J. S. Greidanus, L. H. Willems van Beveren, S. De Franceschi, L. M. K. Vandersypen, S. Tarucha, and L. P. Kouwenhoven. *Few-electron quantum dot circuit with integrated charge read out*. Physical Review B **67**, 161308 (2003).
- [96] L. DiCarlo, H. J. Lynch, A. C. Johnson, L. I. Childress, K. Crockett, C. M. Marcus, M. P. Hanson, and A. C. Gossard. *Differential Charge Sensing and Charge Delocalization in a Tunable Double Quantum Dot*. Physical Review Letters **92**, 226801 (2004).
- [97] S. Gasparinetti, M. J. Martínez-Pérez, S. de Franceschi, J. P. Pekola, and F. Giazotto. *Nongalvanic thermometry for ultracold two-dimensional electron domains*. Applied Physics Letters **100**, 253502 (2012).
- [98] G. Granger, D. Taubert, C. E. Young, L. Gaudreau, A. Kam, S. A. Studenikin, P. Zawadzki, D. Harbusch, D. Schuh, W. Wegscheider, Z. R. Wasilewski, A. A. Clerk, S. Ludwig, and A. S. Sachrajda. *Quantum interference and phonon-mediated back-action in lateral quantum-dot circuits*. Nature Physics **8**, 522 (2012).
- [99] W. G. van der Wiel, S. De Franceschi, J. M. Elzerman, T. Fujisawa, S. Tarucha, and L. P. Kouwenhoven. *Electron transport through double quantum dots*. Review of Modern Physics **75**, 1 (2002).
- [100] A. V. Kuhlmann, J. Houel, A. Ludwig, L. Greuter, D. Reuter, A. D. Wieck, M. Poggio, and R. J. Warburton. *Charge noise and spin noise in a semiconductor quantum device*. Nature Physics **9**, 570 (2013).
- [101] S. Amasha, K. MacLean, I. P. Radu, D. M. Zumbühl, M. A. Kastner, M. P. Hanson, and A. C. Gossard. *Electrical Control of Spin Relaxation in a Quantum Dot*. Physical Review Letters **100**, 046803 (2008).
- [102] M. Ciorga, A. S. Sachrajda, P. Hawrylak, C. Gould, P. Zawadzki, S. Jullian, Y. Feng, and Z. Wasilewski. *Addition spectrum of a lateral dot from Coulomb and spin-blockade spectroscopy*. Physical Review B **61**, R16315 (2000).



- [103] M. Pioro-Ladriere, J. H. Davies, A. R. Long, A. S. Sachrajda, L. Gaudreau, P. Zawadzki, J. Lapointe, J. Gupta, Z. Wasilewski, and S. Studenikin. *Origin of switching noise in GaAs/AlGaAs lateral gated devices*. Physical Review B **72**, 115331 (2005).
- [104] C. Buizert, F. H. L. Koppens, M. Pioro-Ladrière, H.-P. Tranitz, I. T. Vink, S. Tarucha, W. Wegscheider, and L. M. K. Vandersypen. *In-Situ Reduction of Charge Noise in GaAs/AlGaAs Schottky-Gated Devices*. Physical Review Letters **101**, 226603 (2008).
- [105] C. Barthel, M. Kjærgaard, J. Medford, M. Stopa, C. M. Marcus, M. P. Hanson, and A. C. Gossard. *Fast sensing of double-dot charge arrangement and spin state with a radio-frequency sensor quantum dot*. Physical Review B **81**, 161308 (2010).
- [106] D. Paget, G. Lampel, B. Sapoval, and V. I. Safarov. *Low field electron-nuclear spin coupling in gallium arsenide under optical pumping conditions*. Physical Review B **15**, 5780 (1977).
- [107] W. A. Coish and D. Loss. *Hyperfine interaction in a quantum dot: Non-Markovian electron spin dynamics*. Physical Review B **70**, 195340 (2004).
- [108] S. Hess, D. Maradan, L. Casparis, T.-M. Liu, and D. M. Zumbühl. *Projektreport: Mikrokelvin Chip Carrier*. Ph.D. thesis, University of Basel (2010).
- [109] L. Conrad, D. Maradan, L. Casparis, and D. M. Zumbühl. *Low Resistance Ohmic Contacts to a GaAs 2D Electron Gas for Ultra-Low Temperatures*. Ph.D. thesis, University of Basel (2014).
- [110] A. Feshchenko, M. Meschke, D. Gunnarsson, M. Prunnila, L. Roschier, J. Penttila, and J. Pekola. *Primary Thermometry in the Intermediate Coulomb Blockade Regime*. Journal of Low Temperature Physics **173**, 36 (2013).
- [111] I. Giaever. *Energy Gap in Superconductors Measured by Electron Tunneling*. Physical Review Letter **5**, 147 (1960).
- [112] J. M. Rowell and D. C. Tsui. *Hot electron temperature in InAs measured by tunneling*. Physical Review B **14**, 2456 (1976).
- [113] M. Nahum and J. M. Martinis. *Ultrasensitive-hot-electron microbolometer*. Applied Physics Letters **63**, 3075 (1993).
- [114] D. V. Averin and Y. V. Nazarov. *Virtual electron diffusion during quantum tunneling of the electric charge*. Physical Review Letters **65**, 2446 (1990).
- [115] J. Bardeen, L. N. Cooper, and J. R. Schrieffer. *Theory of Superconductivity*. Physical Review **108**, 1175 (1957).
- [116] F. Giazotto, T. T. Heikkilä, A. Luukanen, A. M. Savin, and J. P. Pekola. *Opportunities for mesoscopics in thermometry and refrigeration: Physics and applications*. Review of Modern Physics **78**, 217 (2006).

- [117] M. Meschke, W. Guichard, and J. P. Pekola. *Single-mode heat conduction by photons*. Nature **444**, 187 (2006).
- [118] F. Giazotto and M. J. Martinez-Perez. *The Josephson heat interferometer*. Nature **492**, 401 (2012).
- [119] D. R. Schmidt, C. S. Yung, and A. N. Cleland. *Nanoscale radio-frequency thermometry*. Applied Physics Letters **83**, 1002 (2003).
- [120] P. Koppinen, T. Kühn, and I. Maasilta. *Effects of Charging Energy on SINIS Tunnel Junction Thermometry*. Journal of Low Temperature Physics **154**, 179 (2009).
- [121] A. Maldonado, H. Suderow, and S. Vieira. *Thermometry with a nearly temperature independent sensitivity using a normal-superconducting tunnel diode biased close to the superconducting gap*. Cryogenics **50**, 397 (2010).
- [122] A. Andreev. *Thermal conductivity of the intermediate state of superconductors*. Soviet Physics JETP **19**, 1228 (1964).
- [123] J. M. Hergenrother, M. T. Tuominen, and M. Tinkham. *Charge transport by Andreev reflection through a mesoscopic superconducting island*. Physical Review Letters **72**, 1742 (1994).
- [124] H. Pothier, S. Guéron, D. Esteve, and M. H. Devoret. *Flux-Modulated Andreev Current Caused by Electronic Interference*. Physical Review Letters **73**, 2488 (1994).
- [125] S. Rajauria, P. Gandit, T. Fournier, F. W. J. Hekking, B. Pannetier, and H. Courtois. *Andreev Current-Induced Dissipation in a Hybrid Superconducting Tunnel Junction*. Physical Review Letters **100**, 207002 (2008).
- [126] J. P. Pekola, V. F. Maisi, S. Kafanov, N. Chekurov, A. Kemppinen, Y. A. Pashkin, O.-P. Saira, M. Möttönen, and J. S. Tsai. *Environment-Assisted Tunneling as an Origin of the Dynes Density of States*. Physical Review Letters **105** (2010).
- [127] D. Golubev and L. Kuzmin. *Nonequilibrium theory of a hot-electron bolometer with normal metal-insulator-superconductor tunnel junction*. Journal of Applied Physics **89**, 6464 (2001).
- [128] J. Kivioja, I. Maasilta, J. Pekola, and J. Karvonen. *Response time of a thermometer based on normal metal/insulator/superconductor (NIS) tunnel junctions*. Physica E: Low-dimensional Systems and Nanostructures **18**, 21 (2003).
- [129] H. Pothier, S. Guaron, N. O. Birge, D. Esteve, and M. H. Devoret. *Energy distribution function of quasiparticles in mesoscopic wires*. Physical Review Letters **79**, 3490 (1997).
- [130] M. Nahum, T. M. Eiles, and J. M. Martinis. *Electronic microrefrigerator based on a normal-insulator-superconductor tunnel junction*. Applied Physics Letters **65**, 3123 (1994).

- [131] M. M. Leivo, J. P. Pekola, and D. V. Averin. *Efficient Peltier refrigeration by a pair of normal metal/insulator/superconductor junctions*. Applied Physics Letters **68**, 1996 (1996).
- [132] P. A. Fisher, J. N. Ullom, and M. Nahum. *High-power on-chip microrefrigerator based on a normal-metal/insulator/superconductor tunnel junction*. Applied Physics Letters **74**, 2705 (1999).
- [133] A. M. Clark, A. Williams, S. T. Ruggiero, M. L. van den Berg, and J. N. Ullom. *Practical electron-tunneling refrigerator*. Applied Physics Letters **84**, 625 (2004).
- [134] M. Tinkham. *Effect of Fluxoid Quantization on Transitions of Superconducting Films*. Physical Review **129**, 2413 (1963).
- [135] J. T. Peltonen, J. T. Muhonen, M. Meschke, N. B. Kopnin, and J. P. Pekola. *Magnetic-field-induced stabilization of nonequilibrium superconductivity in a normal-metal/insulator/superconductor junction*. Physical Review B **84**, 220502 (2011).
- [136] H. Courtois, S. Rajauria, P. Gandit, F. Hekking, and B. Pannetier. *Inherent Thermometry in a Hybrid Superconducting Tunnel Junction*. Journal of Low Temperature Physics **153**, 325 (2008).
- [137] R. C. Dynes, V. Narayanamurti, and J. P. Garno. *Direct Measurement of Quasiparticle-Lifetime Broadening in a Strong-Coupled Superconductor*. Physical Review Letters **41**, 1509 (1978).
- [138] R. C. Dynes, J. P. Garno, G. B. Hertel, and T. P. Orlando. *Tunneling Study of Superconductivity near the Metal-Insulator Transition*. Physical Review Letters **53**, 2437 (1984).
- [139] K. Y. Arutyunov, T. I. Suppala, J. K. Suoknuuti, and J. P. Pekola. *Influence of magnetic field on cooling by normal-insulator-superconductor junctions*. Journal of Applied Physics **88**, 326 (2000).
- [140] M. P. Lilly, K. B. Cooper, J. P. Eisenstein, L. N. Pfeiffer, and K. W. West. *Evidence for an Anisotropic State of Two-Dimensional Electrons in High Landau Levels*. Physical Review Letters **82**, 394 (1999).
- [141] K. B. Cooper, M. P. Lilly, J. P. Eisenstein, L. N. Pfeiffer, and K. W. West. *Insulating phases of two-dimensional electrons in high Landau levels: Observation of sharp thresholds to conduction*. Physical Review B **60**, R11285 (1999).
- [142] J. P. Eisenstein, K. B. Cooper, L. N. Pfeiffer, and K. W. West. *Insulating and Fractional Quantum Hall States in the First Excited Landau Level*. Physical Review Letters **88**, 076801 (2002).
- [143] G. A. Csáthy, J. S. Xia, C. L. Vicente, E. D. Adams, N. S. Sullivan, H. L. Stormer, D. C. Tsui, L. N. Pfeiffer, and K. W. West. *Tilt-Induced Localization and Delocalization in the Second Landau Level*. Physical Review Letters **94**, 146801 (2005).

- [144] W. Pan, J. Xia, H. Stormer, D. Tsui, C. Vicente, E. Adams, N. Sullivan, L. Pfeiffer, K. Baldwin, and K. West. *Experimental studies of the fractional quantum Hall effect in the first excited Landau level*. Physical Review B **77**, 075307 (2008).
- [145] W. Pan, J. Xia, H. Stormer, D. Tsui, C. Vicente, E. Adams, N. Sullivan, L. Pfeiffer, K. Baldwin, and K. West. *Low temperature electronic transports in the presence of a density gradient*. Solid State Communications **140**, 88 (2006).
- [146] M. O. Goerbig, P. Lederer, and C. Morais Smith. *Microscopic theory of the reentrant integer quantum Hall effect in the first and second excited Landau levels*. Physical Review B **68**, 241302 (2003).
- [147] J. Olivero and R. Longbothum. *Empirical fits to the Voigt line width: A brief review*. Journal of Quantitative Spectroscopy and Radiative Transfer **17**, 233 (1977).
- [148] A. Kumar, G. A. Csáthy, M. J. Manfra, L. N. Pfeiffer, and K. W. West. *Non-conventional Odd-Denominator Fractional Quantum Hall States in the Second Landau Level*. Physical Review Letters **105**, 246808 (2010).
- [149] A. Y. Kitaev. *Fault-tolerant quantum computation by anyons*. Annals of Physics **303**, 2 (2003).
- [150] A. Kitaev. *Anyons in an exactly solved model and beyond*. Annals of Physics **321**, 2 (2006).
- [151] S. Das Sarma, M. Freedman, and C. Nayak. *Topologically Protected Qubits from a Possible Non-Abelian Fractional Quantum Hall State*. Physical Review Letters **94**, 166802 (2005).
- [152] M. Dolev, M. Heiblum, V. Umansky, A. Stern, and D. Mahalu. *Observation of a quarter of an electron charge at the  $\nu = 5/2$  quantum Hall state*. Nature **452**, 829 (2008).
- [153] J. B. Miller, I. P. Radu, D. M. Zumbühl, E. M. Levenson-Falk, M. A. Kastner, C. M. Marcus, L. N. Pfeiffer, and K. W. West. *Fractional quantum Hall effect in a quantum point contact at filling fraction  $5/2$* . Nature Physics **3**, 561 (2007).
- [154] R. L. Willett, L. N. Pfeiffer, and K. W. West. *Measurement of filling factor  $5/2$  quasiparticle interference with observation of charge  $e/4$  and  $e/2$  period oscillations*. Proceedings of the National Academy of Sciences **106**, 8853 (2009).
- [155] R. L. Willett, L. N. Pfeiffer, and K. W. West. *Alternation and interchange of  $e/4$  and  $e/2$  period interference oscillations consistent with filling factor  $5/2$  non-Abelian quasiparticles*. Physical Review B **82**, 205301 (2010).
- [156] R. L. Willett, C. Nayak, K. Shtengel, L. N. Pfeiffer, and K. W. West. *Magnetic-Field-Tuned Aharonov-Bohm Oscillations and Evidence for Non-Abelian Anyons at  $\nu = 5/2$* . Physical Review Letters **111**, 186401 (2013).
- [157] L. Tiemann, G. Gamez, N. Kumada, and K. Muraki. *Unraveling the Spin Polarization of the  $\nu = 5/2$  Fractional Quantum Hall State*. Science **335**, 828 (2012).

- [158] H. Choi, W. Kang, S. Das Sarma, L. Pfeiffer, and K. West. *Activation gaps of fractional quantum Hall effect in the second Landau level*. Physical Review B **77**, 081301 (2008).
- [159] R. Morf, N. d'Ambrumenil, and S. Das Sarma. *Excitation gaps in fractional quantum Hall states: An exact diagonalization study*. Physical Review B **66**, 075408 (2002).
- [160] J. Nuebler, V. Umansky, R. Morf, M. Heiblum, K. von Klitzing, and J. Smet. *Density dependence of the  $\nu = 5/2$  energy gap: Experiment and theory*. Physical Review B **81**, 035316 (2010).
- [161] G. Gamez and K. Muraki.  *$\nu = 5/2$  fractional quantum Hall state in low-mobility electron systems: Different roles of disorder*. Physical Review B **88**, 075308 (2013).
- [162] C. Dean, B. Piot, P. Hayden, S. Das Sarma, G. Gervais, L. Pfeiffer, and K. West. *Intrinsic Gap of the  $\nu = 5/2$  Fractional Quantum Hall State*. Physical Review Letters **100**, 146803 (2008).
- [163] N. Deng, G. Gardner, S. Mondal, E. Kleinbaum, M. Manfra, and G. Csathy.  *$\nu = 5/2$  Fractional Quantum Hall State in the Presence of Alloy Disorder*. Physical Review Letters **112**, 116804 (2014).
- [164] W. Pan, J. Xia, H. Stormer, D. Tsui, C. Vicente, E. Adams, N. Sullivan, L. Pfeiffer, K. Baldwin, and K. West. *Quantization of the Diagonal Resistance: Density Gradients and the Empirical Resistance Rule in a 2D System*. Physical Review Letters **95**, 066808 (2005).
- [165] D. A. Syphers and P. J. Stiles. *Contiguous two-dimensional regions in the quantized Hall regime*. Physical Review B **32**, 6620 (1985).
- [166] S. Washburn, A. B. Fowler, H. Schmid, and D. Kern. *Quantized Hall effect in the presence of backscattering*. Physical Review Letters **61**, 2801 (1988).
- [167] R. J. Haug, A. H. MacDonald, P. Streda, and K. von Klitzing. *Quantized Multichannel Magnetotransport through a Barrier in Two Dimensions*. Physical Review Letters **61**, 2797 (1988).
- [168] A. M. Chang and J. E. Cunningham. *Transport evidence for phase separation into spatial regions of different fractional quantum Hall fluids near the boundary of a two-dimensional electron gas*. Physical Review Letters **69**, 2114 (1992).
- [169] B. I. Halperin. *Quantized Hall conductance, current-carrying edge states, and the existence of extended states in a two-dimensional disordered potential*. Physical Review B **25**, 2185 (1982).
- [170] M. Büttiker. *Absence of backscattering in the quantum Hall effect in multiprobe conductors*. Physical Review B **38**, 9375 (1988).
- [171] R. Ilan, N. Cooper, and A. Stern. *Longitudinal resistance of a quantum Hall system with a density gradient*. Physical Review B **73**, 235333 (2006).

- [172] E. M. Kendirlik, S. Sirt, S. B. Kalkan, W. Dietsche, W. Wegscheider, S. Ludwig, and A. Siddiki. *Anomalous resistance overshoot in the integer quantum Hall effect*. Scientific Reports **3**, 03133 (2013).
- [173] F. Fischer. *Growth and Electronic Properties of Two-Dimensional Systems on (110) Oriented GaAs*. Ph.D. thesis, Fakultät für Physik der Technischen Universität München Walter Schottky Institut (2004).
- [174] F. Fischer, M. Grayson, E. Schubert, D. Schuh, M. Bichler, and G. Abstreiter. *New anisotropic behavior of quantum Hall resistance in GaAs heterostructures at mK temperatures and fractional filling factors*. Physica E: Low-dimensional Systems and Nanostructures **22**, 108 (2004).
- [175] J. P. Eisenstein, R. Willett, H. L. Stormer, D. C. Tsui, A. C. Gossard, and J. H. English. *Collapse of the even-denominator fractional quantum Hall effect in tilted fields*. Physical Review Letters **61**, 997 (1988).
- [176] S. Ono and K. Sugihara. *Theory of transport properties in graphite*. Journal of Physical Society Japan **21**, 861 (1966).
- [177] K. Sugihara and H. Sato. *Electrical conductivity of graphite*. Journal of the Physical Society Japan **18**, 332 (1963).
- [178] W. Primak and L. Fuchs. *Electrical conductivities of natural graphite crystals*. Physical Review **95**, 22 (1954).
- [179] L. Edman, B. Sundqvist, E. McRae, and E. Litvin-Staszewska. *Electrical resistivity of single-crystal graphite under pressure: An anisotropic three-dimensional semimetal*. Physical Review B **57**, 6227 (1998).
- [180] I. Spain, A. Ubbelohde, and D. Young. *Electronic properties of well oriented graphite*. Philosophical Transactions of the Royal Society, Series A 345 (1967).
- [181] T. Tsuzuku. *Anisotropic electrical-conduction in relation to the stacking disorder in graphite*. Carbon **17**, 293 (1979).
- [182] I. Spain. *Chemistry and Physics of Carbon*, volume 19 (Taylor and Francis, 1981).
- [183] H. Kempa, P. Esquinazi, and Y. Kopelevic. *Field induced metal-insulator transition in the c-axis resistivity of graphite*. Physical Review B **65**, 241101 (2002).
- [184] T. Valla, P. Johnson, Z. Yusof, B. Wells, Q. Li, S. Loureiro, R. Cava, M. Mikami, Y. Nori, M. Yoshimura, and T. Sasaki. *Coherence-incoherence and dimensional crossover in layered strongly correlated metals*. Nature **417**, 627 (2002).
- [185] A. Lavrov, L. Kozeeva, M. Trunin, and V. Zvezrev. *Competition and coexistence of antiferromagnetism and superconductivity in  $R\text{Ba}_2\text{Cu}_3\text{O}_{6+x}$  ( $R = \text{Lu}, \text{Y}$ ) single crystals*. Physical Review B **79**, 214523 (2009).
- [186] B. Kelly. *Physics of Graphite* (Applied Science Publisher, 1981).

- [187] D. Tsang and M. Dresselhaus. *C-axis electrical-conductivity of kish graphite*. Carbon **14**, 43 (1976).
- [188] J. Barzola-Quiquia, J. Yao, P. Rodiger, K. Schindler, and P. Esquinazi. *Sample size effects on the transport characteristics of mesoscopic graphite samples*. Physica Status Solidi A **205**, 2924 (2008).
- [189] D. Maslov, V. Yudson, A. Somoza, and M. Ortuno. *Delocalization by disorder in layered systems*. Physical Review Letters **102**, 216601 (2009).
- [190] S. Zhang, J. Park, V. Milner, and A. Genack. *Photon delocalization transition in dimensional crossover in layered media*. Physical Review Letters **101**, 183901 (2008).
- [191] D. Maslov. Private communication.
- [192] To accommodate the wide range of sample heights, we take the upper plateau height plus 50 nm as the SiO<sub>2</sub> layer thickness. For the thickest samples, angle evaporation was used additionally to ensure complete coverage of the edges.
- [193] S. Tongay, J. Hwang, D. Tanner, H. Pal, D. Maslov, and A. Hebard. *Supermetallic conductivity in bromine-intercalated graphite*. Physical Review B **81**, 115428 (2010).
- [194] Producing samples in this range of thickness probably requires a fabrication technique other than exfoliation and presents further technical difficulties.
- [195] In a dip-stick, a calibrated Cernox chip-thermometer was mounted directly adjacent to the sample, ensuring a very similar temperature. The dip stick was moved slowly between liquid <sup>4</sup>He and the room temperature top flange while continuously measuring both sample and thermometer, resulting in many points in  $T$ . Cool-down and warm-up curves were measured and compared, giving nearly identical results, and confirming the accuracy of this method. To obtain  $\rho_c(T)$ , we perform the correction following Eq. 7.1 at every temperature, using  $\rho_{ab}(T)$ .
- [196] D. Soule. *Magnetic field dependence of the hall effect and magnetoresistance in graphite single crystals*. Physical Review **112**, 698 (1958).
- [197] Y. Zhang, J. Small, W. Pontius, and P. Kim. *Fabrication and electric-field-dependent transport measurements of mesoscopic graphite devices*. Applied Physics Letters **86**, 073104 (2005).
- [198] Y. Wang, Z. Ni, Z. Shen, H. Wang, and Y. Wu. *Interference enhancement of Raman signal of graphene*. Applied Physics Letters **92**, 043121 (2008).
- [199] G. Binnig, H. Fuchs, C. Gerber, H. Rohrer, E. Stoll, and E. Tosatti. *Energy-dependent state-density corrugation of a graphite surface as seen by scanning tunneling microscopy*. Europhysics Letters **1**, 31 (1986).
- [200] N. Garcia, P. Esquinazi, J. Barzola-Quiquia, and S. Dusari. *Evidence for semi-conducting behavior with a narrow band gap of Bernal graphite*. New Journal of Physics **14**, 053015 (2012).

- 
- [201] O. Zilberberg, A. Carmi, and A. Romito. *Measuring Cotunneling in its wake*. arxiv:1403.5897 (2014).
- [202] A. J. Keller, S. Amasha, I. Weymann, C. P. Moca, I. G. Rau, J. A. Katine, H. Shtrikman, G. Zarand, and D. Goldhaber-Gordon. *Emergent  $SU(4)$  Kondo physics in a spin-charge-entangled double quantum dot*. Nature Physics **10**, 145 (2014).
- [203] V. J. Goldman and B. Su. *Resonant Tunneling in the Quantum Hall Regime: Measurement of Fractional Charge*. Science **267**, 1010 (1995).
- [204] A. Kou, C. M. Marcus, L. N. Pfeiffer, and K. W. West. *Coulomb Oscillations in Antidots in the Integer and Fractional Quantum Hall Regimes*. Physical Review Letters **108**, 256803 (2012).
- [205] R. Zielke, B. Braunecker, and D. Loss. *Cotunneling in the  $\nu = 5/2$  fractional quantum Hall regime*. Physical Review B **86**, 235307 (2012).
- [206] Klinovaja, Jelena and Loss, Daniel. *Integer and fractional quantum Hall effect in a strip of stripes*. European Physical Journal B **87**, 171 (2014).
- [207] T. Meng, P. Stano, J. Klinovaja, and D. Loss. *Helical nuclear spin order in a strip of stripes in the Quantum Hall regime*. arXiv:1407.3726 (2014).
- [208] I. G. Rau, S. Amasha, M. Grobis, R. M. Potok, H. Shtrikman, and D. Goldhaber-Gordon. *Nonsaturating Dephasing Time at Low Temperature in an Open Quantum Dot*. arXiv:1210.0087 (2012).



## List of Figures

2.1	Schematic of the Nuclear Refrigerator Setup . . . . .	20
2.2	$T_{Cu}$ versus applied power to determine static heat leak . . . . .	23
2.3	The inverse of $T_{Cu}$ versus time to determine the static heat leak . . . . .	25
2.4	Cooling of $RuO_2$ thermometers during demagnetization . . . . .	27
2.5	Warm-up curves after demagnetization . . . . .	28
2.6	Demagnetization efficiency $\xi$ as a function of $B_f$ . . . . .	30
3.1	Layout of novel nanosample microkelvin refrigerator and CBT array . . . . .	33
3.2	CBT normalized differential conductance $g/g_T$ versus source-drain dc bias $V_{SD}$ for various NR temperatures . . . . .	35
3.3	CBT electron temperature $T_{CBT}$ versus NR temperature . . . . .	38
4.1	Working principle of quantum dot thermometry . . . . .	44
4.2	Direct transport quantum dot thermometry . . . . .	50
4.3	Charge sensing in a double quantum dot . . . . .	52
4.4	Charge sensing quantum dot thermometry . . . . .	54
5.1	Coulomb Blockade Thermometry in the Improved Setup . . . . .	63
5.2	Normal Metal/Insulator/Superconductor Junction Sample and Energy Diagram. . . . .	67
5.3	NIS I/V Curves at Different $T$ . . . . .	70
5.4	$B$ -Field Dependence of $\Delta V$ . . . . .	72
5.5	NIS thermometry . . . . .	74
5.6	Comparison between measured I-V and calculated I-V curves . . . . .	75
5.7	Primary NIS thermometer . . . . .	78
5.8	Reentrant Quantum Hall States for Thermometry . . . . .	81
5.9	Peaks Heights of Reentrant Quantum Halls States as Function of $T$ . . . . .	82
5.10	$T_{ext}$ as a function of $T_{Cu}$ for different noise levels $V_{rms}$ . . . . .	86
5.11	Fermi-Dirac distributions convoluted with Gaussian voltage noise distribution for different $V_{rms}$ . . . . .	87
6.1	Longitudinal resistance quantization . . . . .	92
6.2	Asymmetry in $B$ -field . . . . .	96
6.3	Temperature dependence of $R_{xy}$ and $R_{xx}$ . . . . .	98
6.4	Density gradient influence on energy gap of the $\nu = 5/2$ state . . . . .	100
7.1	Nano-graphite samples . . . . .	106
7.2	Thickness dependence on $\rho_c$ and $\rho_{ab}$ at room temperature . . . . .	110
7.3	Temperature dependence of resistivities . . . . .	111

7.4	Disorder characterization with micro-Raman spectroscopy . . . . .	113
7.5	Comparison of extraction methods for $\rho_c$ and $\rho_{ab}$ at room temperature	121

## A Curriculum Vitae

Lucas Casparis, from Bergün, Scharans, Fürstenau and Thusis, GR

2000 - 2004	Kantonsschule Sargans, Sargans
2004	Matura in Law and Economics
2005	military service
2005 - 2010	studies at the University of Basel
2009	semester at ETH Zürich
Jul. 2010	Master of Science in Nanosciences
2010 - 2014	PhD student at University of Basel

### Publications

A.Feshchenko\*, L. Casparis\*, M. Meschke, D. Maradan, M. Palma, J. P. Pekola and D.M. Zumbühl, *Normal Metal/Insulator/Superconductor Junction as Thermometer down to 5 mK*, in preparation.

L. Casparis, M. Lafkioti, T.-M. Liu, D. Maradan, C. Reichl, D.M. Zumbühl and W. Wegscheider, *Longitudinal Resistance Quantization and Density Gradient in the Integer Quantum Hall Regime*, in preparation.

D. Maradan\*, L. Casparis\*, T.-M. Liu, D.E.F. Biesinger, C. Scheller, D.M. Zumbühl, J. Zimmermann and A. C. Gossard, *GaAs Quantum Dot Thermometry using Direct Transport and Charge Sensing*, J. Low Temp. Phys. Volume 175, **5**, 784 (2014).

L. Casparis, D. Hug, D. Koelbl and D.M. Zumbühl, *Evidence for Disorder Induced Delocalization in Graphite*, 12. Jan. 2013, arxiv: 1301:2727.

L. Casparis, M. Meschke, D. Maradan, A. C. Clark, C. Scheller, K. K. Schwarzwälder, J. P. Pekola and D.M. Zumbühl, *Metallic Coulomb Blockade Thermometry down to 10 mK and below*, Rev. Sci. Instr. **83**, 083903 (2012).